UNIVERSITY OF CALIFORNIA

Los Angeles

Structural Studies of Pathogenic Amyloids

A dissertation submitted in partial satisfaction of the

requirements for the degree Doctor of Philosophy

in Molecular Biology

by

Smriti Sangwan

2017

ABSTRACT OF THE DISSERTATION

Structural Studies of Pathogenic Amyloids

by

Smriti Sangwan

Doctor of Philosophy in Molecular Biology

University of California, Los Angeles, 2017

Professor David S. Eisenberg, Chair

My research project is focused on deciphering the structural basis of toxicity in neurodegenerative diseases including Parkinson's and Lou Gehrig's (ALS) disease. Even though large proteinacious deposits that are amyloid in nature are found in these diseases, scientific evidence in recent years has tilted the opinion in favor of small oligomers as the more toxic species. However, the transient nature of these small oligomers has made their study extremely difficult. The Eisenberg lab has focused on characterizing amyloid aggregates from a structural perspective. We have deciphered the atomic resolution structure of segments from these proteins in their amyloid-like conformation and used the structures to design inhibitors that prevent aggregation. We have now focused on characterizing these transient oligomers. In my research, I have worked on two amyloid-forming proteins namely Superoxide Dismutase 1 (SOD1) and Alpha Synuclein (α-syn) and have attempted to understand the basis of their toxicity. My results suggest two different modes of action for these proteins. For SOD1, moderately sized oligomers

seem to be more toxic than insoluble amyloid aggregates, but for α-syn the fibers are more toxic. Using the atomic structure of the spine of α-syn fibrils, I have developed a new line of inhibitors that prevent fibril growth and propagation. My results reveal a novel therapeutic approach targeted at the spread and progression that may be applicable for PD and related synucleinopathies.

The dissertation of Smriti Sangwan is approved.

Bennett G. Novitch

Feng Guo

Alexander Hoffmann

Zhefeng Guo

David S. Eisenberg, Committee Chair

University of California, Los Angeles

2017

DEDICATION

I dedicate this work to my parents, my brother and sister and, my husband, Sarvesh.

TABLE OF CONTENTS

LIST OF FIGURES

LIST OF TABLES

Acknowledgements

First and foremost, I want to thank my advisor, David Eisenberg for his mentorship. His constant optimism and unwavering support has inspired me to pursue difficult projects to the best of my ability. His professional and personal advice over the years has shaped me as a scientist and as a person. He is truly my scientific hero.

I also want to thank all my committee members for their guidance through the years. Prof. Novitch was my collaborator on one of the projects, and I thank him for his advice. I realized early on that Prof. Feng Guo could not say no to students and asked for his help in reviewing fellowship applications, manuscripts etc. I thank him for bearing with me.

My best memories of graduate school are the numerous trips to the Advanced Photon Source in Chicago for which I thank Duilio Cascio and Michael Sawaya. I hope I can some day solve structures the way Mike does.

I also want to acknowledge the helpful discussions and advice of all my collaborators; Anni Zhao, Katrina Adams, Elizabeth Guenther, Angela Soriaga, Magdalena Ivanova, Lukasz Goldschmidt, Destaye Moore, Kevin Murray, Shruti Sahay, Michael Hughes, Lorena Saelices, Dr. Negar Khanlou, David Shaw group, Mike Bowers group, Carla Koehler lab, Mark Geisburg at Silverlake Research and Goedert lab at MRC.

Through graduate school, I met Angela Soriaga, Lorena Saelices, Elizabeth Guenther and Michael Hughes who have turned into lifelong friends. I thank them for many scientific discussions over coffee.

A special thanks to all Boyer Hall, Room 225 residents; Paul Seidler, Kevin Murray, David Boyer and Sarah Griner for they have made work all the more enjoyable.

Almost all members of the Eisenberg lab have contributed in one way or another in my projects either through direct collaborations or by offering advice and suggestions, and I thank them.

I also want to thank the Philip Whitcome Fellowship, the UCLA graduate division dissertation year fellowship and the Fowler award for financial support.

Finally, thanks to my husband, Sarvesh for his unconditional love and support. Without his support, I would not be writing this dissertation at all.

Vita

B.E. - Biotechnology *with honors* 2009

Maharshi Dayanand University, India

M.S. - Biomedical Engineering 2012

University of California, Los Angeles, CA

Whitcome Pre-doctoral Fellowship 2015

Molecular Biology Institute,

University of California, Los Angeles

Fowler Award Excellence in Protein Science 2016

Molecular Biology Institute,

University of California, Los Angeles

UCLA Graduate Division Dissertation Year Fellowship 2016

PUBLICATIONS

Smriti Sangwan, David S. Eisenberg 'Perspective on SOD1 mediated toxicity in Amyotrophic Lateral Sclerosis' Review Postepi Biochemii (2016)

Angela B. Soriaga, Smriti Sangwan, Ramsay Macdonald, Michael R. Sawaya, David Eisenberg "Crystal structures of IAPP amyloidogenic segments reveal a novel packing motif of out-of-register beta sheets" *The Journal of Physical Chemistry B* (2016) doi: 10.1021/acs.jpcb.5b09981

Jose A. Rodriguez, Magdalena I. Ivanova, Michael R. Sawaya, Duilio Cascio, Francis Reyes, Dan Shi, Smriti Sangwan, Elizabeth L. Guenther, Lisa M. Johnson, Meng Zhang, Lin Jiang, Mark A. Arbing, Brent Nannenga, Johan Hattne, Julian Whitelegge, Aaron S. Brewster, Marc Messerschmidt, Sébastien Boutet, Nicholas K. Sauter, Tamir Gonen, David Eisenberg "Structure of the toxic core of α-synuclein from invisible crystals" *Nature* (2015) doi:10.1038/nature15368

Do, Thanh D.*, Nichole E. LaPointe*, Smriti Sangwan*, David B. Teplow, Stuart C. Feinstein, Michael R. Sawaya, David S. Eisenberg, and Michael T. Bowers. "Factors That Drive Peptide Assembly from Native to Amyloid Structures: Experimental and Theoretical Analysis of [Leu-5]-Enkephalin Mutants." *The Journal of Physical Chemistry B* (2014) doi:10.1021/jp502473s. *equal contribution

Introduction and Dissertation Layout

Neurodegenerative diseases such as Alzheimer's, Parkinson's and Lou Gehrig's (ALS) are characterized by loss of neuronal cells, which leads to dementia, motor defects and ultimately death. These diseases are fatal and current treatment options are limited. Furthermore, with a global aging population they also present a huge financial burden on our health care system and emotional burden on caregivers. In all of these diseases, aggregated proteins – α-synuclein in Parkinson's, amyloid-β in Alzheimer's and SOD1 in ALS are found. Why these proteins aggregate and the structure of the toxic entity has been unknown until now. The Eisenberg lab has focused on characterizing amyloid aggregates from a structural perspective. We have deciphered the atomic resolution structures of segments from these proteins in their amyloid-like conformation and used the structures to design inhibitors that prevent aggregation. In my research, I have worked on two amyloid-forming proteins namely Superoxide Dismutase 1 (SOD1) and Alpha Synuclein (α-syn). My results suggest two different modes of action for these proteins. For SOD1, soluble oligomers seem to be more toxic than insoluble aggregates, but for α-syn the large aggregates are more toxic.

Dissertation Layout

Chapter 1 is a reprint of a review article published in 2016. In this review, we summarize the various hypotheses presented for the mechanism of SOD1-mediated motor neuron death in ALS. We discuss the different structural and biochemical studies performed on SOD1 and its familial mutants. I thank David Eisenberg for his help in writing this review.

Chapter 2 is a draft of the manuscript currently in submission for publication. In this work, we identified a short segment, 28-38 of SOD1 that is both necessary and sufficient for cytotoxicity. We discovered that the segment is important for oligomer formation but not for fibril formation. We also determined the atomic structure of this segment, which revealed an oligomer composed of anti-parallel β-strands forming a twisted sheet structure termed corkscrew. Using mutagenesis and biochemical assays, we showed that the integrity of the structure is critical for SOD1-mediated cytotoxicity. I thank Anni Zhao for help with experiments, Albert Pan and David Shaw for performing the computational simulations, Michael Sawaya for help with solving the structure, Katrina Adams and Destaye Moore for assistance with motor neuron culture, Christina Jayson, Jennifer Ngo and Carla Koehler for zebrafish experiments, Elizabeth Guenther and Angela Soriaga for biochemical assays, Anand Panchal and Mark Geisburg for antibody generation and Lukasz Goldshmidt and Rebecca Nelson for performing the computational predictions, and Bennett Novitch and David Eisenberg for help with experimental design and manuscript preparation.

Chapter 3 is a manuscript in preparation in which we build on our discovery of the corkscrew. We obtained three new atomic resolution structures of variants of the corkscrew-forming segment; a corkscrew-like structure, pairs of untwisted highly curved sheets and a steric zipper proto-filament structure. These results suggest that the segment has a high propensity to form corkscrew-like structures and the twisted sheet structure is important for cytotoxicity. I thank Michael Sawaya for help with solving the crystal structures, Kevin Murray for performing the computational predictions and Michael Hughes for help with fiber diffraction.

Chapter 4 is a manuscript in preparation. In this work, we developed a line of inhibitors that prevent α-syn aggregation. The small peptidic inhibitors were designed against the structure of a short segment of α-syn. Using biochemical and cell culture models of seeding, I tested the efficacy of the inhibitors and found them to effectively prevent α-syn aggregation and spread. These results reveal a novel therapeutic approach targeted at the prion-like spread of α-syn aggregates. I thank Lin Jiang and Kevin Murray for help with computational predictions, Shruti Sahay for help with biochemical assays and Michel Goedert for advice and suggestions.

Chapter 1: Perspective on SOD1 mediated toxicity in Amyotrophic Lateral Sclerosis

This chapter is a reprint of:

Perspective on SOD1 mediated toxicity in Amyotrophic Lateral Sclerosis.

Sangwan S, Eisenberg DS.

Postepy Biochem. 2016;62(3):362-369. Review.

Abstract: Amyotrophic lateral sclerosis (ALS) is a fatal neurodegenerative disease characterized by the progressive degeneration of spinal motor neurons. Although mutations in dozens of proteins have been associated with ALS, the enzyme, superoxide dismutase 1 (SOD1) was the first protein identified with the development of ALS and accounts for ~20% of familial cases. In experimental animals and patient samples, mutant SOD1 is found in cytoplasmic deposits implicating SOD1 aggregates as the toxic entities. Here we discuss the various biochemical and structure-based hypotheses proposed for mutant SOD1-associated ALS. Although much remains to be discovered about the molecular mechanism of SOD1 mediated toxicity, these hypotheses offer new avenues for therapeutic development.

Perspective on SOD1 mediated toxicity in Amyotrophic Lateral Sclerosis*

Smriti Sangwan

David S. Eisenberg✉

Molecular Biology Institute and Howard Hughes Medical Institute, UCLA, Los Angeles CA, USA

✉Molecular Biology Institute and Howard Hughes Medical Institute, UCLA, Box 95170, Los Angeles CA 90095-1570, USA; e-mail: david@mbi.ucla.edu

Received: May 30, 2016
Accepted: June 7, 2016

Key words: Amyotrophic lateral sclerosis; superoxide dismutase

Abbreviations: ALS, amyotrophic lateral sclerosis; SOD1, superoxide dismutase 1; fALS, familial ALS; sALS, sporadic ALS; wtSOD1, wild-type SOD1; mSOD1, mutant SOD1; H/D, hydrogen/deuterium

*The authors dedicate this review to the honor of Dr. Alexander Wlodawer on his 70th birthday, with admiration for his applications of structural biology to the understanding and treatment of disease.

Acknowledgements: We thank Elizabeth Guenther and Paul Seidler for discussion and NIH and HHMI for support. S.S. is supported by the Whitcome pre-doctoral fellowship

ABSTRACT

Amyotrophic lateral sclerosis (ALS) is a fatal neurodegenerative disease characterized by the progressive degeneration of spinal motor neurons. Although mutations in dozens of proteins have been associated with ALS, the enzyme, superoxide dismutase 1 (SOD1) was the first protein identified with the development of ALS and accounts for ~20% of familial cases. In experimental animals and patient samples, mutant SOD1 is found in cytoplasmic deposits implicating SOD1 aggregates as the toxic entities. Here we discuss the various biochemical and structure-based hypotheses proposed for mutant SOD1-associated ALS. Although much remains to be discovered about the molecular mechanism of SOD1 mediated toxicity, these hypotheses offer new avenues for therapeutic development.

INTRODUCTION

Amyotrophic lateral sclerosis (ALS) is a late-adult onset disease characterized by the loss of voluntary motor functions. Patients live an average of 3-5 years after the appearance of symptoms and very few are known to have survived for more than two decades [1]. Clinically the disease is identified by loss of motor function, which progresses in an unusually fast and unpredictable manner. Proteinaceous deposits are found in degenerating motor neurons of the cerebellum, cortex and spinal cord suggesting that protein aggregation is the underlying cause of the disease. Although 90% of all ALS cases are sporadic (sALS), 5–10% of cases are inherited and called familial ALS (fALS); these have a clear genetic linkage to a specific gene. Genome-wide association studies (GWAS) in the last decade have implicated nearly 30 genes in ALS pathogenesis. Of these, the majority code for the proteins TARDP, SOD1, FUS, VCP and OPTN (Fig. 1). The gene encoding the cytosolic enzyme, superoxide dismutase 1 (SOD1) was first discovered to have mutations in ALS patients in 1993 [2]. Mutations in the SOD1 gene are found in the exons suggesting that their toxic effects are the result of malfunctions of the protein. Furthermore, large aggregates that stain as SOD1 are found in autopsy samples suggesting a pathological link between SOD1 aggregates and motor neuron death. The role of SOD1 in sporadic and non-SOD1 linked fALS is less clear. Biochemical studies and antibody reactivity suggest an altered SOD1 conformation is present in both sALS and non-SOD1-linked fALS patients [3–5]. SOD1 aggregates are also observed in the presence of mutant TDP-43 and FUS in patients and in cell culture suggesting cross talk between various proteins associated with ALS [6]. An oxidized form of wild-type SOD1 (wtSOD1) has also been detected in sporadic patient tissues [7]. Recently,

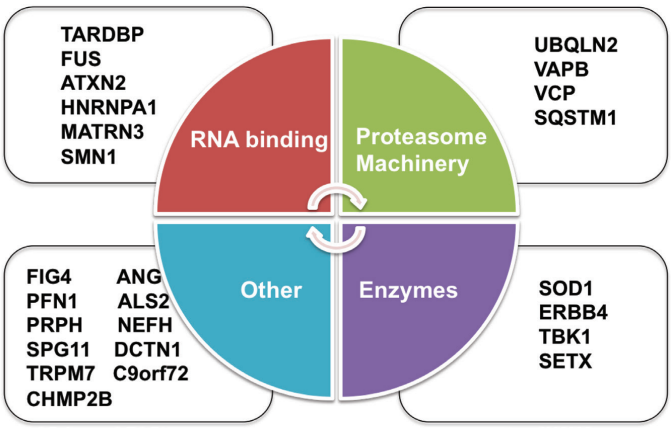

Figure 1. Different ALS-linked genes classified by function.

mutations in SOD1 were also found in sporadic forms of ALS such as the aggressive juvenile-onset ALS [8,9]. From these reports it appears that SOD1 plays a role that extends to ALS cases associated with mutations in other proteins, as well as to at least some sporadic cases. To date more than 160 different disease-associated mutations have been found in SOD1; these are spread over the entire 153 amino acid sequence (http://alsod.iop.kcl.ac.uk). Studies over the last two decades have elucidated key features of mutant SOD1 (mSOD1) aggregation. It is generally accepted that mSOD1 acquires toxic properties: mSOD1 does not lose its enzymatic activity [10] and knockdown of wild-type SOD1 does not cause ALS symptoms in mice [11]. Together these observations strengthen the hypothesis that disease mutations confer a toxic function that ultimately causes cellular dysfunction.

In this review, we summarize the various hypotheses proposed for mSOD1 toxicity. We focus on the biophysical studies of SOD1 mutants, and in particular the biochemical and structural data that suggest varying roles for different regions of the SOD1 protein in aggregation and ALS pathogenesis.

STRUCTURAL MODELS FOR CHANGES IN MUTANT SOD1

Several proteins associated with neurodegenerative diseases such as β-amyloid, α-synuclein and islet amyloid polypeptide do not have a native tertiary structure. However, SOD1 does have a tertiary structure and the effect of mutations on the native structure has been extensively studied. The native metal-bound SOD1 exists as a homo-dimer wherein each monomer has a Greek key architecture and binds one copper and one zinc ion (Fig. 2A). The monomer is composed of an eight-stranded β barrel and two loops – the metal binding loop (spanning residues 49-84) and the electrostatic loop (spanning residues 122-143) [12,13]. The simplest hypothesis for mutant SOD1-mediated neuronal damage is that the presence of each disease mutation increases the aggregation propensity of the protein. These aggregates accumulate over time and are toxic to neuronal cells. In support of this hypothesis, severity of the disease correlates with the aggregation propensity of the mutants. For example, patients with the A4V mutation survive only 6 months post symptom-onset and this mutation increases the aggregation propensity many fold. However, the increase in aggregation propensity does not correlate with an earlier age of disease onset [14,15]. Furthermore, not all disease mutations increase the aggregation propensity of the protein [14] (Table 1). Structural studies of more than a dozen different SOD1 constructs harboring disease-related mutations have been carried out and provide conflicting results. Overall, most mutations do not cause major structural alterations to the native SOD1 structure [16]. Crystal structures of A4V and I113T mutants show some structural deviations in the dimer interface that might contribute to increased aggregation propensity [17] and the structure of the G37R mutant shows altered subunit arrangement [18] while structures of D124V and H80R mutants show disrupted metal binding loops [19]. Mutations such as A4V, G93A, I113T and G37R also do not affect the enzymatic activity

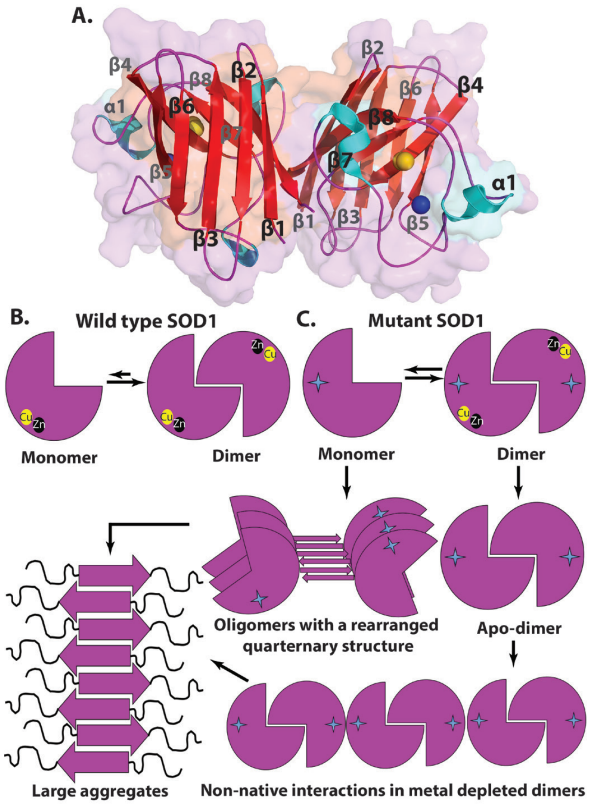

Figure 2. A) Crystal structure of metal-bound SOD1 (PDB 2C9S). Native SOD1 exists as a stable dimer. Each monomer is composed of an eight-stranded β barrel (red) and a metal binding loop (magenta) and an electrostatic loop. Cu and Zn are shown respectively as yellow and blue spheres. Strands facing towards the viewer are named in black and away from the viewer are named in gray. B) Wild type SOD1 is an exceptionally stable dimer and can be monomerized only by loss of metal ions. C) A disease mutation (blue cross) can gain a toxic function by different modes. It can increase the propensity to monomerize and these monomers in turn can form oligomers with non-native quaternary structure that may be toxic. Another mode of oligomerization involves apo dimers that harbor non-native contacts forming fibrous assemblies.

of the protein whereas G85R and H48Q mutations that are present in the metal binding loop lead to reduced activity [16]. In light of these conflicting reports, it is difficult to determine if increased aggregation propensity is the only effect of mutations that cause the disease; whereas protein aggregation may contribute to disease progression, it may not be the cause of the disease itself.

Another hypothesis is that the mutations introduce structural instability either by destabilizing the native structure or by reducing its metal binding affinity [20]. One line of evidence supporting this hypothesis is that large molecular weight aggregates are seen prior to disease onset in transgenic mice [21,22]. Additionally, large inclusion bodies containing insoluble SOD1 are found only in end-stage mice [23,24]. Biochemical and cell culture studies also show that SOD1 forms soluble oligomers that are sufficient to cause toxicity [25–29]. In-cell NMR and mutagenesis studies have shown that several mutants lack metal binding and are prone to oligomerization [30]. Structural studies of metal

Table 1. Comparison of several SOD1 mutations

Location of mutation	Mutations	Aggregation propensity vs. wt	Melting temperature vs. wt
β barrel	G37R	Similar	Similar
Electrostatic loop	N139K	High	Similar
Metal binding loop	H46R,D134N, H80R, D124V	High	Low
Dimer Interface	A4V, I113T	High	Low

depleted mutants also support this hypothesis. For example, in the crystal structures of the metal deficient mutants – H46R, S134N, D124V and H80R significant new inter-molecule interfaces are observed [19,31–33]. The buried surface area in these new interactions is identical to the native dimeric interface and thus proposed to be significant. Furthermore, these new interfaces can only occur by rearranging the metal binding loop. Therefore, reduced metal binding would increase flexibility and in principle stabilize these interactions. However, it is important to note that these interactions are observed only in the crystal structures and their physiological relevance has been unclear.

In addition to studies investigating the effect of disease-linked mutations on the global structure of SOD1, research groups have analyzed the SOD1 protein sequence to identify segments that affect the aggregation kinetics. Aggregates isolated from the spinal cords of transgenic mice have been shown to contain full-length SOD1 that is devoid of metals [34,35] but limited proteolysis and atomic force microscopy experiments suggest that the core of large aggregates formed by SOD1 is composed of residues 1-63 [36]. Molecular dynamic simulations, mass spectrometry and hydrogen/deuterium (H/D) exchange studies suggest local unfolding of the β-barrel and exceptional flexibility in the β strands 3 and 4 corresponding to residues 29-36 and 41-48 [37–39]. These strands compose the β barrel and thus their rearrangement likely induces changes in the structure to enable secondary interactions that are important for aggregation. In vivo models and cell culture studies also suggest that the N-terminal region of SOD1 plays an important role in toxicity, in particular residues such as Trp32 that may be important sites for post translational modifications [8,40,41]. Another study with shorter segments identified 4 different segments that are important for aggregation [42]. Mutations in two of these segments – 101-107 and 147-153 changed the aggregation propensity suggesting that these segments play an important role in the initiation of aggregation. The segment 147-153 lies at the dimer interface and this peptide segment can seed fibril formation of the full-length protein in vitro [42], suggesting that it plays an important role in aggregation.

SOD1 monomer also has 4 cysteine residues (Cys 6, Cys 57, Cys 111, and Cys 146) with Cys 57 and Cys 146 engaged in a disulfide bond. The role of these Cys residues in SOD1 aggregation has been explored (reviewed in [23,43]. SOD1 mutations increase the aggregation propensity of disulfide-reduced apo-SOD1 [44,45] and aberrant disulfide-linked oligomers are detected in spinal cord homogenates of transgenic mice [46]. However, mutating the cysteine residues does not change the aggregation propensity of the protein [47]. Also, cysteine residues are not conserved across different species. Taken together, these reports suggest that disulfide reduction is an important albeit non-critical step in the toxic aggregation pathway.

Overall, these biochemical and structural studies suggest that SOD1 mediated toxicity is likely caused by a combination of different events such as aberrant disulfide reduction, the presence of a disease-associated mutation and reduced metal binding (Fig. 2). One or more of these events results in a shift in the equilibrium toward pathogenic aggregation.

TOXIC SOD1 SPECIES – LARGE AGGREGATES OR SOLUBLE OLIGOMERS

The molecular stoichiometry of the toxic species in neurodegenerative diseases has been intensely debated. While large aggregates are considered to be the pathological hallmark of Alzheimer's or Parkinson's disease and ALS, evidence for small oligomers as the toxic entities has also been presented.

In case of SOD1, evidence for both large aggregates and small oligomers as the toxic species has been given. Large inclusions are a defining histological feature of patients and detergent insoluble aggregates are formed in animal models as well. However, the cause and effect relationship between insoluble aggregates and motor neuron death is unclear. Several studies of SOD1 suggest that small oligomers may also be toxic. In these experiments, disulfide reduced forms of mutant SOD1 were detected that may be the precursor species for the large aggregates [25,26,28,29]. The minimum toxic species has been proposed to be trimeric with a non-native quaternary assembly [48]. Similar trimeric assemblies have been proposed for other aggregating proteins such as tau [49], amyloid-β [50] and α-synuclein [51]. The structural details of these toxic oligomers have been elusive till now and it is also not known if the native SOD1 structure is intact or not.

PRION-LIKE BEHAVIOR OF SOD1

It is increasingly appreciated for neurodegenerative diseases that protein aggregates can transfer from cell to cell much like the aggregated forms of the PrP prion protein. Protein aggregates of α-synuclein [52–54], tau [55], β-amyloid [56,57] have been shown to act as templates for seeding native protein into aggregates as do prion proteins, a behavior termed 'Prion-like'. However, the behavior of these proteins differs from the canonical prion proteins, as

there is no evidence of transmission of disease between individuals by transfer of aggregates.

Several lines of evidence for transmission of SOD1 aggregates have been found. SOD1 is abundant in the cytoplasm but has been reported also to be secreted extracellularly *in vitro* [58–60]. Additionally, co-culturing of non-neuronal cells such as astrocytes expressing mSOD1 induces toxicity in motor neurons expressing unmutated wtSOD1 [61,62]. However, it is not clear if the toxic effect on motor neurons is due to mSOD1 transmission or through a signaling cascade. Overexpression of human wtSOD1 in mice expressing the familial mutant G85R accelerates the disease onset suggesting recruitment of wtSOD1 in aggregation [63]. It has also been shown that spinal cord homogenates from mSOD1 transgenic mice can seed aggregation of the protein *in vitro* [64]. Finally, injection of spinal cord homogenates in mice induces pathology that spreads to distant regions of the spinal cord [65–68]. Although mutant SOD1 forms intracellular inclusions it is possible that a soluble, transferred form is sufficient for spread of pathology. Taken together, these studies suggest that SOD1 aggregation may initiate spontaneously in a section of motor neurons and could then be sequentially transferred from cell to cell. This hypothesis is also supported by the clinical disease progression, which starts with loss of a subset of motor neurons and then progresses through connected anatomical regions.

COMPARISON OF SOD1 WITH OTHER ALS-LINKED PROTEINS

Gene sequencing has associated nearly 30 different genes with ALS. A majority of these including TARDP, FUS, OPTN, VCP and hnRNP are RNA binding proteins that are also capable of forming aggregates in response to stress [69–71]. In these cases, the pathology appears to derive from both a loss of native function and gain of toxic function as disease causing mutations often render the protein functionally inactive [72–74]. Indeed the mechanism of toxicity of RNA binding proteins seems to differ from that of SOD1. For RNA binding proteins defects in nuclear pore assembly and defective RNA processing [73,75,76] have been found whereas for SOD1, mitochondrial defects [77–80], golgi fragmentation [59], defects in proteasome machinery and axonal transport [77,81] have been found. These differences highlight an important realization that even though all forms of ALS are associated with protein aggregation, the mechanisms that cause toxicity are likely to differ from case-to-case, depending on the proteins that are mutated.

Another aspect that differentiates SOD1 from other ALS-associated proteins such as TDP43, FUS and VCP is the exclusivity of mutant SOD1 to ALS. For example, aggregates of TDP43 are also found in Alzheimer's and frontotemporal dementia (FTD) cases [82,83] , FUS is also associated with FTD [84] and VCP mutants are found in inclusion body myopathy with early-onset Paget disease and frontotemporal dementia (IBMPFD) [85]. In contrast, SOD1 mutants are associated only with ALS and there is no evidence of SOD1 aggregation in any other neurodegenerative disease. As all forms of ALS cases are clinically similar, researchers have studied the mechanism of disease onset in models of familial cases in hopes that the information could be used to design drugs that would be effective against all forms of the disease. However, as more genes are implicated in ALS, it appears that even though protein aggregation is a central theme, the downstream effects of these aggregates may differ. Thus, it may be necessary to understand the toxic properties and disease pathway of each ALS-associated protein.

THERAPEUTIC DEVELOPMENT FOR SOD1-RELATED ALS

Various strategies have been explored to protect against SOD1 aggregation and to prevent neuronal loss. Among these siRNA-based gene silencing that reduces mutant SOD1 protein production was found to be well tolerated in phase 1 clinical trials [86,87]. A similar approach was also shown to be effective in a C9orf72 mouse model [88] and thus may be applicable to all forms of ALS.

In animal models, immunization approaches using antibodies that bind to a disease-specific conformation have been shown to be marginally effective [89]. The anti-SOD1 antibodies tested increased the life span of transgenic mice by 6–9 days and thus provide proof of concept for immunization therapy. Full-length SOD1 and its shorter segments such as peptide 143-151 that lies at the dimer interface have also been used to elicit immune response in animal models [90,91]. This vaccination approach was successful in delaying disease onset by 28 days and increased the overall lifespan of transgenic mice by 40 days.

With the advent of stem cell differentiation and induced pluripotent stem cells (iPSCs), patient derived motor neurons are being used to discover small molecule therapeutics. Patient-derived motor neurons show reduced survival and recapitulate the defects seen in transgenic mouse models such as reduced axon transport and mitochondrial defects [77,92]. Stem cell-derived motor neurons offer a fast method for high throughput screening of potential therapeutics. Indeed the first few studies have yielded several small molecules that inhibit aggregation *in vitr*o and alleviate the toxic effects in cell culture [93,94].

Intriguingly, all ALS-linked mutant proteins are expressed ubiquitously in all tissues yet they aggregate only in the spinal cord. In this regard, some studies have focused on identifying a protective factor that may be present in non-neuronal tissues. In one study, a chaperone MIF2 (macrophage inhibitory factor) that expresses in non-neuronal tissues was discovered that inhibits SOD1 aggregation [95]. In a parallel approach, over expression of chaperones such as HSJ1 [96] and Hsp110 [97] specifically in spinal motor neurons conferred protection. In a related study, a small molecule inhibitor, Sephin1 was developed that activates the proteasome system and increases chaperone production [98]. Sephin1 reduced the motor deficits and insoluble aggregate formation in transgenic mice expressing G93A mSOD1. Although these results are preliminary, they suggest that over-expression of individual chaperones or stimulating chaperone production have therapeutic potential.

A promising approach to therapy for amyloid diseases is stabilizing the native structure of proteins such that the equilibrium shifts away from aggregation. This approach has most successfully been applied for transthyretin [99] and light chain amyloidosis [100] but it remains unexplored for SOD1 till now. A few studies have shown that stabilizing the native structure of SOD1 by chemical crosslinking or by small molecules delays aggregation [101–103]. Intriguingly, when these compounds were co-crystallized with SOD1 they were found to bind not at the dimer interface but to the β-barrel, in particular β-strands 2, 3 and 6 suggesting that these strands play a role in aggregation.

CONCLUSIONS

Since its discovery as an ALS-linked protein, SOD1 has been extensively studied *in vitro*, in cell culture, and in animal models. Overall, various hypotheses such as increased aggregation propensity, dimer destabilization and oligomerization have been proposed for mSOD1 toxicity that may not be mutually exclusive. It is conceivable that under different conditions such as presence of a mutation, oxidative stress, and aberrant metal binding different mechanisms for toxicity are initiated.

Critical questions that remain unanswered include: the structure of the toxic species, the role of SOD1 in sporadic ALS, the mechanism of prion-like, intercellular spread of aggregates, and whether SOD1 and other ALS-linked proteins share a common pathogenic pathway. Answering these critical questions will ultimately help to defeat this devastating disease.

REFERENCES

1. Salameh J, Brown R, Berry J (2015) Amyotrophic lateral sclerosis: Review Semin Neurol 35: 469–476
2. Rosen DR, Siddique T, Patterson D, Figlewicz DA, Sapp P, Hentati A, Donaldson D, Goto J, O'Regan JP, Deng HX, Rahmani Z, Krizus A, Mckenna-Yasek D, Cayabyab A, Gaston SM, Berger R, Tanzi R E, Halperin J J , Herzfeldt B, Van Den Bergh R, Hung WY, Bird T, Deng G, Mulder DW, Smyth C, Laing NG, Soriano E, Pericak–Vance MA, Haines J, Rouleau GA, Gusella JS, Horvitz HR, Brown RH (1993) Mutations in Cu/Zn superoxide dismutase gene are associated with familial amyotrophic lateral sclerosis. Nature 362: 59–62
3. Bosco DA, Morfini G, Karabacak NM, Song Y, Gros-Louis F, Pasinelli P, Goolsby H, Fontaine BA, Lemay N, McKenna-Yasek D, Frosch MP, Agar JN, Julien JP, Brady ST, Brown RH (2010) Wild-type and mutant SOD1 share an aberrant conformation and a common pathogenic pathway in ALS. Nat Neurosci 13: 1396–403
4. Forsberg K, Jonsson PA, Andersen PM, Bergemalm D, Graffmo KS, Hultdin M, Jacobsson J, Rosquist R, Marklund SL, Brännström T (2010) Novel antibodies reveal inclusions containing non-native SOD1 in sporadic ALS patients. PLoS One 5: e11552
5. Gruzman A, Wood WL, Alpert E, Prasad MD, Miller RG, Rothstein JD, Bowser R, Hamilton R, Wood TD, Cleveland DW, Lingappa VR, Liu J (2007) Common molecular signature in SOD1 for both sporadic and familial amyotrophic lateral sclerosis. Proc Natl Acad Sci 104: 12524–12529
6. Pokrishevsky E, Grad LI, Yousefi M, Wang J, Mackenzie IR, Cashman NR (2012) Aberrant localization of FUS and TDP43 is associated with misfolding of SOD1 in amyotrophic lateral sclerosis. PLoS One 7: e35050
7. Guareschi S, Cova E, Cereda C, Ceroni M, Donetti E, Bosco DA, Trotti D, Pasinelli P (2012) An over-oxidized form of superoxide dismutase found in sporadic amyotrophic lateral sclerosis with bulbar onset shares a toxic mechanism with mutant SOD1. Proc Natl Acad Sci 109: 5074–5079
8. Ezzi SA, Urushitani M, Julien J-P (2007) Wild-type superoxide dismutase acquires binding and toxic properties of ALS-linked mutant forms through oxidation. J Neurochem 102: 170–178
9. Zou Z-Y, Liu M-S, Li X-G, Cui L-Y (2015) Mutations in SOD1 and FUS caused juvenile-onset sporadic amyotrophic lateral sclerosis with aggressive progression. Ann Transl Med 15: 221
10. Borchelt DR, Lee MK, Slunt HS, Guarnieri M, Xu Z-S, Wong PC, Brown RH Jr, Price DL, Sisodia SS, Cleveland DW (1994) Superoxide dismutase 1 with mutations linked to familial amyotrophic lateral sclerosis possesses significant activity. Proc Natl Acad Sci 91: 8292–8296
11. Bruijn LI, Houseweart MK, Kato S, Anderson KL, Anderson SD, Ohama E, Reaume AG, Scott RW, Cleveland DW (1998) Aggregation and motor neuron toxicity of an ALS-linked SOD1 mutant independent from Wild-Type SOD1. Science 281: 1851–1854
12. Parge HE, Hallewell RA, Tainer JA (1992) Atomic structures of wild-type and thermostable mutant recombinant human Cu,Zn superoxide dismutase. Proc Natl Acad Sci 89: 6109–6113
13. Tainer JA, Getzoff ED, Beem KM, Richardson JS, Richardson DC (1982) Determination and analysis of the 2 Å structure of copper, zinc superoxide dismutase. J Mol Biol 160: 181–217
14. Rodriguez JA, Shaw BF, Durazo A, Sohn SH, Doucette PA, Nersissian AM, Faull KF, Eggers DK, Tiwari A, Hayward LJ, Valentine JS (2005) Destabilization of apoprotein is insufficient to explain Cu,Zn-superoxide dismutase-linked ALS pathogenesis. Proc Natl Acad Sci 102: 10516–10521
15. Wang Q, Johnson JL, Agar NYR, Agar JN (2008) Protein aggregation and protein instability govern familial amyotrophic lateral sclerosis patient survival. PLoS Biol 6: e170
16. Shaw B, Valentine J (2007) How do ALS-associated mutations in superoxide dismutase 1 promote aggregation of the protein? Trends Biochem Sci 32: 78–85
17. Hough MA, Grossmann JG, Antonyuk SV, Strange RW, Doucette PA, Rodriguez JA, Whitson LJ, Hart PJ, Hayward LJ, Valentine JS, Hasnain SS (2004) Dimer destabilization in superoxide dismutase may result in disease-causing properties: Structures of motor neuron disease mutants. Proc Natl Acad Sci 101: 5976–5981
18. Hart PJ, Liu H, Pellegrini M, Nersissian AM, Gralla EB, Valentine JS, Eisenberg D (1998) Subunit asymmetry in the three-dimensional structure of a human CuZnSOD mutant found in familial amyotrophic lateral sclerosis. Protein Sci 7: 545–555
19. Seetharaman SV, Winkler DD, Taylor AB, Cao X, Whitson LJ, Doucette PA, Valentine JS, Schirf V, Demeler B, Carroll MC, Culotta VC, Hart PJ (2010) Disrupted zinc-binding sites in structures of pathogenic SOD1 variants D124V and H80R. Biochemistry (Mosc) 49: 5714–5725
20. Lindberg MJ, Bystrom R, Boknas N, Andersen PM, Oliveberg M (2005) Systematically perturbed folding patterns of amyotrophic lateral sclerosis (ALS)-associated SOD1 mutants. Proc Natl Acad Sci 102: 9754–9759
21. Johnston JA, Dalton MJ, Gurney ME, Kopito RR (2000) Formation of high molecular weight complexes of mutant Cu,Zn-superoxide dismutase in a mouse model for familial amyotrophic lateral sclerosis. Proc Natl Acad Sci 97: 12571–12576
22. Jonsson PA, Ernhill K, Andersen PM, Bergemalm D, Brännström T, Gredal O, Nilsson P, Marklund SL (2004) Minute quantities of misfolded mutant superoxide dismutase-1 cause amyotrophic lateral sclerosis. Brain 127: 73–88
23. Karch CM, Prudencio M, Winkler DD, Hart PJ, Borchelt DR (2009) Role of mutant SOD1 disulfide oxidation and aggregation in the pathogenesis of familial ALS. Proc Natl Acad Sci 106: 7774–7779
24. Wang J, Xu G, Borchelt DR (2002) High molecular weight complexes of mutant superoxide dismutase 1: age-dependent and tissue-specific accumulation. Neurobiol Dis 9: 139–48
25. Banci L, Bertini I, Boca M, Girotto S, Martinelli M, Valentine JS, Vieru M (2008) SOD1 and amyotrophic lateral sclerosis: mutations and oligomerization. PLoS One doi: 10.1371/journal.pone.0001677

26. Banci L, Bertini I, Durazo A, Girotto S, Gralla EB, Martinelli M, Valentine JS, Vieru M, Whitelegge JP (2007) Metal-free superoxide dismutase forms soluble oligomers under physiological conditions: A possible general mechanism for familial ALS. Proc Natl Acad Sci 104: 11263–11267
27. Brotherton TE, Li Y, Glass JD (2013) Cellular toxicity of mutant SOD1 protein is linked to an easily soluble, non-aggregated form *in vitro*. Neurobiol Dis 49: 49–56
28. Park Y-N, Zhao X, Norton M, Taylor JP, Eisenberg E, Greene LE (2012) Huntingtin fragments and SOD1 mutants form soluble oligomers in the cell. PLoS One 7: e40329
29. Redler RL, Fee L, Fay JM, Caplow M, Dokholyan NV (2014) Non-native soluble oligomers of Cu/Zn superoxide dismutase (SOD1) contain a conformational epitope linked to cytotoxicity in amyotrophic lateral sclerosis (ALS). Biochemistry (Mosc) 53: 2423–2432
30. Luchinat E, Barbieri L, Rubino JT, Kozyreva T, Cantini F, Banci L (2014) In-cell NMR reveals potential precursor of toxic species from SOD1 fALS mutants. Nat Commun 5: 5502
31. Elam JS, Strange R, Antonyuk S, Doucette PA, Rodriguez JA, Hasnain SS, Hayward LJ, Valentine JS, Yeates TO, Hart PJ (2003) Amyloid-like filaments and water-filled nanotubes formed by SOD1 mutant proteins linked to familial ALS. Nat Struct Biol 10: 461–467
32. Galaleldeen A, Strange RW, Whitson LJ, Antonyuk SV, Narayana N, Taylor AB, Schuermann JP, Holloway SP, Hasnain SS, Hart PJ (2009) Structural and biophysical properties of metal-free pathogenic SOD1 mutants A4V and G93A. Arch Biochem Biophys 492: 40–47
33. Valentine JS, Hart PJ (2003) Misfolded CuZnSOD and amyotrophic lateral sclerosis. Proc Natl Acad Sci 100: 3617–3622
34. Lelie HL, Liba A, Bourassa MW, Chattopadhyay M, Chan PK, Gralla EB, Miller LM, Borchelt DR, Valentine JS, Whitelegge JP (2011) Copper and zinc metallation status of copper-zinc superoxide dismutase from amyotrophic lateral sclerosis transgenic mice. J Biol Chem 286: 2795–2806
35. Shaw BF, Lelie HL, Durazo A, Nersissian AM, Xu G, Chan PK, Gralla EB, Tiwari A, Hayward LJ, Borchelt DR, Valentine JS, Whitelegge JP (2008) Detergent-insoluble aggregates associated with amyotrophic lateral sclerosis in transgenic mice contain primarily full-length, unmodified superoxide dismutase-1. J Biol Chem 283: 8340–8350
36. Chan PK, Chattopadhyay M, Sharma S, Souda P, Gralla EB, Borchelt DR, Whitelegge JP, Valentine JS (2013) Structural similarity of wild-type and ALS-mutant superoxide dismutase-1 fibrils using limited proteolysis and atomic force microscopy. Proc Natl Acad Sci 110: 10934–10939
37. Assfalg M, Banci L, Bertini I, Turano P, Vasos PR (2003) Superoxide dismutase folding/unfolding pathway: role of the metal ions in modulating structural and dynamical features. J Mol Biol 330: 145–158
38. Durazo A, Shaw BF, Chattopadhyay M, Faull KF, Nersissian AM, Valentine JS, Whitelegge JP (2009). Metal-free superoxide dismutase-1 and three different amyotrophic lateral sclerosis variants share a similar partially unfolded beta-barrel at physiological temperature. J Biol Chem 284: 34382–34389
39. Shaw BF, Durazo A, Nersissian AM, Whitelegge JP, Faull KF, Valentine JS (2006) Local unfolding in a destabilized, pathogenic variant of superoxide dismutase 1 observed with H/D exchange and mass spectrometry. J Biol Chem 281: 18167–18176
40. Mulligan VK, Kerman A, Laister RC, Sharda PR, Arslan PE, Chakrabartty A (2012) Early steps in oxidation-induced SOD1 misfolding: implications for non-amyloid protein aggregation in familial ALS. J Mol Biol 421: 631–65
41. Taylor DM, Gibbs BF, Kabashi E, Minotti S, Durham HD, Agar JN (2007) Tryptophan 32 potentiates aggregation and cytotoxicity of a copper/zinc superoxide dismutase mutant associated with familial amyotrophic lateral sclerosis. J Biol Chem 282: 16329–16335
42. Ivanova MI, Sievers SA, Guenther EL, Johnson LM, Winkler DD, Galaleldeen A, Sawaya MR, Hart PJ, Eisenberg DS (2014) Aggregation-triggering segments of SOD1 fibril formation support a common pathway for familial and sporadic ALS. Proc Natl Acad Sci 111: 197–201
43. Sheng Y, Chattopadhyay M, Whitelegge J, Valentine JS (2012) SOD1 aggregation and ALS: role of metallation states and disulfide status. Curr Top Med Chem 12: 2560–72
44. Furukawa Y, O'Halloran TV (2005) Amyotrophic lateral sclerosis mutations have the greatest destabilizing effect on the apo- and reduced form of SOD1, leading to unfolding and oxidative aggregation. J Biol Chem 280: 17266–17274
45. Oztug Durer ZA, Cohlberg JA, Dinh P, Padua S, Ehrenclou K, Downes S, Tan JK, Nakano Y, Bowman CJ, Hoskins JL, Kwon C, Mason AZ, Rodriguez JA, Doucette PA, Shaw BF, Valentine JS (2009) Loss of metal ions, disulfide reduction and mutations related to familial ALS promote formation of amyloid-like aggregates from superoxide dismutase. PLoS One 4: e5004
46. Furukawa Y, Fu R, Deng H-X, Siddique T, O'Halloran TV (2006) Disulfide cross-linked protein represents a significant fraction of ALS-associated Cu, Zn-superoxide dismutase aggregates in spinal cords of model mice. Proc Natl Acad Sci 103: 7148–7153
47. Karch CM, Borchelt DR (2008) A limited role for disulfide cross-linking in the aggregation of mutant SOD1 linked to familial amyotrophic lateral sclerosis. J Biol Chem 283: 13528–13537
48. Proctor EA, Fee L, Tao Y, Redler RL, Fay JM, Zhang Y, Lv Z, Mercer IP, Deshmukh M, Lyubchenko YL, Dokholyan NV (2016) Nonnative SOD1 trimer is toxic to motor neurons in a model of amyotrophic lateral sclerosis. Proc Natl Acad Sci 113: 614–619
49. Mirbaha H, Holmes BB, Sanders DW, Bieschke J, Diamond MI (2015) Tau trimers are the minimal propagation unit spontaneously internalized to seed intracellular aggregation. J Biol Chem 290: 14893–14903
50. Kreutzer AG, Hamza IL, Spencer RK, Nowick JS (2016) X-ray crystallographic structures of a trimer, dodecamer, and annular pore formed by an $A\beta_{17-36}$ β-Hairpin. J Am Chem Soc 138: 4634–4642
51. Ostrerova-Golts N, Petrucelli L, Hardy J, Lee JM, Farer M, Wolozin B (2000) The A53T alpha-synuclein mutation increases iron-dependent aggregation and toxicity. J Neurosci 20: 6048–6054
52. Guo JL, Covell DJ, Daniels JP, Iba M, Stieber A, Zhang B, Riddle DM, Kwong LK, Xu Y, Trojanowski JQ, Lee VM (2013) Distinct α-synuclein strains differentially promote tau inclusions in neurons. Cell 154: 103–117
53. Luk KC, Song C, O'Brien P, Stieber A, Branch JR, Brunden KR, Trojanowski JQ, Lee VM (2009) Exogenous alpha-synuclein fibrils seed the formation of Lewy body-like intracellular inclusions in cultured cells. Proc Natl Acad Sci 106: 20051–20056
54. Masuda-Suzukake M, Nonaka T, Hosokawa M, Oikawa T, Arai T, Akiyama H, Mann DM, Hasegawa M (2013) Prion-like spreading of pathological alpha-synuclein in brain. Brain 136: 1128–1138
55. Sanders DW, Kaufman SK, DeVos SL, Sharma AM, Mirbaha H, Li A, Barker SJ, Foley AC, Thorpe JR, Serpell LC, Miller TM, Grinberg LT, Seeley WW, Diamond MI (2014) Distinct Tau prion strains propagate in cells and mice and define different tauopathies. Neuron 82: 1271–1288
56. Heilbronner G, Eisele YS, Langer F, Kaeser SA, Novotny R, Nagarathinam A, Aslund A, Hammarström P, Nilsson KP, Jucker M (2013) Seeded strain-like transmission of β-amyloid morphotypes in APP transgenic mice. EMBO Rep 14: 1017–1022
57. Meyer-Luehmann M, Coomaraswamy J, Bolmont T, Kaeser S, Schaefer C, Kilger E, Neuenschwander A, Abramowski D, Frey P, Jaton AL, Vigouret JM, Paganetti P, Walsh DM, Mathews PM, Ghiso J, Staufenbiel M, Walker LC, Jucker M (2006) Exogenous induction of cerebral beta-amyloidogenesis is governed by agent and host. Science 313: 1781–1784
58. Munch C, O'Brien J, Bertolotti A (2011) Prion-like propagation of mutant superoxide dismutase-1 misfolding in neuronal cells. Proc Natl Acad Sci 108: 3548–3553
59. Sundaramoorthy V, Walker AK, Yerbury J, Soo KY, Farg MA, Hoang V, Zeineddine R, Spencer D, Atkin JD (2013) Extracellular wildtype and mutant SOD1 induces ER–Golgi pathology characteristic of amyotrophic lateral sclerosis in neuronal cells. Cell Mol Life Sci 70: 4181–4195

60. Turner BJ, Atkin JD, Farg MA, Zang DW, Rembach A, Lopes EC, Patch JD, Hill AF, Cheema SS (2005) Impaired extracellular secretion of mutant superoxide dismutase 1 associates with neurotoxicity in familial amyotrophic lateral sclerosis. J Neurosci 25: 108–117

61. Haidet-Phillips AM, Hester ME, Miranda CJ, Meyer K, Braun L, Frakes A, Song S, Likhite S, Murtha MJ, Foust KD, Rao M, Eagle A, Kammesheidt A, Christensen A, Mendell JR, Burghes AH, Kaspar BK (2011) Astrocytes from familial and sporadic ALS patients are toxic to motor neurons. Nat Biotechnol 29: 824–828

62. Marchetto MCN, Muotri AR, Mu Y, Smith AM, Cezar GG, Gage FH (2008) Non-cell-autonomous effect of human SOD1G37R astrocytes on motor neurons derived from human embryonic stem cells. Cell Stem Cell 3: 649–657

63. Wang L, Deng H-X, Grisotti G, Zhai H, Siddique T, Roos RP (2009) Wild-type SOD1 overexpression accelerates disease onset of a G85R SOD1 mouse. Hum Mol Genet 18: 1642–1651

64. Chia R, Tattum MH, Jones S, Collinge J, Fisher EMC, Jackson GS (2010) Superoxide dismutase 1 and tgSOD1G93A mouse spinal cord seed fibrils, suggesting a propagative cell death mechanism in amyotrophic lateral sclerosis. PLoS One 5: e10627

65. Ayers JI, Fromholt S, Koch M, DeBosier A, McMahon B, Xu G, Borchelt DR (2014) Experimental transmissibility of mutant SOD1 motor neuron disease. Acta Neuropathol (Berl) 128: 791–803

66. Ayers JI, Fromholt SE, O'Neal VM, Diamond JH, Borchelt DR (2016) Prion-like propagation of mutant SOD1 misfolding and motor neuron disease spread along neuroanatomical pathways. Acta Neuropathol (Berl) 131: 103–114

67. Grad LI, Guest WC, Yanai A, Pokrishevsky E, O'Neill MA, Gibbs E, Semenchenko V, Yousefi M, Wishart DS, Plotkin SS, Cashman NR (2011) Intermolecular transmission of superoxide dismutase 1 misfolding in living cells. Proc Natl Acad Sci 108: 16398–16403

68. Grad LI, Yerbury JJ, Turner BJ, Guest WC, Pokrishevsky E, O'Neill MA, Yanai A, Silverman JM, Zeineddine R, Corcoran L, Kumita JR, Luheshi LM, Yousefi M, Coleman BM, Hill AF, Plotkin SS, Mackenzie IR, Cashman NR (2014) Intercellular propagated misfolding of wild-type Cu/Zn superoxide dismutase occurs *via* exosome-dependent and -independent mechanisms. Proc Natl Acad Sci 111: 3620–3625

69. Figley MD, Bieri G, Kolaitis R-M, Taylor JP, Gitler AD (2014). Profilin 1 associates with stress granules and ALS-linked mutations alter stress granule dynamics. J Neurosci 34: 8083–8097

70. Hart MP, Gitler AD (2012) ALS-associated ataxin 2 PolyQ Expansions enhance stress-induced caspase 3 activation and increase TDP-43 pathological modifications. J Neurosci 32: 9133–9142

71. Kato M, Han TW, Xie S, Shi K, Du X, Wu LC, Mirzaei H, Goldsmith EJ, Longgood J, Pei J, Grishin NV, Frantz DE, Schneider JW, Chen S, Li L, Sawaya MR, Eisenberg D, Tycko R, McKnight SL (2012) Cell-free formation of RNA granules: low complexity sequence domains form dynamic fibers within hydrogels. Cell 149: 7 53–767

72. Alami NH, Smith RB, Carrasco MA, Williams LA, Winborn CS, Han SS, Kiskinis E, Winborn B, Freibaum BD, Kanagaraj A, Clare AJ, Badders NM, Bilican B, Chaum E, Chandran S, Shaw CE, Eggan KC, Maniatis T, Taylor JP (2014) Axonal transport of TDP-43 mRNA granules is impaired by ALS-causing mutations. Neuron 81: 536–543

73. Arnold ES, Ling S-C, Huelga SC, Lagier-Tourenne C, Polymenidou M, Ditsworth D, Kordasiewicz HB, McAlonis-Downes M, Platoshyn O, Parone PA, Da Cruz S, Clutario KM, Swing D, Tessarollo L, Marsala M, Shaw CE, Yeo GW, Cleveland DW (2013) ALS-linked TDP-43 mutations produce aberrant RNA splicing and adult-onset motor neuron disease without aggregation or loss of nuclear TDP-43. Proc Natl Acad Sci 110: E736–E745

74. Ling S-C, Polymenidou M, Cleveland DW (2013) Converging mechanisms in ALS and FTD: disrupted RNA and protein homeostasis. Neuron 79: 416–438

75. Lagier-Tourenne C, Polymenidou M, Hutt KR, Vu AQ, Baughn M, Huelga SC, Clutario KM, Ling SC, Liang TY, Mazur C, Wancewicz E, Kim AS, Watt A, Freier S, Hicks GG, Donohue JP, Shiue L, Bennett CF, Ravits J, Cleveland DW, Yeo GW (2012) Divergent roles of ALS-linked proteins FUS/TLS and TDP-43 intersect in processing long pre-mRNAs. Nat Neurosci 15: 1488–1497

76. Polymenidou M, Lagier-Tourenne C, Hutt KR, Huelga SC, Moran J, Liang TY, Ling SC, Sun E, Wancewicz E, Mazur C, Kordasiewicz H, Sedaghat Y, Donohue JP, Shiue L, Bennett CF, Yeo GW, Cleveland DW (2011) Long pre-mRNA depletion and RNA missplicing contribute to neuronal vulnerability from loss of TDP-43. Nat Neurosci 14: 459–468

77. Kiskinis E, Sandoe J, Williams LA, Boulting GL, Moccia R, Wainger BJ, Han S, Peng T, Thams S, Mikkilineni S, Mellin C, Merkle FT, Davis-Dusenbery BN, Ziller M, Oakley D, Ichida J, Di Costanzo S, Atwater N, Maeder ML, Goodwin MJ, Nemesh J, Handsaker RE, Paull D, Noggle S, McCarroll SA, Joung JK, Woolf CJ, Brown RH, Eggan K (2014) Pathways disrupted in human ALS motor neurons identified through genetic correction of mutant SOD1. Cell Stem Cell 14: 781–795

78. Li Q, Vande Velde C, Israelson A, Xie J, Bailey AO, Dong M-Q, Chun SJ, Roy T, Winer L, Yates JR, Capaldi RA, Cleveland DW, Miller TM (2010) ALS-linked mutant superoxide dismutase 1 (SOD1) alters mitochondrial protein composition and decreases protein import. Proc Natl Acad Sci 107: 21146–21151

79. Liu J, Lillo C, Jonsson PA, Vande Velde C, Ward CM, Miller TM, Subramaniam JR, Rothstein JD, Marklund S, Andersen PM, Brännström T, Gredal O, Wong PC, Williams DS, Cleveland DW (2004) Toxicity of familial ALS-linked SOD1 mutants from selective recruitment to spinal mitochondria. Neuron 43: 5-17

80. Vande Velde C, McDonald KK, Boukhedimi Y, McAlonis-Downes M, Lobsiger CS, Bel Hadj S, Zandona A, Julien JP, Shah SB, Cleveland DW (2011) Misfolded SOD1 associated with motor neuron mitochondria alters mitochondrial shape and distribution prior to clinical onset. PLoS One 6: e22031

81. Moloney EB, de Winter F, Verhaagen J (2014) ALS as a distal axonopathy: molecular mechanisms affecting neuromuscular junction stability in the presymptomatic stages of the disease. Front Neurosci 8. doi: 10.3389/fnins.2014.00252

82. Amador-Ortiz C, Lin W-L, Ahmed Z, Personett D, Davies P, Duara R, Graff-Radford NR, Hutton ML, Dickson DW (2007) TDP-43 immunoreactivity in hippocampal sclerosis and Alzheimer's disease. Ann Neurol 61: 435–445

83. Arai T, Mackenzie IRA, Hasegawa M, Nonoka T, Niizato K, Tsuchiya K, Iritani S, Onaya M, Akiyama H (2009) Phosphorylated TDP-43 in Alzheimer's disease and dementia with Lewy bodies. Acta Neuropathol (Berl) 117: 125–136

84. Mackenzie IR, Rademakers R, Neumann M (2010) TDP-43 and FUS in amyotrophic lateral sclerosis and frontotemporal dementia. Lancet Neurol 9: 995–1007

85. Mizuno Y, Hori S, Kakizuka A, Okamoto K (2003) Vacuole-creating protein in neurodegenerative diseases in humans. Neurosci Lett 343: 77–80

86. Nizzardo M, Simone C, Rizzo F, Ulzi G, Ramirez A, Rizzuti M, Bordoni A, Bucchia M, Gatti S, Bresolin N, Comi GP, Corti S (2016) Morpholino-mediated SOD1 reduction ameliorates an amyotrophic lateral sclerosis disease phenotype. Sci Rep 6: 21301

87. Miller TM, Pestronk A, David W, Rothstein J, Simpson E, Appel SH, Andres PL, Mahoney K, Allred P, Alexander K, Ostrow LW, Schoenfeld D, Macklin EA, Norris DA, Manousakis G, Crisp M, Smith R, Bennett CF, Bishop KM, Cudkowicz ME (2013) An antisense oligonucleotide against SOD1 delivered intrathecally for patients with SOD1 familial amyotrophic lateral sclerosis: a phase 1, randomised, first-in-man study. Lancet Neurol 12: 435–442

88. Donnelly CJ, Zhang P-W, Pham JT, Haeusler AR, Mistry NA, Vidensky S, Daley EL, Poth EM, Hoover B, Fines DM, Maragakis N, Tienari PJ, Petrucelli L, Traynor BJ, Wang J, Rigo F, Bennett CF, Blackshaw S, Sattler R, Rothstein JD (2013) RNA toxicity from the ALS/FTD C9ORF72 expansion is mitigated by antisense intervention. Neuron 80: 415–248

89. Gros-Louis F, Soucy G, Larivière R, Julien J-P (2010) Intracerebroventricular infusion of monoclonal antibody or its derived Fab fragment against misfolded forms of SOD1 mutant delays mortality in a mouse model of ALS. J Neurochem. doi: 10.1111/j.1471-4159.2010.06683.x

90. Liu H-N, Tjostheim S, DaSilva K, Taylor D, Zhao B, Rakhit R, Brown M, Chakrabartty A, McLaurin J, Robertson J (2012) Targeting of Mono-

mer/misfolded SOD1 as a therapeutic strategy for amyotrophic lateral sclerosis. J Neurosci 32: 8791–8799

91. Urushitani M, Ezzi SA, Julien J-P (2007) Therapeutic effects of immunization with mutant superoxide dismutase in mice models of amyotrophic lateral sclerosis. Proc Natl Acad Sci 104: 2495–2500
92. Chen H, Qian K, Du Z, Cao J, Petersen A, Liu H, Blackbourn LW 4th, Huang CL, Errigo A, Yin Y, Lu J, Ayala M, Zhang SC (2014) Modeling ALS with iPSCs reveals that mutant SOD1 misregulates neurofilament balance in motor neurons. Cell Stem Cell 14: 796–809
93. de Boer AS, Koszka K, Kiskinis E, Suzuki N, Davis-Dusenbery BN, Eggan K (2014) Genetic validation of a therapeutic target in a mouse model of ALS. Sci Transl Med 6: 248ra104–248ra104
94. Yang YM, Gupta SK, Kim KJ, Powers BE, Cerqueira A, Wainger BJ, Ngo HD, Rosowski KA, Schein PA, Ackeifi CA, Arvanites AC, Davidow LS, Woolf CJ, Rubin LL (2013) A Small molecule screen in stem-cell-derived motor neurons identifies a kinase inhibitor as a candidate therapeutic for ALS. Cell Stem Cell 12: 713–726
95. Israelson A, Ditsworth D, Sun S, Song S, Liang J, Hruska-Plochan M, McAlonis-Downes M, Abu-Hamad S, Zoltsman G, Shani T, Maldonado M, Bui A, Navarro M, Zhou H, Marsala M, Kaspar BK, Da Cruz S, Cleveland DW (2015) Macrophage migration inhibitory factor as a chaperone inhibiting accumulation of misfolded SOD1. Neuron 86: 218–232
96. Novoselov SS, Mustill WJ, Gray AL, Dick JR, Kanuga N, Kalmar B, Greensmith L, Cheetham ME (2013) Molecular chaperone mediated late-stage neuroprotection in the SOD1G93A mouse model of amyotrophic lateral sclerosis. PLoS One 8: e73944
97. Nagy M, Fenton WA, Li D, Furtak K, Horwich AL (2016) Extended survival of misfolded G85R SOD1-linked ALS mice by transgenic expression of chaperone Hsp110. Proc Natl Acad Sci 201604885. doi: 10.1073/pnas.1604885113
98. Das I, Krzyzosiak A, Schneider K, Wrabetz L, D'Antonio M, Barry N, Sigurdardottir A, Bertolotti A (2015) Preventing proteostasis diseases by selective inhibition of a phosphatase regulatory subunit. Science 348: 239–242
99. Bulawa CE, Connelly S, DeVit M, Wang L, Weigel C, Fleming JA, Packman J, Powers ET, Wiseman RL, Foss TR, Wilson IA, Kelly JW, Labaudinière R (2012) Tafamidis, a potent and selective transthyretin kinetic stabilizer that inhibits the amyloid cascade. Proc Natl Acad Sci 109: 9629–9634
100. Brumshtein B, Esswein SR, Salwinski L, Phillips ML, Ly AT, Cascio D, Sawaya MR, Eisenberg DS (2015) Inhibition by small-molecule ligands of formation of amyloid fibrils of an immunoglobulin light chain variable domain. eLife 4. doi: 10.7554/eLife.10935
101. Auclair JR, Boggio KJ, Petsko GA, Ringe D, Agar JN (2010) Strategies for stabilizing superoxide dismutase (SOD1), the protein destabilized in the most common form of familial amyotrophic lateral sclerosis. Proc Natl Acad Sci 107: 21394–21399
102. Ray SS, Nowak RJ, Brown RH, Lansbury PT (2005) Small-molecule-mediated stabilization of familial amyotrophic lateral sclerosis-linked superoxide dismutase mutants against unfolding and aggregation. Proc Natl Acad Sci 102: 3639–3644
103. Wright GSA, Antonyuk SV, Kershaw NM, Strange RW, Samar Hasnain S (2013) Ligand binding and aggregation of pathogenic SOD1. Nat Commun 4: 1758

Aspekt toksyczności SOD1 w stwardnieniu zanikowym bocznym

Smriti Sangwan, David S. Eisenberg✉

Molecular Biology Institute and Howard Hughes Medical Institute, UCLA, Los Angeles CA, USA

✉ e-mail: david@mbi.ucla.edu

Słowa kluczowe: dysmutaza ponadtlenkowa; stwardnienie zanikowe boczne (ALS)

STRESZCZENIE

Stwardnienie zanikowe boczne (ALS) to śmiertelna choroba neurodegeneracyjna charakteryzująca się postępującą degeneracją neuronów motorycznych rdzenia kręgowego. Z ALS powiązano obecność mutacji w wielu białkach, jednak to dysmutazę ponadtlenkową 1 (SOD1) jako pierwszą powiązano z rozwojem ALS; jest ona odpowiedzialna za około 20% rodzinnych wystąpień tej choroby. U zwierząt doświadczalnych i w próbkach pobranych od pacjentów zmutowana forma SOD1 została wykryta w złogach cytoplazmatycznych, co świadczy o toksyczności jej agregatów. W niniejszym artykule przedstawiono różne hipotezy oparte na danych biochemicznych i strukturalnych wyjaśniające rozwój ALS związany ze zmutowaną formą SOD1. Choć molekularne mechanizmy leżące u podstaw toksyczności SOD1 są w znacznym stopniu nieznane, przedstawione modele mogą wskazywać na nowe możliwości opracowywania skutecznej terapii.

Chapter 2: Atomic structure of a toxic, oligomeric segment of SOD1 linked to amyotrophic lateral sclerosis (ALS)

Abstract: Fibrils and oligomers are the aggregated protein agents of neuronal dysfunction in Alzheimer's, Parkinson's and Lou Gehrig's (ALS) diseases. Whereas we now know much about fibril architecture, atomic structures of disease-related oligomers have eluded determination. Here we determine the corkscrew-like structure of a cytotoxic segment of SOD1 in its oligomeric state. Mutations that prevent formation of this structure eliminate cytotoxicity of SOD1 on primary motor neurons and in a *Danio Rerio* (zebrafish) model of ALS. Moreover, a novel antibody detects corkscrew-like epitopes in neural tissue samples collected from ALS patients. Our findings add to evidence that the toxic oligomeric entities in protein aggregation diseases contain antiparallel, out-of-register β-sheet structures, and identify a target for structure-based therapeutics for ALS.

Title: Atomic structure of a toxic, oligomeric segment of SOD1 linked to amyotrophic lateral sclerosis.

Authors:

Smriti Sangwan[1], Anni Zhao[1], Katrina L. Adams[2], Christina K. Jayson[3], Michael R. Sawaya[1], Elizabeth L. Guenther[1], Albert C. Pan[4], Jennifer Ngo[3], Destaye Moore[2], Angela B. Soriaga[1], Anand Panchal[7], Thanh D. Do[6], Lukasz Goldschmidt[1], Rebecca Nelson[1], Michael T Bowers[6], Mark Geisberg[7], Carla M. Koehler[3], David E. Shaw[4,5], Bennett G. Novitch[2], David S. Eisenberg[1,*]

Affiliations:

[1]Howard Hughes Medical Institute, UCLA-DOE and Molecular Biology Institutes, Department of Biological Chemistry Los Angeles, California, USA.

[2]Department of Neurobiology, Eli and Edythe Broad Center of Regenerative Medicine and Stem Cell Research, David Geffen School of Medicine at UCLA, Los Angeles, California, USA.

[3]Department of Chemistry & Biochemistry, UCLA, Los Angeles, California, USA.

[4]D. E. Shaw Research, New York, New York, USA.

[5]Department of Biochemistry and Molecular Biophysics, Columbia University, New York, New York, USA.

[6]Department of Chemistry, UC Santa Barbara, CA, USA.

[7]Silver Lake Research Corporation, Azusa, California, USA.

*Correspondence to: David Eisenberg, email: david@mbi.ucla.edu

Abstract: Fibrils and oligomers are the aggregated protein agents of neuronal dysfunction in Alzheimer's, Parkinson's and Lou Gehrig's (ALS) diseases. Whereas we now know much about fibril architecture, atomic structures of disease-related oligomers have eluded determination. Here we determine the corkscrew-like structure of a cytotoxic segment of SOD1 in its oligomeric state. Mutations that prevent formation of this structure eliminate cytotoxicity of SOD1 on primary motor neurons and in a *Danio Rerio* (zebrafish) model of ALS. Moreover, a novel antibody detects corkscrew-like epitopes in neural tissue samples collected from ALS patients. Our findings add to evidence that the toxic oligomeric entities in protein aggregation diseases contain antiparallel, out-of-register β-sheet structures, and identify a target for structure-based therapeutics for ALS.

Main Text:

Since Alzheimer's pioneering report in 1906, fibrillar protein deposits have been linked to neurodegenerative diseases. More recently, this link has been challenged by findings that transient, soluble oligomers formed by these proteins are cytotoxic (*1–3*). Whereas atomic- resolution structures of the spines of amyloid fibrils have shown tightly packed β-sheets with inter-digitated side chains (*4–9*), atomic-level details of toxic oligomers remain elusive. Various reports suggest that toxic intermediates formed by amyloid forming proteins consist of anti-parallel β sheet-rich structures (*10–15*). These reports utilized chemical cross-linking, analytical size exclusion, electron microscopy and FTIR, but no crystal structure of a toxic amyloid oligomer has been reported.

ALS is a debilitating disease, destroying spinal motor neurons and often leading to death within a few years of symptom onset. More than 160 different mutations in SOD1, a metal-binding, dimeric protein of 153 residues, are found in familial cases of ALS (*16*). SOD1 aggregation has also been implicated in sporadic ALS pathogenesis (*17*, *18*). Most of these SOD1 mutants show little change in enzymatic function suggesting that toxicity derives not from a loss of native function, but from a gain of toxic function (*19*, *20*). Transgenic mouse models of the familial mutants show motor neuron degeneration and stain positive for SOD1-containing inclusions, suggesting that protein aggregation is a mode of toxicity (*21–23*). Enrichment of oligomers has also been observed in cell culture (*24*, *25*) and in transgenic mice (*26*, *27*). However, a causal relationship between the appearance of aggregates and neuronal death has not been conclusively supported, and no atomic structure has been described for toxic oligomer of SOD1 or any other neurodegenerative-disease-related protein. Here we propose a structure for toxic oligomers formed by SOD1.

Crystal structure of the segment (residues 28-38) reveals an anti-parallel β sheet oligomer:

Based on mutational studies of others (*28–31*) and our own (see below), we focused on residues (28-38) of SOD1 as having the potential to form a toxic amyloid oligomer (Fig. S1, S2, S3, Supp. Text). To determine the structure of this segment we needed to increase its solubility. We achieved this by engineering a single residue replacement: proline to lysine at the N-terminal position 28. Rod-like crystals, 5 μm in one dimension appeared

overnight and upon further optimization yielded diffraction to 2.0 Å resolution. We phased the diffraction data by single isomorphous replacement with anomalous scattering (SIRAS) from crystals soaked in potassium iodide (Table S1). The crystal structure shows a twisted β-sheet built of antiparallel, out-of-register β-strands. Describing its shape, we term it the *corkscrew* (Fig. 1A). The exterior of the corkscrew is largely polar, while the hydrophobic interior is filled with aliphatic side chains of valine, leucine and isoleucine (Fig. 1A, right, S4). The N-terminal residues 29-35 form the β strand and the C-terminal residues, lysine, glycine and leucine form a beta-hairpin, which contributes weakly to the corkscrew assembly.

Corkscrew shows structural similarities to cylindrin, an oligomer of a non-pathogenic amyloid-forming protein (*32*). Similar to cylindrin, corkscrew is also composed of antiparallel β-strands that are out-of-register and form alternating weak and strong interfaces with neighboring β-strands (Fig. S5). The strong interface is composed of 9 inter-chain hydrogen bonds whereas the weak interface is composed of 7 hydrogen bonds - 1 intra-main chain and 6 inter-main chain hydrogen bonds. The buried surface area of one strand relative to the assembly (984 $Å^2$ vs 943 $Å^2$) and shape complementarity (0.79 vs 0.74) of the two structures are also comparable (Table S2). However, an important difference between the two architectures is that cylindrin is a closed barrel of 6 strands whereas corkscrew is an open barrel extending indefinitely as a twisted sheet, forming one complete turn every 16 strands. Oligomers formed by several other proteins such as α-synuclein, amyloid-β and HET-s have also been reported to be β-sheet rich (*11–13*, *33*). However, there is also evidence for polymorphism for the different oligomers that differ in size, architecture and toxic properties (*34–36*). Indeed, oligomeric structure of a single

protein can also differ depending on preparation conditions and consequently differ in biochemical properties (*37*). Taking the corkscrew structure described here, along with reports of amyloid oligomers described by others suggests that antiparallel, out-of-register β-strand architecture may be a common motif of amyloid oligomers (*13*, *34*, *38*).

From the crystal structure we observed that the N-terminal Lys28 replacing proline does not form any critical contacts and contributes only weakly to the crystal lattice contacts (Fig. S6A). Lys28 in the corkscrew structure is engaged in two hydrogen bonds; one with the C-terminal carboxylate and another with the carbonyl oxygen of Ser34. The native sequence maintains the same capacity for hydrogen bonds with these two hydrogen bond acceptors (Fig. S6B). Thus, the proline to lysine replacement has no effect on the corkscrew structure.

The segment 28-38 includes the longest stretch conserved in all known ALS cases and has been previously hypothesized to be important for aggregation (*28*). However, it also includes a number of familial mutations including the intensely studied, familial mutant, G37R and the rare mutants, V29A and V31A. From the crystal structure, we deduce that these mutations are compatible with the corkscrew structure.

We modeled the rest of full-length SOD1 around the corkscrew keeping the native tertiary structure of SOD1 intact. We used the apo-SOD1 monomeric structure as our starting model. Biochemical studies have noted that metal-depleted monomer is prevalent in patient tissues (*39–41*) as well as mice models (*27*, *42*) and is an intermediate in the conversion of native holo-SOD1 to pathological aggregates. We find that the remaining

residues can be accommodated with minimal change in secondary structure (Fig. 1B). Strands 2 and 3 detach from the monomer to allow corkscrew-like assemblies to form. While this model is currently speculative, it agrees with H/D exchange, molecular dynamics (MD) and mass spectrometry studies by others showing that most familial SOD1 mutants have minimal change in their secondary structure and contain a partially unfolded β-barrel at physiological temperature with local unfolding in β strand 3 corresponding to segment 29-36 (*29*, *43*).

We hypothesize that corkscrew-like oligomers of SOD1 resemble subsets of the indefinitely long twisted sheets modeled here on the framework of the corkscrew crystal structure. A single preferred oligomer size is not indicated by our structural model. Our observation that the corkscrew is composed of a single β-sheet, rather than several packed sheets as in amyloid fibrils, suggests that its fragmentation should be relatively facile, and would limit the size of SOD1 oligomers. Because our corkscrew-based model of SOD1 oligomers does not require the complete unfolding of SOD1, globular segments of SOD1 around the periphery of the corkscrew segment could block indefinite growth of the oligomer by shielding the sheet edges. Such a mechanism of limiting oligomer growth could not be observed in our crystal structure since the globular regions were excluded from crystallization.

Examining the corkscrew structure, we noticed that the glycine at position 6 (position 33 in full-length SOD1) is essential for corkscrew formation (Fig. 1C). Residues with larger side chains at position 33, such as tryptophan (Fig. 1D) cause steric clashes destabilizing the corkscrew structure. Consistent with this observation, in our all-atom MD simulations

the G33W mutant structure was less stable than the wild-type structure with both native proline and modified lysine residues at the N terminus (Fig. 1E, S7).

We also performed ion mobility mass spectrometry experiments to confirm that the segment forms oligomers in solution similar in cross-section to the crystal structure of the corkscrew (Supp text, Fig. S8, Table S3). The SOD1 segment was also observed to preferentially assemble into a corkscrew-like structure in our MD simulations (Fig. 1F, S9).

Segment (28-38) is necessary and sufficient for toxicity:

We next asked if the segment is cytotoxic and if the corkscrew structure underlies its toxicity. To examine cytotoxicity, we used embryonic stem-cell-derived motor neurons labeled with green fluorescent protein (*44*). The corkscrew-forming segment was aggregated and applied to motor neurons and cellular viability was measured upon overnight treatment. We found that viability was reduced by 60% compared to buffer-treated cells at physiologically relevant concentrations of 8-100 μM in a dose-dependent manner (Fig. 2A) (*45*). In contrast, the segment harboring a single G33W substitution that disrupts corkscrew formation did not induce any toxicity in cells at any concentration tested (Fig. 2B). We also tested replacement of Gly33 with a less bulky residue, valine, and found that it was also sufficient to alleviate toxicity of the segment (Fig. 2B, S10). The segment harboring the native proline residue is also cytotoxic and mutation at Gly33 to tryptophan or valine renders the peptide segment non-toxic (Fig. S11).

To further validate our hypothesis that the corkscrew structure forms the basis of SOD1-mediated toxicity in ALS, we studied two familial mutants of full-length SOD1 – A4V and G93A (*46*). We introduced the corkscrew-disrupting substitutions at Gly33 on the background of both of these familial mutations. Proteins were recombinantly expressed and aggregated by demetallation and agitation at 37°C for 12 hours, which produced a mixture of fibrils and oligomers. Motor neurons were treated with aggregated proteins overnight and cellular viability measured thereafter. A4V and G93A mutants were toxic to the cells at 8 μM, which appeared drastically degenerated compared to buffer-treated cells (Fig. 2C). By contrast, A4V/G33V, A4V/G33W, G93A/G33V and G93A/G33W proteins were non-toxic at the same concentration, and cellular morphologies were indistinguishable from those of the buffer-treated cells. We also quantified cellular viability, confirming that A4V and G93A were toxic to cells (Fig. 2D) and that the introduction of the corkscrew-disrupting substitutions at Gly33 alleviates their toxic effects. Together, these data suggest that the SOD1 segment (28-38) is both necessary and sufficient for motor neuron toxicity.

Toxicity of full-length SOD1 derives from soluble oligomers:

To determine whether the toxicity of full length SOD1 derives from soluble oligomers or insoluble fibrils, we tested the cytotoxic effects of the non-fibril-forming mutant (I104P) (26). While I104P protein did not form any mature fibrils (Fig. 2E), it was nevertheless toxic to motor neurons. The addition of the corkscrew-disrupting substitution G33W

alleviated this cytotoxicity (Fig. 2F, 2G). These results suggest that fibril formation is not essential for cytotoxicity.

To further investigate the origin of toxicity, we performed a series of experiments monitoring the aggregation kinetics of the various SOD1 mutants. In these experiments, we aggregated the proteins for different amounts of time and measured their cytotoxicity. We found that both familial mutants (A4V and G93A) were toxic to cultured neurons when aggregated for 12-16 hours and extended aggregation for 72 hours rendered the protein non-toxic (Fig. 2H, 2I). A4V/G33W and G93A/G33W were non-toxic irrespective of the duration of aggregation. Negative stain electron microscopy showed abundant fibrils in the samples aggregated for 72 hours and immunoblotting with the conformational oligomer specific antibody (A11) suggested samples aggregated for 72 hours contained no oligomers (Fig. S12). These results suggest that toxicity of aggregated SOD1 mutants derives from oligomers.

Several reports suggest that wt-SOD1 also aggregates in sporadic ALS (*47–49*). However, there is a lack of cellular and animal models that recapitulate wt-SOD1 (WT) toxicity and it is also not clear if WT and mutants have similar mechanisms of aggregation and toxicity. Therefore, we asked if WT differs in aggregation and toxicity from the familial mutants in our assays. To monitor the kinetics of fibril formation in these experiments, we used Thioflavin T, a dye that fluoresces upon binding to fibrils. The fibril-forming behavior of WT, G93A, and G33W constructs were similar, displaying a lag time of 2-4 hours, presumably during small-oligomer formation, followed by a short

log phase and then a plateau indicative of mature-fibrils (Fig. S13). We then performed the motor-neuron-cytotoxicity assay with protein aggregates from several time points. We found that WT or G93A protein samples that were allowed to aggregate for up to 12 hours were toxic to the motor neurons, whereas the same protein preparations that were aggregated for 16 hours or more exhibited no toxicity (Fig. S13A, S13B). Electron microscopy showed no mature fibrils in samples aggregated up to 12 hours (Fig. S13). In contrast, samples shaken for 16 hours or longer exhibited large fibril loads and were non-toxic to motor neurons. G33W, which cannot form the corkscrew, was non-toxic regardless of the extent of fibril formation (Fig. S13C). Thus, WT and mutant SOD1 share similar mechanisms of cytotoxicity that resides in residues (28-38) although other segments may enhance aggregation by initiating unfolding.

Taken together, our data suggest that toxicity of aggregated SOD1 derives specifically from oligomers that are off-pathway from fibrillation (Fig. S14). Our findings for SOD1 align with the hypotheses proposed by others for amyloid beta and huntingtin that large insoluble aggregates are relatively inert deposits (*50–53*).

Corkscrew disruption alleviates defects in a *Danio rerio* (zebrafish) ALS model:

To examine the effect of the corkscrew-disrupting mutation in vivo, we turned to a zebrafish model of ALS in which familial SOD1 mutants cause axonopathies (*54–57*). We expressed A4V SOD1 with and without the corkscrew-disrupting substitution at Gly33 in a zebrafish TDL6 line in which the primary motor neurons are labeled with GFP

and the mitochondria are labeled with dsRed (*58*). We analyzed motor axons at 2 days post fertilization (dpf). A4V caused 8% reduction in axon length (Fig. 3A, 3B) as has been previously shown (*56*), but A4V/G33V-injected fish had normal axon lengths (Fig. 3A, 3B). Additionally, we observed 30% of A4V but not the WT or double mutants injected embryos were severely deformed and could not be imaged suggesting that an acute phenotype is lethal (Fig. S15). We observed a similar phenotype upon expression of G93A – G93A-expressing zebrafish have 5% reduction in axon lengths while G93A/G33V expressing zebrafish were significantly better (Fig. 3C, 3D).

Defects in mitochondrial assembly and trafficking along with vacuolation (*59*, *60*) and abnormal clustering in neuronal processes (*61–64*) are established pathological phenotypes observed in transgenic mice, patient derived cells and other models. However, they have not been reported in any zebrafish model of ALS. Therefore we analyzed the mitochondrial morphology upon expression of SOD1 familial mutants. Expression of A4V mutant protein caused remarkable mitochondrial pathology characterized by abnormal clustering at the branch points indicative of defective mitochondria (Fig 3E) whereas A4V/G33V expressing fish had a mitochondrial network similar to WT fish. These defects were quantified by measuring the size and number of the mitochondria confirming that A4V had enlarged mitochondria (Fig 3F, S15) that were fewer in number (Fig 3G, S15). We also observed similar defects in the G93A-expressing zebrafish (Fig 3H, 3I, S15). Thus, disrupting the corkscrew segment alleviates ALS-linked axonopathies and mitochondrial defects in this *in vivo* model.

A novel antibody against corkscrew antigen recognizes apo-SOD1 oligomers:

We also found evidence that aggregated SOD1 in familial ALS patients exhibits a corkscrew-like epitope. From our model of full-length SOD1 oligomers, we observed that residues Val29, Val31, Gly33 and Ile35 are exposed at the ends of the corkscrew (Fig 4A). These residues are buried in the native SOD1 structure. We utilized this difference of solvent accessibility to develop an antibody (CSAb) specific for the corkscrew conformation. CSAb recognizes an epitope present in the oligomers of the segment but not in the fibrils (Fig. 4B, S16). CSAb does not recognize native dimeric SOD1 (Fig. 4C) or insoluble fibrils prepared by aggregation for 72 hours that are non-toxic (Fig. 4E). CSAb also fails to recognize denatured metal-bound SOD1 either purified recombinantly or from cell lysates although it recognizes denatured apo proteins (Fig. 4D). This selectivity on a denatured western blot suggests that there is some degree of conformational specificity associated with CSAb. CSAb also does not recognize the corkscrew disrupted G33W mutant proteins (Fig. S17). However, it recognizes toxic oligomers of apo-G93A prepared by aggregating for 12 hours (Fig. 4E, S16). Blue-native gel electrophoresis followed by western blotting showed that CSAb-positive oligomers are soluble and range from 30-100 kDa in mass, or about 2-6 monomers (Fig. 4F). Finally, we co-incubated 8 μM apo-G93A protein with 0.5 μM CSAb and found that it neutralized the toxicity of apo-G93A, supporting our conclusion that the segment (28-38) is a critical epitope for cytotoxicity (Fig. 4G).

We used CSAb to test for the presence of corkscrew oligomers in ALS and healthy human spinal cord specimens. CSAb positive staining was observed in the motor neurons of 4 out of 6 SOD1-linked fALS cases, 3 out of 6 sALS and 4 out of 5 non-SOD1 fALS but not in the healthy human subjects (Figure 4H, 4J, S18, Table S4). Interestingly, we also observed staining in non-neuronal cells, in particular, in 4 SOD1-linked fALS patients and in 3 non-SOD1 fALS subjects similar to previous reports (Fig. 4I, 4K) (*22*,*56*). Taken together, CSAb suggests that the SOD1 segment containing residues (28-38) is involved in the development of ALS, possibly in the corkscrew conformation.

In summary, we have identified an 11-residue segment in ALS-associated SOD1 that is necessary for its cytotoxicity. Our data support the hypothesis that SOD1 forms toxic oligomers composed of antiparallel, out-of-register β-sheet structures involving residues 28-38. This cytotoxic segment may be a target for developing structure-based ALS therapeutics.

References:

1. G. M. Shankar *et al.*, Amyloid-β protein dimers isolated directly from Alzheimer's brains impair synaptic plasticity and memory. *Nat. Med.* **14**, 837–842 (2008).

2. S. Baglioni *et al.*, Prefibrillar Amyloid Aggregates Could Be Generic Toxins in Higher Organisms. *J. Neurosci.* **26**, 8160–8167 (2006).

3. Y. S. Eisele *et al.*, Targeting protein aggregation for the treatment of degenerative diseases. *Nat. Rev. Drug Discov.* **14**, 759–780 (2015).

4. R. Nelson *et al.*, Structure of the cross-β spine of amyloid-like fibrils. *Nature*. **435**, 773–778 (2005).

5. M. R. Sawaya *et al.*, Atomic structures of amyloid cross-β spines reveal varied steric zippers. *Nature*. **447**, 453–457 (2007).

6. Y. Xiao *et al.*, Aβ(1–42) fibril structure illuminates self-recognition and replication of amyloid in Alzheimer's disease. *Nat. Struct. Mol. Biol.* **22**, 499–505 (2015).

7. M. T. Colvin *et al.*, Atomic Resolution Structure of Monomorphic $A\beta_{42}$ Amyloid Fibrils. *J. Am. Chem. Soc.* **138**, 9663–9674 (2016).

8. M. D. Tuttle *et al.*, Solid-state NMR structure of a pathogenic fibril of full-length human α-synuclein. *Nat. Struct. Mol. Biol.* **23**, 409–415 (2016).

9. M. A. Wälti *et al.*, Atomic-resolution structure of a disease-relevant Aβ(1–42) amyloid fibril. *Proc. Natl. Acad. Sci.* **113**, E4976–E4984 (2016).

10. Y. Zou, Y. Li, W. Hao, X. Hu, G. Ma, Parallel β-Sheet Fibril and Antiparallel β-Sheet Oligomer: New Insights into Amyloid Formation of Hen Egg White Lysozyme under Heat and Acidic Condition from FTIR Spectroscopy. *J. Phys. Chem. B*. **117**, 4003–4013 (2013).

11. K. Berthelot, H. P. Ta, J. Géan, S. Lecomte, C. Cullin, In Vivo and In Vitro Analyses of Toxic Mutants of HET-s: FTIR Antiparallel Signature Correlates with Amyloid Toxicity. *J. Mol. Biol.* **412**, 137–152 (2011).

12. M. S. Celej *et al.*, Toxic prefibrillar α-synuclein amyloid oligomers adopt a distinctive antiparallel β-sheet structure. *Biochem. J.* **443**, 719–726 (2012).

13. E. Cerf *et al.*, Antiparallel β-sheet: a signature structure of the oligomeric amyloid β-peptide. *Biochem. J.* **421**, 415–423 (2009).

14. A. Sandberg *et al.*, Stabilization of neurotoxic Alzheimer amyloid- oligomers by protein engineering. *Proc. Natl. Acad. Sci.* **107**, 15595–15600 (2010).

15. H. Wille, G. Drewes, J. Biernat, E.-M. Mandelkow, E. Mandelkow, Alzheimer-like paired helical filaments and antiparallel dimers formed from microtubule-associated protein tau in vitro. *J Cell Biol* (1992).

16. D. R. Rosen *et al.*, Mutations in Cu/Zn superoxide dismutase gene are associated with familial amyotrophic lateral sclerosis. *Nature*. **362**, 59–62 (1993).

17. Z.-Y. Zou, M.-S. Liu, X.-G. Li, L.-Y. Cui, Mutations in SOD1 and FUS caused juvenile-onset sporadic amyotrophic lateral sclerosis with aggressive progression. *Ann Transl Med* (2015).

18. P. Pasinelli, R. H. Brown, Molecular biology of amyotrophic lateral sclerosis: insights from genetics. *Nat. Rev. Neurosci.* **7**, 710–723 (2006).

19. M. Gurney *et al.*, Motor neuron degeneration in mice that express a human Cu,Zn superoxide dismutase mutation. *Science*. **264**, 1772–1775 (1994).

20. D. R. Borchelt *et al.*, Superoxide dismutase 1 with mutations linked to familial amyotrophic lateral sclerosis possesses significant activity. *Proc. Natl. Acad. Sci.* **91**, 8292–8296 (1994).

21. L. I. Bruijn, Aggregation and Motor Neuron Toxicity of an ALS-Linked SOD1 Mutant Independent from Wild-Type SOD1. *Science*. **281**, 1851–1854 (1998).

22. L. I. Bruijn *et al.*, ALS-Linked SOD1 Mutant G85R Mediates Damage to Astrocytes and Promotes Rapidly Progressive Disease with SOD1-Containing Inclusions. *Neuron*. **18**, 327–338 (1997).

23. Z. A. Oztug Durer *et al.*, Loss of Metal Ions, Disulfide Reduction and Mutations Related to Familial ALS Promote Formation of Amyloid-Like Aggregates from Superoxide Dismutase. *PLoS ONE*. **4**, e5004 (2009).

24. Y.-N. Park *et al.*, Huntingtin Fragments and SOD1 Mutants Form Soluble Oligomers in the Cell. *PLoS ONE*. **7**, e40329 (2012).

25. J. Kim *et al.*, Dimerization, Oligomerization, and Aggregation of Human Amyotrophic Lateral Sclerosis Copper/Zinc Superoxide Dismutase 1 Protein Mutant Forms in Live Cells. *J. Biol. Chem.* **289**, 15094–15103 (2014).

26. P. Zetterström *et al.*, Soluble misfolded subfractions of mutant superoxide dismutase-1s are enriched in spinal cords throughout life in murine ALS models. *Proc. Natl. Acad. Sci.* **104**, 14157–14162 (2007).

27. J. Wang *et al.*, Progressive aggregation despite chaperone associations of a mutant SOD1-YFP in transgenic mice that develop ALS. *Proc. Natl. Acad. Sci.* **106**, 1392–1397 (2009).

28. G. S. A. Wright, S. V. Antonyuk, N. M. Kershaw, R. W. Strange, S. Samar Hasnain, Ligand binding and aggregation of pathogenic SOD1. *Nat. Commun.* **4**, 1758 (2013).

29. A. Durazo *et al.*, Metal-free Superoxide Dismutase-1 and Three Different Amyotrophic Lateral Sclerosis Variants Share a Similar Partially Unfolded -Barrel at Physiological Temperature. *J. Biol. Chem.* **284**, 34382–34389 (2009).

30. B. F. Shaw *et al.*, Local Unfolding in a Destabilized, Pathogenic Variant of Superoxide Dismutase 1 Observed with H/D Exchange and Mass Spectrometry. *J. Biol. Chem.* **281**, 18167–18176 (2006).

31. D. M. Taylor *et al.*, Tryptophan 32 Potentiates Aggregation and Cytotoxicity of a Copper/Zinc Superoxide Dismutase Mutant Associated with Familial Amyotrophic Lateral Sclerosis. *J. Biol. Chem.* **282**, 16329–16335 (2007).

32. A. Laganowsky *et al.*, Atomic View of a Toxic Amyloid Small Oligomer. *Science*. **335**, 1228–1231 (2012).

33. T. D. Do *et al.*, Amyloid β-Protein C-Terminal Fragments: Formation of Cylindrins and β-Barrels. *J. Am. Chem. Soc.* **138**, 549–557 (2016).

34. P. Liu *et al.*, Quaternary Structure Defines a Large Class of Amyloid-β Oligomers Neutralized by Sequestration. *Cell Rep.* **11**, 1760–1771 (2015).

35. K. E. Marshall, L. C. Serpell, Fibres, crystals and polymorphism: the structural promiscuity of amyloidogenic peptides. *Soft Matter*. **6**, 2110 (2010).

36. J.-X. Lu *et al.*, Molecular Structure of β-Amyloid Fibrils in Alzheimer's Disease Brain Tissue. *Cell*. **154**, 1257–1268 (2013).

37. W. Paslawski, S. Mysling, K. Thomsen, T. J. D. Jørgensen, D. E. Otzen, Co-existence of Two Different α-Synuclein Oligomers with Different Core Structures Determined by Hydrogen/Deuterium Exchange Mass Spectrometry. *Angew. Chem. Int. Ed.* **53**, 7560–7563 (2014).

38. W. Hoyer, C. Gronwall, A. Jonsson, S. Stahl, T. Hard, Stabilization of a beta-hairpin in monomeric Alzheimer's amyloid- peptide inhibits amyloid formation. *Proc. Natl. Acad. Sci.* **105**, 5099–5104 (2008).

39. R. Rakhit *et al.*, An immunological epitope selective for pathological monomer-misfolded SOD1 in ALS. *Nat. Med.* **13**, 754–759 (2007).

40. H.-N. Liu *et al.*, Targeting of Monomer/Misfolded SOD1 as a Therapeutic Strategy for Amyotrophic Lateral Sclerosis. *J. Neurosci.* **32**, 8791–8799 (2012).

41. R. Rakhit *et al.*, Monomeric Cu,Zn-superoxide Dismutase Is a Common Misfolding Intermediate in the Oxidation Models of Sporadic and Familial Amyotrophic Lateral Sclerosis. *J. Biol. Chem.* **279**, 15499–15504 (2004).

42. H. L. Lelie *et al.*, Copper and Zinc Metallation Status of Copper-Zinc Superoxide Dismutase from Amyotrophic Lateral Sclerosis Transgenic Mice. *J. Biol. Chem.* **286**, 2795–2806 (2011).

43. J. S. Valentine, P. J. Hart, Misfolded CuZnSOD and amyotrophic lateral sclerosis. *Proc. Natl. Acad. Sci.* **100**, 3617–3622 (2003).

44. H. Wichterle, I. Lieberam, J. A. Porter, T. M. Jessell, Directed Differentiation of Embryonic Stem Cells into Motor Neurons. *Cell*. **110**, 385–397 (2002).

45. N. Kurobe, F. Suzuki, K. Okajima, K. Kato, Sensitive enzyme immunoassay for human Cu/Zn superoxide dismutase. *Clin. Chim. Acta*. **187**, 11–20 (1990).

46. Q. Wang, J. L. Johnson, N. Y. R. Agar, J. N. Agar, Protein Aggregation and Protein Instability Govern Familial Amyotrophic Lateral Sclerosis Patient Survival. *PLoS Biol.* **6**, e170 (2008).

47. A. Gruzman *et al.*, Common molecular signature in SOD1 for both sporadic and familial amyotrophic lateral sclerosis. *Proc. Natl. Acad. Sci.* **104**, 12524–12529 (2007).

48. K. Forsberg *et al.*, Novel Antibodies Reveal Inclusions Containing Non-Native SOD1 in Sporadic ALS Patients. *PLoS ONE*. **5**, e11552 (2010).

49. S. Guareschi *et al.*, An over-oxidized form of superoxide dismutase found in sporadic amyotrophic lateral sclerosis with bulbar onset shares a toxic mechanism with mutant SOD1. *Proc. Natl. Acad. Sci.* **109**, 5074–5079 (2012).

50. S. Treusch, D. M. Cyr, S. Lindquist, Amyloid deposits: Protection against toxic protein species? *Cell Cycle*. **8**, 1668–1674 (2009).

51. M. Arrasate, S. Mitra, E. S. Schweitzer, M. R. Segal, S. Finkbeiner, Inclusion body formation reduces levels of mutant huntingtin and the risk of neuronal death. *Nature*. **431**, 805–810 (2004).

52. I. Kuperstein *et al.*, Neurotoxicity of Alzheimer's disease Aβ peptides is induced by small changes in the Aβ42 to Aβ40 ratio. *EMBO J.* **29**, 3408–3420 (2010).

53. I. C. Martins *et al.*, Lipids revert inert Aβ amyloid fibrils to neurotoxic protofibrils that affect learning in mice. *EMBO J.* **27**, 224–233 (2008).

54. T. Ramesh *et al.*, A genetic model of amyotrophic lateral sclerosis in zebrafish displays phenotypic hallmarks of motoneuron disease. *Dis. Model. Mech.* **3**, 652–662 (2010).

55. S. A. Sakowski *et al.*, Neuromuscular effects of G93A-SOD1 expression in zebrafish. *Mol. Neurodegener.* **7**, 44 (2012).

56. A. Van Hoecke *et al.*, EPHA4 is a disease modifier of amyotrophic lateral sclerosis in animal models and in humans. *Nat. Med.* **18**, 1418–1422 (2012).

57. R. Lemmens *et al.*, Overexpression of mutant superoxide dismutase 1 causes a motor axonopathy in the zebrafish. *Hum. Mol. Genet.* **16**, 2359–2365 (2007).

58. M. P. Levesque, J. Krauss, C. Koehler, C. Boden, M. P. Harris, New Tools for the Identification of Developmentally Regulated Enhancer Regions in Embryonic and Adult Zebrafish. *Zebrafish*. **10**, 21–29 (2013).

59. P. C. Wong *et al.*, An adverse property of a familial ALS-linked SOD1 mutation causes motor neuron disease characterized by vacuolar degeneration of mitochondria. *Neuron*. **14**, 1105–1116 (1995).

60. P. Shi, J. Gal, D. M. Kwinter, X. Liu, H. Zhu, Mitochondrial dysfunction in amyotrophic lateral sclerosis. *Biochim. Biophys. Acta BBA - Mol. Basis Dis.* **1802**, 45–51 (2010).

61. E. Kiskinis *et al.*, Pathways Disrupted in Human ALS Motor Neurons Identified through Genetic Correction of Mutant SOD1. *Cell Stem Cell*. **14**, 781–795 (2014).

62. C. Vande Velde *et al.*, Misfolded SOD1 Associated with Motor Neuron Mitochondria Alters Mitochondrial Shape and Distribution Prior to Clinical Onset. *PLoS ONE*. **6**, e22031 (2011).

63. J. R. Sotelo-Silveira *et al.*, Axonal Mitochondrial Clusters Containing Mutant SOD1 in Transgenic Models of ALS. *Antioxid. Redox Signal.* **11**, 1535–1545 (2009).

64. J. Magrane, C. Cortez, W.-B. Gan, G. Manfredi, Abnormal mitochondrial transport and morphology are common pathological denominators in SOD1 and TDP43 ALS mouse models. *Hum. Mol. Genet.* **23**, 1413–1424 (2014).

65. K. Forsberg, P. M. Andersen, S. L. Marklund, T. Brännström, Glial nuclear aggregates of superoxide dismutase-1 are regularly present in patients with amyotrophic lateral sclerosis. *Acta Neuropathol. (Berl.)*. **121**, 623–634 (2011).

Acknowledgments: We thank Lisa Johnson, David Borchelt, Joan Valentine for discussions; Prof John Ravits and Prof Dennis Dickson for kindly providing the ALS patient tissues and Prof Negar Khanlou for help with histology; Hamilton Trinh, Michael Collazo, Duilio Cascio, and beam line staff at Argonne Photon Source (APS) for help with experiments. We thank HHMI, DOE, and NIH (AG029430) for support to DSE; UCLA Broad Center for Regenerative Medicine and Stem Cell Research and NINDS (NS072804), Muscular Dystrophy Association (92901) and California Institute for Regenerative Medicine (RB1-01367; RB5-07480 grants to BGN; RT307678 grant to CMK); NIGMS (GM61721) grants to CMK; NIH (AG047116) and NSF (CHE-1301032) grants to MTB. SS was supported by the Whitcome Pre-Doctoral fellowship; KLA by the UCLA CMB Training program (Ruth L. Kirschstein NIH GM00785), the UCLA-California Institute for Regenerative Medicine Training Grant, and a UCLA Graduate Division Dissertation Year Fellowship; RN by a Larry L. Hillblom Foundation fellowship and CKJ was a Beckman Research Scholar. Atomic coordinates and structure factors for the corkscrew have been deposited in the Protein Data Bank as 5DLI and 5IIW.

Author contributions: SS and DSE designed research and wrote the manuscript. SS and MRS determined the crystal structure. SS, AZ, ELG performed the biochemical and cytotoxicity assays. TDD performed the mass spectrometry experiments. SS and AP generated and characterized the antibody. CKJ and JN performed the zebrafish experiments. ACP performed the MD simulations. LG and RAN performed computational predictions. ABS assisted with structure data collection. KLA and DM assisted with the cell culture assays. MTB supervised the mass spectrometry experiments. MG supervised the antibody generation. DES supervised the simulation work. BGN supervised the cell culture assays. All authors contributed comments to the manuscript.

Figure Legends

Fig. 1. Structure of the corkscrew, an oligomer-forming segment of SOD1

(A) 2.0 Å resolution crystal structure of the SOD1 segment with sequence KVKVWGSIKGL shows antiparallel, out-of-register β-strands forming a continuous left-handed helix. Sixteen strands form one complete turn of the helix, with 25 Å outer diameter and 71 Å pitch. The hydrophobic interior lined with valine, isoleucine, and leucine side chains excludes water molecules, as shown in side and top views.

(B) Model of the SOD1 toxic oligomer built of 16 monomers on the spine of the corkscrew crystal structure. Strands 2 and 3 detach from the native SOD1 fold to form the corkscrew spine. The remaining protein decorates the exterior of corkscrew with much of the SOD1 structure intact. The model is shown in the same two orientations as (A). One monomer is colored in brown for clarity. Notice that the segment (28-38) is buried in the core but it is exposed at the edges.

(C) Val29 and Val31 of alternate β-strands form a hydrophobic interaction and are accommodated by the lack of a Gly33 side chain on the intervening strand.

(D) A PyMol-generated figure illustrates the steric clash caused by mutating Gly33 to tryptophan.

(E) All-atom MD simulations of the corkscrew-forming segment suggest that introduction of the G33W substitution destabilizes the structure. Blue and red curves correspond to Cα root-mean-square deviations (RMSD) from the corkscrew crystal structure in MD simulations of 8 chains of the corkscrew segment (KVKVWGSIKGL) and G33W mutant segment (KVKVWWSIKGL), respectively. The structure of the

corkscrew segment remained stable throughout the length of the simulation, whereas the G33W mutant deviated from the corkscrew structure.

(F) The SOD1(28-38) segment preferentially assembled into a corkscrew-like structure in MD simulation. MD simulations of weakly restrained monomers of SOD1 spontaneously assembled into a corkscrew-like structure. A snapshot of an assembled corkscrew-like structure from the MD simulations (green) is overlaid onto the crystal structure (blue). As a control, we found that monomers of the cylindrin-forming segment of αB crystallin spontaneously assembled into a cylindrin structure using the same simulation protocol (see SI text and Fig. S9 for additional simulation details).

Fig. 2. Corkscrew-forming segment (28-38) is necessary and sufficient for cytotoxicity

(A) Cell viability of motor neurons measured by MTT reduction assay shows that the corkscrew segment (KVKVWGSIKGL) is toxic to primary motor neurons in a dose-dependent manner. Statistical significance was analyzed using two tailed T-tests with Welch's correction.

(B) Corkscrew-forming segment (28-38) harboring single point substitutions at Gly33 (G33V and G33W) is non-toxic to motor neurons. All peptide segments were prepared identically and motor neurons were treated with different final concentrations. Statistical significance of G33 mutants was compared to the 28-38 segment by two-way ANOVA.

(C) Hb9-GFP labeled motor neurons treated with 8 μM aggregated full-length familial mutants (A4V and G93A) lose neurites but the corresponding double mutants

(G93A/G33V, G93A/G33W, A4V/G33V and A4V/G33W) are non-toxic and neurons look healthy. (Scale bar = 20 μm)

(D) Cell viability measured by MTT reduction assay confirming that the familial mutants A4V and G93A are toxic and substitution of Gly33 with Valine or Tryptophan renders the protein non-toxic. Statistical significance was analyzed by one-way ANOVA.

(E) Electron micrographs of a non-fibril forming SOD1 mutant (I104P) and the corresponding double mutant (I104P/G33W) show some aggregates but no large fibrils.

(F) Motor neurons treated with I104P lose neurites and have shrunken cell bodies (left) but I104P/G33W treated cells look healthy.

(G) Cell viability measured by MTT reduction assay confirmed that I104P is toxic and I104P/G33W is non-toxic. Statistical significance was analyzed using a two-tailed T-test with Welch's correction.

(H,I) The toxic properties of SOD1 mutants depend on the duration of aggregation. A4V and G93A mutants aggregated for 12-16 hours are toxic to motor neurons while extended agitation for 72 hours renders the proteins non-toxic. The corkscrew-disrupted proteins (A4V/G33W and G93A/G33W) are non-toxic irrespective of the duration of aggregation. Statistical significance was analyzed by two-tailed T-tests with Welch's correction. Results shown as Mean±SD (n=3). Symbols represent individual values of triplicates and bars represent average values. (*$p < 0.05$, (**$p<0.01$,***$p< 0.001$,****$p<.0001$).

Fig. 3. Corkscrew-disrupting substitution of G33V alleviates axonopathies in a *Danio Rerio* (zebrafish) ALS model

(A) Micrographs of zebrafish embryos at 2 dpf show reduction in axon length of A4V–expressing embryos, whereas corkscrew-disrupted A4V/G33V–expressing embryos have normal axon lengths. The first axon is highlighted in pink for clarity and axons measured for quantification are marked by an asterisk. Scale bar 100 μm.

(B) Quantification of axon lengths show that A4V–expressing embryos have shorter axons than WT-expressing embryos. The corkscrew-disrupting substitution G33V alleviates the defect. Results shown as Mean±SEM relative to WT for at least 72 embryos. Statistical significance was analyzed using one-way ANOVA.

(C) Micrographs of zebrafish embryos at 2 dpf show reduction in axon lengths of G93A–expressing embryos, whereas corkscrew-disrupted G93A/G33V–expressing embryos have normal axon lengths. The first axon is highlighted in pink for clarity, and axons measured for quantification are marked by an asterisk. Scale bar 100 μm.

(D) Quantifications of axon lengths show that G93A–expressing embryos have shorter axons than WT-expressing embryos. The corkscrew-disrupting substitution, G33V alleviates the defect. Results shown as Mean±SEM relative to WT for axons 12-16 of at least 73 embryos. Statistical significance was analyzed using one-way ANOVA.

(E) Micrographs show A4V-expressing zebrafish have impaired mitochondria which are clustered at the branch points (encircled) as compared to WT. Mitochondrial network of A4V/G33V-expressing embryos is similar to WT.

(F,G) Quantitative analysis of the mitochondrial network shows A4V-expressing fish have larger mitochondrial size (30.17 a.u.) and fewer mitochondria (32) in the axons indicative of defective fission whereas A4V/G33V (10.57 a.u. size and 54 mitochondria) expressing embryos have healthy mitochondria similar to WT (14.08 a.u. size and 58

mitochondria). Symbols represent individual measurements made in five motor neurons in 3 fish for each group. Statistical significance was analyzed by one-way ANOVA.

(H,I) Quantitative analysis of the mitochondria network show G93A-expressing fish have larger, diffused mitochondria (14.68 a.u. size and 39 mitochondria). Mitochondrial network of G93A/G33V (11.68 a.u. size and 59 mitochondria) expressing embryos is similar to WT (10.78 a.u. size and 78 mitochondria). Statistical significance was analyzed by one-way ANOVA.

Results shown as Mean±SEM. Symbols represent individual values and bars represent average values. (*p< 0.05, **p<0.01,***p< 0.001,****p<.0001).

Fig. 4. Corkscrew-based monoclonal antibody (CSAb) is reactive for SOD1 in fALS tissue sections.

(**A)** Solvent accessibility of the segment (28-38) (blue) in full-length SOD1 oligomers is evident in this space-filing model. In particular, residues Val29, Val31, Gly33 and Ile35 that are buried in the native SOD1 structure are exposed at the ends of the corkscrew model. Therefore, an antibody specific for the corkscrew conformation would recognize only oligomers and not native SOD1.

(B) CSAb detects oligomers (O) of the (28-38) segment but not fibrils. SODAb (a monoclonal antibody that recognizes the linear epitope corresponding to residues 24-36) was used to compare loading and electron microscopy was used to confirm the presence of fibrils (Fig. S16).

(**C**) Dot blot assay showing that CSAb does not detect native, dimeric metal-bound proteins.

(**D**) SDS-PAGE western blot shows CSAb does not recognize denatured recombinant protein or SOD1 extracted from cell lysates although it recognizes metal depleted apo-proteins.

(**E**) Dot blot assay showing CSAb does not recognize insoluble fibrils (F) (aggregated for 72 hours) but detects oligomers (O) (aggregated for 12 hours) of full-length apo-G93A (Refer Fig. S13 for toxicity). A11 antibody was used to confirm the presence of oligomers. SOD100 (a polyclonal antibody that recognizes all forms of SOD1) was used to compare loading and electron microscopy was used to confirm the presence of fibrils (Fig. S16).

(**F**) Blue-native PAGE western blot of the apo-G93A shows soluble oligomers recognized by CSAb range from approximately 30 kDa to 100 kDa, in size, and the fibrillar preparations have no detectable oligomers. The molecular weight of the SOD1 monomer is 17 kDa, so the oligomers range from about 2 to 6 monomers.

(**G**) CSAb neutralizes the toxicity of SOD1 oligomers. 8 μM apo-G93A protein aggregated for 12 hours was co-incubated for 2 hours with 0.5 μM CSAb or equal amounts of an unrelated IgG1 or buffer. The mixture was then applied to motor neurons and toxicity was measured after 24 hours by cellular morphology as well as by MTT reduction assay. Co-incubation with CSAb neutralizes the toxicity but equal volumes of buffer or unrelated IgG1 are ineffective suggesting that the epitope (28-38) is critical for cytotoxicity. Symbols represent individual measurements and bars represent average

values. Statistical significance was analyzed using one-way ANOVA (***p< 0.001, ns not significant).

(H, I) CSAb reactivity was tested in spinal cord tissues from 6 SOD1-linked fALS, 5 non-SOD1 linked fALS, 6 sALS and 10 control subjects. Cytoplasmic reactivity (marked by arrows) was observed in the motor neurons of majority of ALS subjects with strongest reactivity in SOD1-linked fALS subjects. Nuclear staining (marked by arrowheads) was observed in non-neuronal cells of fALS subjects but not in control or sALS subjects.

(J,K) Ratio of positive neuronal and non-neuronal cells in control, SOD1-linked fALS, non-SOD1 fALS and sALS (see Table. S4 for clinical information). Five fields of view in one section chosen randomly from 5 stained sections were counted per subject. Symbols represent individual measurements and bars represent average values. Statistical significance was analyzed using one-way ANOVA (**p<0.01,****p<0.0001, ns not significant).

Figures

Fig. 1

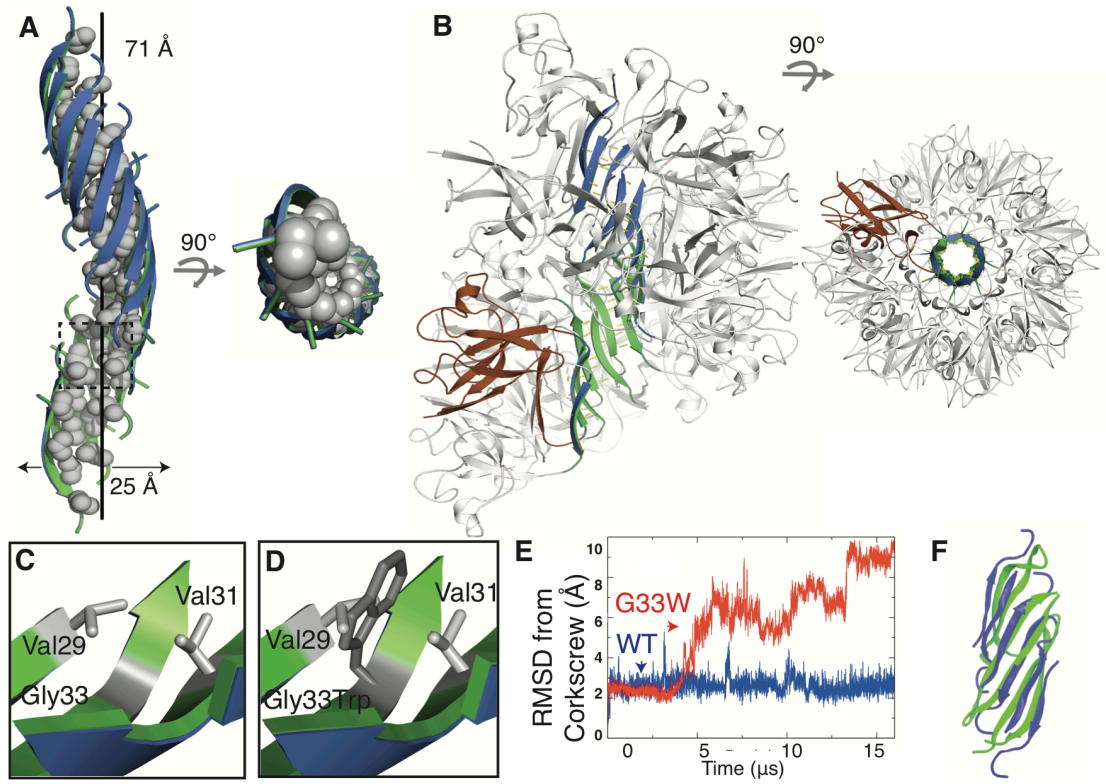

Fig. 2

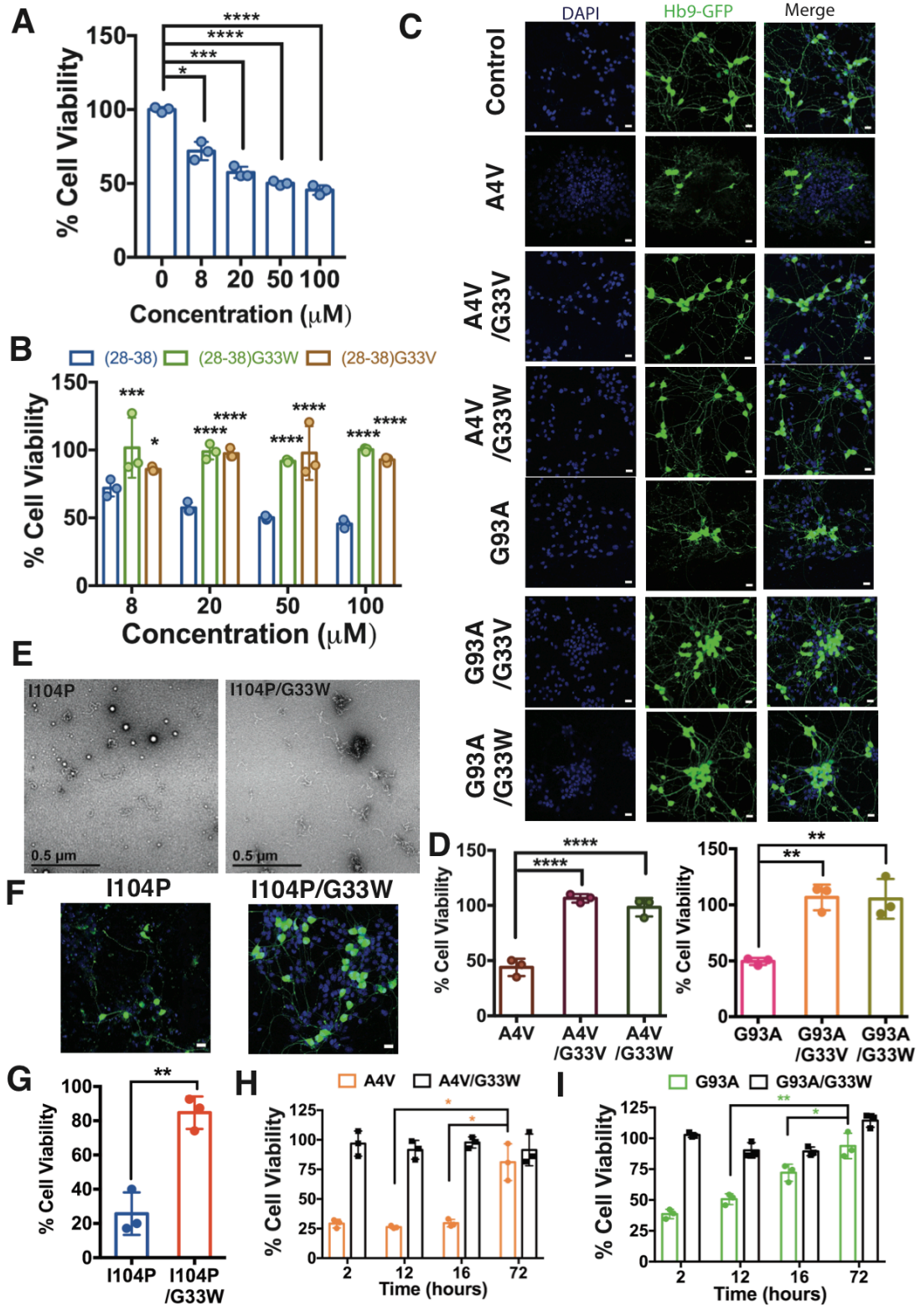
A
% Cell Viability
Concentration (μM)
B
(28-38)
(28-38)G33W
(28-38)G33V
% Cell Viability
Concentration (μM)
C
DAPI
Hb9-GFP
Merge
Control
A4V
A4V /G33V
A4V /G33W
G93A
G93A /G33V
G93A /G33W
D
% Cell Viability
A4V
A4V /G33V
A4V /G33W
G93A
G93A /G33V
G93A /G33W
E
I104P
I104P/G33W
0.5 μm
F
I104P
I104P/G33W
G
% Cell Viability
I104P
I104P /G33W
H
A4V
A4V/G33W
% Cell Viability
Time (hours)
I
G93A
G93A/G33W
% Cell Viability
Time (hours)

Fig.3

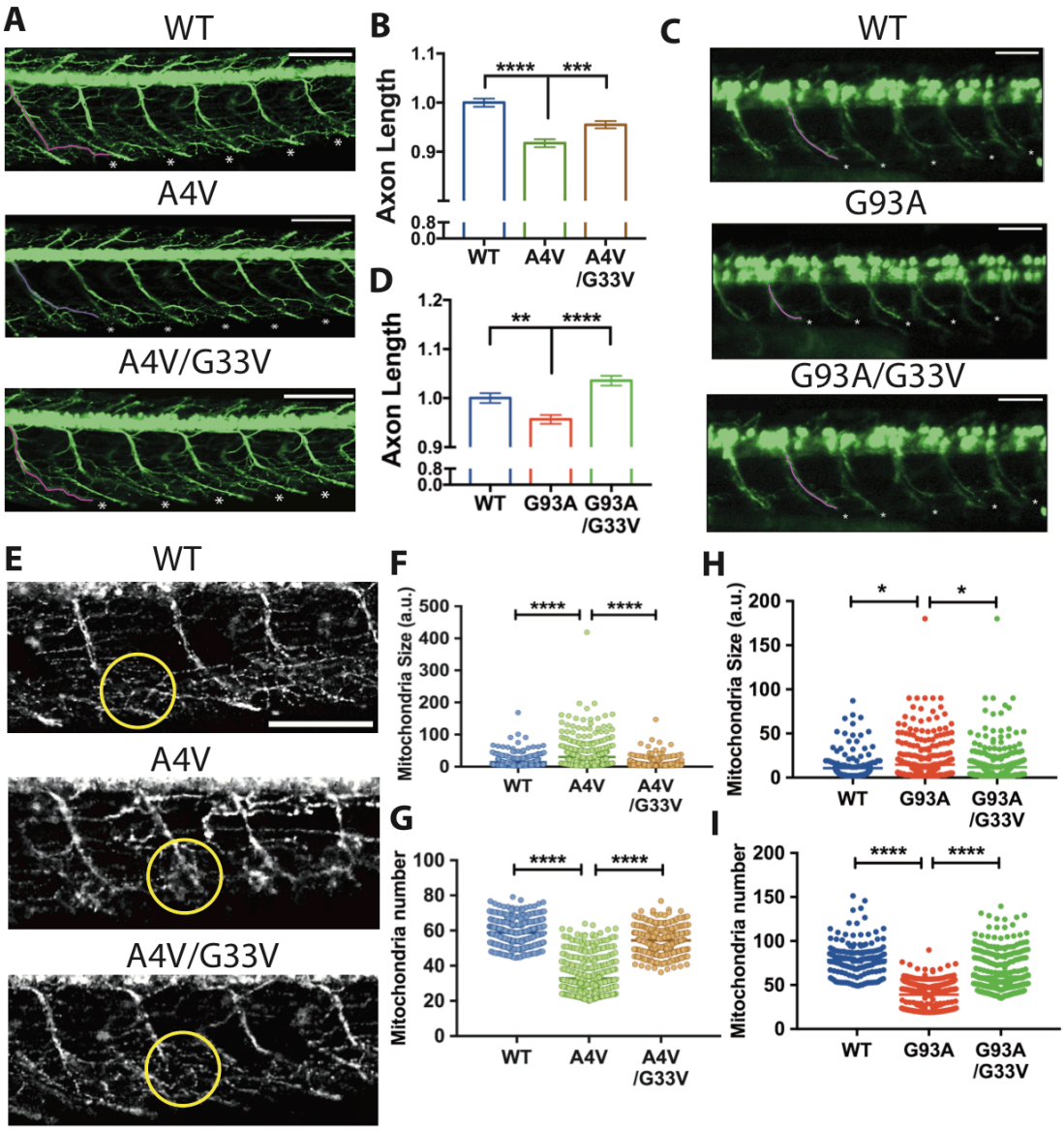
A
WT
A4V
A4V/G33V
B
Axon Length
****
***
WT
A4V
A4V /G33V
C
WT
G93A
G93A/G33V
D
Axon Length
**
****
WT
G93A
G93A /G33V
E
WT
A4V
A4V/G33V
F
Mitochondria Size (a.u.)
****
****
WT
A4V
A4V /G33V
G
Mitochondria number
****
****
WT
A4V
A4V /G33V
H
Mitochondria Size (a.u.)
*
*
WT
G93A
G93A /G33V
I
Mitochondria number
****
****
WT
G93A
G93A /G33V

Fig4.

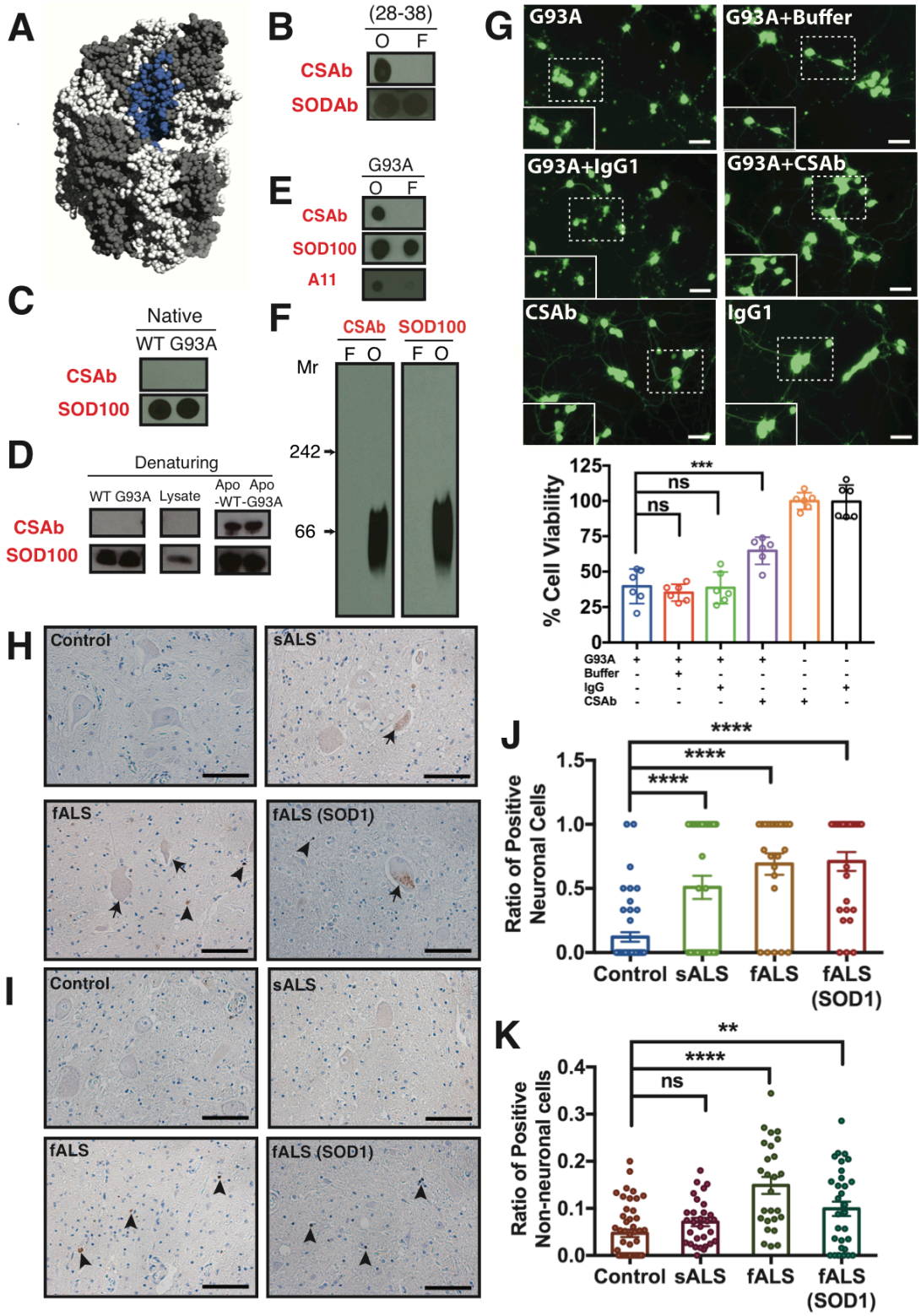
A
B
(28-38)
O F
CSAb
SODAb
C
Native
WT G93A
CSAb
SOD100
D
Denaturing
WT G93A
Lysate
Apo -WT-G93A
Apo -G93A
CSAb
SOD100
E
G93A
O F
CSAb
SOD100
A11
F
CSAb SOD100
F O F O
Mr
242
66
G
G93A
G93A+Buffer
G93A+IgG1
G93A+CSAb
CSAb
IgG1
% Cell Viability
125
100
75
50
25
0
***
ns
ns
G93A + + + + - -
Buffer - + - - - -
IgG - - + - - +
CSAb - - - + + -
H
Control
sALS
fALS
fALS (SOD1)
I
Control
sALS
fALS
fALS (SOD1)
J
Ratio of Positive Neuronal Cells
1.5
1.0
0.5
0.0
****
****
****
Control sALS fALS fALS (SOD1)
K
Ratio of Positive Non-neuronal cells
0.4
0.3
0.2
0.1
0.0
**
****
ns
Control sALS fALS fALS (SOD1)

Materials and Methods

SOD1(28-38) structure determination

Crystals of SOD1(28-38) with a P28K residue change were grown in hanging drop VDX plates (Hampton Research, Aliso, Viejo, CA). Lyophilized peptide at 98% purity (Genscript Inc.) was dissolved to 50mg/ml in 50mM Tris-base buffer. The reservoir solution contained 0.2M Na Citrate pH 5, 13% PEG 6000. Thick rod-like crystals appeared overnight and were allowed to grow for 2-3 days at ambient temperature in 2μL drops with a ratio of 2:1 peptide:reservoir. For heavy metal soaking, a 0.5M KI stock solution was made in the reservoir solution. The crystals were soaked for 30 seconds in a solution composed of a 2:1 ratio of the 0.5M KI stock solution to reservoir solution and 10% glycerol stock for cryoprotection. The crystals were subsequently flash frozen in liquid nitrogen. Single crystals were mounted with CrystalCap HT Cryoloops (Hampton Research, Aliso Viejo, CA). All data were collected at the Advanced Photon Source (Chicago, IL) on beamline 24-ID-E, which has a 5 μm microfocus beam suitable for the crystals. All data were processed using DENZO and SCALEPACK or XDS (*1*). Phases were obtained by heavy atom soaking and the structure was solved by SIRAS, followed by model building using COOT (*2*). All model refinement was done using REFMAC (*3*) and BUSTER (*4*). Figures were generated using PyMol (*5*). Unless stated otherwise, SOD1(28-38) in the text refers to KVKVWGSIKGL.

Molecular Dynamics simulations

We performed all-atom MD simulations of SOD1 and αB crystallin on Anton (*6*, *7*), a special-purpose computer designed to accelerate standard molecular dynamics simulations by orders of magnitude. Protein, water, and ions were represented explicitly, using the AMBER 99SB*-ILDN (*8–10*) force field and the TIP3P water model (*11*). Simulations of the SOD1 corkscrew were initiated from the crystal structure comprised of an eight-stranded corkscrew with either a wild-type (KVKVWGSIKGL and PVKVWGSIKGL) or G33W mutant (KVKVWWSIKGL and PVKVWWSIKGL) monomer sequence. Initial structures were placed in a cubic box 76 Å on each side and solvated with approximately 13,000 water molecules and 150 mM NaCl. The systems were minimized and then equilibrated in the NPT ensemble at 1 bar and 300 K for 50 ns with 5 kcal mol^{-1} $Å^{-2}$ harmonic position restraints applied to all non-hydrogen atoms of the protein; these restraints were tapered off linearly over 50 ns. Production runs were initiated from the final snapshot of the equilibration run and performed in the NVT ensemble using a 2.5-fs time step. Non-bonded interactions were truncated at 12 Å. The wild-type (KVKVWGSIKGL and PVKVWGSIKGL) and G33W mutant (KVKVWWSIKGL and PVKVWWSIKGL) corkscrew simulations were run for 16.4 μs, 13.8 μs, 16.6 μs and 15.2 μs, respectively. RMSDs in Figs. 1E and S7 were calculated on the hydrophobic core of the corkscrew (Cα atoms of residues 3 to 9, excluding the chains at the end).

SOD1 oligomer assembly simulations were initiated from three monomers of a tandem repeat structure (KVKVWGSIKGL--GG--KVKVWGSIKGL) built in homology to a monomer of the tandem repeat structure of αB crystallin cylindrin (PDB ID 3SGR (*12*)).

These monomers were separated in space by at least 30 Å, placed in a box 62 Å on each side, and solvated with approximately 7,600 water molecules and 150 mM NaCl. System preparation and simulations then proceeded as described above for the SOD1 corkscrew simulations. Each monomer was weakly restrained such that its Cα root-mean-square deviation (RMSD) was within approximately 2 Å of the starting structure. In particular, a flat-bottom harmonic restraint, *U*, was applied to each monomer such that $U(R) = \frac{1}{2}k(R - R_0)^2$ for $R > R_0$, and $U(R) = 0$ otherwise. Here, R is the RMSD from the initial structure, $R_0 = 2$ Å, and $k = 50$ kcal mol^{-1} Å^{-2}. The flat-bottom RMSD restraints limit the monomers' sampling of very collapsed structures and structures that have significantly reduced β-sheet content, and allow simulations to focus on discovering possible amyloid-like oligomers. We ran 20 assembly simulations beginning from the same starting conformation with different initial velocities drawn from a Maxwell-Boltzmann distribution. Of the twenty simulations, four were run for 4 μs and the rest were run for 1 μs.

The αB crystallin assembly simulations were initiated from three monomers of the tandem repeat structure of αB crystallin (GKLKVLGDVIEV--GG--KLKVLGDVIEV, PDB ID 3SGR). System preparation and simulation protocol were as above, except that we ran 10 assembly simulations in this case. Of these 10 simulations, two were run for 5 μs, two were run for 2 μs, and the rest were run for 1 μs.

Expression and purification of SOD1 constructs

All SOD1 constructs were expressed recombinantly using an *E. coli* system. All recombinant proteins are based on a SOD1 background strain that carries a C6A, C111S double mutation to simplify the purification. The SOD1 gene was inserted into the pET22b vector from Novagen with NcoI and SalI restriction enzyme digestion sites (gift from Professor Joan Valentine's lab at UCLA). Mutations in the SOD1 gene were made using the QuickChange Site-Directed mutagenesis Kit (Stratagene). The plasmid was transformed into the BL21(DE3)Gold (Agilent Technologies) expression strain. For expression, 10 ml LB + Amp (50mg/mL) was inoculated from frozen stock and grown overnight. 10 ml of starting culture was added to a 2L flask of 1L LB + Amp (50μg/mL) and grown for 3 hours at 37 °C to OD_{600} = 0.6. IPTG was then added to 1 mM and Zn^{2+} was added to 0.05 mM to induce protein expression, which continued for an additional 3 hours. The bacterial pellet was collected by centrifugation at 4000 rpm for 10 mins.

To purify SOD1 from the bacteria, osmotic shock was used to release proteins including SOD1 from the periplasm. First, the cell pellet was resuspended in 30 mL of 30 mM Tris-HCl pH 8 with 20% sucrose and stirred slowly for 20 mins. The cells were collected by centrifugation at 10,000 × g at 4°C for 10 mins. The pellet was then resuspended in 30 mL of ice-cold water and stirred slowly for 20 mins on ice to release periplasmic proteins. Next, cell debris was removed by centrifugation at 4°C for 10 mins at 10,000 × g. The contaminant proteins were then removed by precipitation with ammonium sulfate. 0.326 g/ml $(NH_4)_2SO_4$ was added to the supernatant, and the solution was stirred at 4°C for 45 mins. The protein was purified out of ammonium sulfate by separation over a phenyl

sepharose column. The column was equilibrated with buffer A (2 M $(NH_4)_2SO_4$, 0.15 M NaCl, 0.05 M KH_2PO_4, pH 7.0, adjusted with 1 M KOH) and buffer B (0.15 M NaCl, 0.05 M KH_2PO_4, pH 7.0, adjusted with 1 M KOH). The protein eluted at 6-30% buffer B. The protein was then concentrated and further purified by size exclusion chromatography on a silica G3000 column (Tosoh Bioscience). The column buffer comprised 0.1 M sodium sulfate, 25 mM sodium phosphate, and 1 mM sodium azide, pH 6.5.

SOD1 demetallation (required for aggregation)

The protein constructs purified by size exclusion chromatography were dialyzed in four buffers at 4°C to remove the bound metals. Protein preparations were put in a 10 kDa dialysis cassette and exchanged against buffer 1 twice (100mM Na Acetate pH 3.8**,** 10mM EDTA pH 8.0), followed by dialysis in buffer 2 **(**100mM Na Acetate pH 3.8, 100mM NaCl), buffer 3 **(**100mM Na Acetate pH 5.5, 100mM NaCl) for 4 hours, and finally in buffer 4 **(**20mM K phosphate pH7.0) for 12 hours each. To avoid metal contamination, all stock solutions (except for EDTA) were treated with Chelex 100 resin (Bio-Rad) to remove trace metals and all beakers were rinsed with metal-free water.

Protein and peptide aggregation

Full-length SOD1: Following metal removal, proteins were concentrated with a 10kDa concentrator to 800 μM (monomer) stock concentration and stored at -80 °C in 50μL aliquots until further use. Aggregation assays were carried out in 1.5 mL microcentrifuge tubes (Fisher Scientific) under acidic conditions with 80 μM SOD1,

50 mM sodium acetate, 1 mM EDTA and 1 mM TCEP, pH 3.5. Preparations were agitated at 900 rpm at 37 °C for indicated times. These samples were then dialysed with 10 mM potassium phosphate and 1 mM EDTA, pH 7.0 for 4 hours at 4 °C.

Peptide: Peptide segments were aggregated by incubation at 37°C for 12 hours with agitation in 50 mM tris-base buffer and added to cultured neurons.

Differentiation of mESCs to motor neurons

Hb9:eGFP mESCs were maintained and differentiated into motor neurons as previously described (*13*). Briefly, mESCs were first plated on gelatin to remove mouse embryonic fibroblasts (MEFs) prior to differentiation, and then plated in 60 mm bacterial petri dishes in core motor neuron medium (DMEM/F12, Neurobasal, 10% Knockout Serum Replacement, Pen-Strep, Glutamax) to induce embryoid body (EB) formation. Two days later, N2 supplement (1x), retinoic acid (1 μM; Sigma), and SAG (1 μM; Calbiochem) were added to the EBs. Media was changed every two days. After five days post-retinoic acid and SAG addition, Hb9:GFP EBs were dissociated using ice-cold 0.25% Trypsin-EDTA for 6 minutes at room temperature, followed by trituration in L-15 medium (Hyclone). Dissociated motor neurons were plated in core motor neuron medium with GDNF, BDNF, CNTF (all 10 ng/ml; Peprotech) on 96-well plates that were previously coated with poly-L-ornithine (0.01%; Sigma) and laminin (5 μg/ml; BD Biosciences) and incubated for 12-16 hrs before treatment with the SOD1 peptides or proteins. Approximately 80,000 cells were plated per well. All reagents are from Invitrogen, unless otherwise noted.

Cytotoxicity Assays

Peptide segments were dissolved in 50mM Tris (base) and aggregated by incubation at 37°C for 12 hours with agitation and then added to cultured neurons at the given final concentration. Unless stated otherwise, all full-length proteins were aggregated for 12 hours before adding to motor neurons at 8 μM final concentration. Motor neurons were incubated for 12-16 hrs and imaged (Axio Observer.D1 microscope, Zeiss), followed by cell viability assay. Cell viability was measured using the commercially available MTT assay (Promega Cat#G4100) according to the manufacturer's protocol with 4 hour incubation with the MTT reagent. All data were normalized using buffer as 100% viability and 0.2% SDS as 0% viability. Experiments were performed in triplicates and repeated a minimum of three times.

Electron Microscopy

3-5 μL sample was spotted directly on freshly glow-discharged carbon-coated electron microscopy grids (Ted Pella, Redding, CA). After 4 min incubation, grids were rinsed twice with 5μL distilled water and stained with 5μl of 2% uranyl acetate for 1 min. Excess uranyl acetate was removed by blotting and specimens were examined on a T-12 electron microscope at an accelerating voltage of 80 kV. Images were recorded digitally by wide angle (top mount) BioScan 600W 1 × 1K digital camera (Gatan, Pleasanton, CA).

Dot Blot Assay

3-5µL sample was spotted on a nitrocellulose membrane (Trans-Blot, Bio-Rad) followed by blocking with 10% fat-free milk in 1X TBST buffer (50 mM Tris, 150 mM NaCl, 0.05% Tween20) for 30 mins. Membranes were incubated with primary antibody – SOD100 (Enzo Life Sciences) at 1:1000 dilution, SODAb (gift by Prof. David Borchelt) at 1:5000 dilution, A11 (EMD Millipore) at 1:500, CSAb (in-house) at 1:500 diluted in 5% fat free milk in TBST buffer at room temperature for 1 hour. The membranes were washed three times in TBST buffer before incubating with HRP-linked secondary antibody - anti-mouse HRP secondary antibody (Life Technologies) at 1:10000 dilution, or anti-rabbit HRP secondary antibody (Life Technologies) at 1:10000 diluted in 5% fat-free milk in TBST buffer at room temperature for 1 hour. Pierce ECL Western Blotting Substrate, (Thermo Scientific, #32209), a chemiluminescent substrate was used for the detection of horseradish peroxidase (HRP) on the immunoblots following the manufacturer's instructions. Detailed protocol can be found on https://tools.thermofisher.com/content/sfs/manuals/MAN0011536_Pierce_ECL_West_Blot_Subs_UG.pdf

Thioflavin-T (ThT) Assay

Fibril formation assays were performed with 80 µM protein concentration in 50 mM sodium acetate buffer, 1 mM EDTA, 1 mM TCEP, pH 3.5 and 10 µM ThT – conditions identical to those used for aggregating proteins for the cytotoxicity assays, but with the addition of ThT. All assays were carried out in black Nunc 96-well optical bottom plates (Thermo Scientific). Plates were agitated at 300 rpm in 3-mm rotation diameter in a Varioskan microplate reader (Thermo) at 37 °C. Fluorescence measurements were

recorded every 30 mins using λ_{ex} = 444 nm, λ_{em} = 482 nm, with an integration time of 200 μs.

Mass Spectrometry

Peptide segments were dissolved in 20 mM ammonium acetate buffer (pH = 7) to the final concentration of 200 μM and incubated at room temperature without any agitation. Experiments were carried out at time t_0 and every day for a week and ion mobility was used to calculate the cross sections of oligomers. The peptide samples were nano-electrosprayed on a home-built, high-resolution ion mobility mass spectrometer (*14*) consisting of a source ion-funnel, a two-meter long drift cell, an exit funnel, a quadrupole mass analyzer and detectors. The ions were stored and focused in the source funnel and subsequently pulsed into the drift cell filled with helium gas at high pressure. A drift voltage was applied across the cell to create a weak electrical field. The ions moved forward under the influence of the electrical field, and at the same time experienced the drag force due to multiple collisions with helium buffer gas. An ion traveled with a constant velocity that reflected its size and shape. At the end of the drift cell, the ions were collected by an exit funnel where they were steered and focused into a quadrupole mass analyzer and detected as a function of arrival time in the arrival time distributions (ATDs). By measuring ATDs at different pressure to voltage (P/V) ratios, the absolute mobility of the ion of interest could be measured:

$$t_A = \frac{l^2}{K_0} \frac{273.16\ K}{760\ torr \cdot T} \cdot \frac{P}{V} + t_0 \ (Eq. 1)$$

In Eq. 1, l is the length of the drift cell, P is the gas pressure in torr, V is the voltage across the cell, and t_0 is the time the ions spend outside the drift cell before reaching the detector. The collision cross section σ can then be approximated from K_0 (*15*)

$$\sigma \approx \frac{3q}{16N}\left(\frac{2\pi}{\mu k_B T}\right)^{\frac{1}{2}}\frac{1}{K_0} \quad (Eq.2)$$

Here, N is the buffer gas density, μ is the reduced mass of the collision system (He+ion) and k_B is Boltzmann's constant. The cross section contains information about the three dimensional structure of the ion. In the ATDs shown in Fig. S8, underneath each experimental peak is a dotted line representing the peak shape expected for a single conformer (*16*) .

Zebrafish

All zebrafish (*Danio rerio*) were maintained in accordance with standard laboratory conditions (*17*). The University of California, Los Angeles (UCLA) Chancellor's Animal Research Committee approved all experiments performed on zebrafish. The TDL6 (Tübingen driver line) zebrafish used in all experiments were identified in a screen for developmentally regulated enhancers that drive tissue-specific expression. Gal4-driven GFP expression marks primary motor neurons. Mitochondria were marked by a TOL2-mediated insertion of a Gal4-UAS-MLSDsRed construct (*18*).

RNA production and injections

SOD1 constructs used for zebrafish expressions were the full-length sequence with Cys6 and Cys111 intact. The constructs (WT, G93A, G93A/G33V, A4V, A4V/G33V were

subcloned into pcGlobin2 vector and the constructs were linearized using XbaI to generate RNA. The Translation efficiency of the RNA of all constructs was tested by TnT® Quick Coupled Transcription/Translation System (Promega) using the manufacturer's instructions. Construct G93A/G33V has an additional mutation of I18G to prevent steric clashes due to the presence of G33V in the native SOD1 barrel. As a control we also tested the cytotoxicity of this construct in cell culture and found that it was non-toxic similar to G33V construct (Fig. S15B). RNA was transcribed using the mMessage Machine T7 kit (Ambion) and the mRNA was diluted to 500 ng/µL and 1000 ng/µL aliquots and stored at -80°C. 1 µL mRNA at 500 ng/µL (WT, G93A, G93A/G33V) and at 1000 ng/ µL (WT, A4V, A4V/G33V) was injected into TDL6 embryos from timed mating at the 1-4 cell stage. Embryos were incubated in 1x E3 buffer at 28.5 °C.

Analysis of axonopathy

At 2dpf zebrafish larvae microinjected with SOD1 constructs were anesthetized in 0.01% tricaine and imaged using a Leica MZ16F fluorescent stereoscope at 11.5X magnification. Observers were blinded and the length from the exit point of the spinal cord to the tip of the motor axon was measured for 5 axons per embryo corresponding to axons 12-16 using Fiji Simple Neurite Tracer. Experiments were repeated a minimum of three times and a total of 72 embryos were assessed for each construct.

Analysis of mitochondrial network

The mitochondrial network from the base of the spinal cord to the tip of the motor axon was imaged on a Leica TCS SP8 confocal microscope at 10X magnification with a 1.5X optical zoom. Images were processed with the Leica AF software and mitochondria size was measured for 5 axons per embryo using Fiji Image J Particle Analysis with the described algorithm (*19*). Before quantification, fluorescence from the spinal cord and regions outside of the larvae body were excluded. The program allowed automatic detection of isolated fluorescent spots by threshold and watershedding of binary formatted images without introducing user-bias. Spots with a circularity of 0.5-1 were selected to have their intensity and area quantified, where 1 is a complete circle. Intensity was quantified for each spot via overlapping gray levels and is reported as number of mitochondria as previously reported (*20*).

Protein expression in zebrafish

Protein expression was confirmed by western blotting (Fig. S15). Zebrafish embryos were pooled from each group at 2dpf and washed twice in Ringer's buffer (NaCl 135mM, KCl 5mM, $MgSO_4$ 1mM, K_2HPO_4 0.4mM, Glucose 5.5mM, HEPES 20mM pH 7.4). The embryos were subsequently deyolked, dechorionated and lysed in RIPA buffer (Sigma) (volume equals twice the number of embryos in μL) with Halt protease inhibitor cocktail EDTA-free (Thermo Scientific) added. Lysates were homogenized by sonication and protein concentration was determined using the BCA protein assay kit (Thermo Fisher Cat #23252). Equal amounts of protein were loaded on 12% Tris-glycine PAGE gels and transferred onto a PVDF membrane using an iBlot dry blotting system (Thermo Fisher) at

20V for 6 mins. Membranes were washed with methanol followed by water and then blocked with 10% fat free milk in TBST for 1hr at room temperature and washed three times with TBST buffer. Membranes were incubated with primary antibodies – SOD100 (Enzo Life sciences) at 1:500 dilution in 5% milk in TBST and incubated for 1hr at room temperature or anti β-actin (Abcam) at 1:1000 diluted in 5% milk in TBST and incubated overnight at 4°C. Membranes were first probed with SOD100 and then stripped using Restore PLUS Western Blot stripping buffer (Thermo Scientific) and subsequently probed with anti β-actin. Blots were washed thrice with 1X TBST and subsequently incubated with the secondary anti-rabbit HRP secondary antibody (Sigma) at a 1:2500 dilution in 5% milk in TBST for 1hr at room temperature. Pierce ECL Western Blotting Substrate, (Thermo Scientific, #32209), a chemiluminescent substrate was used for the detection of horseradish peroxidase (HRP) on the immunoblots following the manufacturer's instructions.

Antibody generation

Mice were immunized with 10 μg of synthetic peptide KVKVWGSIKGL dissolved in PBS and incubated 12 hours at 4°C. Boosts were performed bi-weekly for 4-8 weeks with the same dosages. Mice were sacrificed and splenocytes were fused with Sp2/0 myeloma cells (American Type Culture Collection cell line CRL-1581, Manassas, VA) (*21*). Following HAT selection, surviving clones were cultured in microwell plates and selected for production of IgG binding to peptide KVKVWGSIKGL. These screens were performed by indirect ELISA on culture supernatants and confirmed by dot blots with KVKVWGSIKGL peptide bound to nitrocellulose. Monoclonal antibody (MAb) CSAb

was identified by these criteria and the clone was stabilized by limiting dilution subcloning. MAb was produced from bulk hybridoma culture in medium with serum depleted of bovine IgG and purified by Protein G chromatography (Pierce Biotechnology, Rockford, IL).

Blue native gel electrophoresis

Samples were prepared by mixing with 4X NativePAGE sample buffer. For more details refer to the protocol for the Novex Native PAGE Bis-Tris Gel System (Thermo Fisher) (https://tools.thermofisher.com/content/sfs/manuals/nativepage_man.pdf). Briefly, equal amounts of proteins were loaded on 3-12% Bis-Tris native gels with light blue cathode buffer at 150 V for 2 hours. The protein was transferred to PVDF membranes using iBlot dry blotting system (Thermo Fisher) at 20V for 6 mins. Membranes were washed with methanol to remove Coommassie Blue and then washed with water. Membranes were then blocked with 10% fat-free milk in TBST for 1 hour at room temperature. Membranes were then washed three times with TBST and incubated with the primary antibody – SOD100 (Enzo Life Sciences) at 1:1000 dilution or CSAb (in-house) diluted 1:500 in 5% fat-free milk in TBST for 1 hour. Membranes were then washed with TBST three times and incubated with the secondary antibody – anti-mouse HRP secondary antibody (Life Technologies) at 1:10000 dilution or anti-rabbit HRP secondary antibody (Life Technologies) at 1:10000 dilution in 5% fat-free milk in TBST). Membranes were washed again three times with TBST and the films were developed following the protocol as described in the Kit (Thermo Scientific Pierce ECL Western Blotting Substrate, #32209).

Immunohistochemistry

Slides were deparaffinized by xylene followed by a series of washes in ethanol. After a wash under tap water, the slides were incubated in 3% hydrogen peroxide in methanol for 10 minutes. The slides were washed with distilled water and incubated for 10 minutes in EDTA Solution pH 8 (Invitrogen, #005501) at 95°C using a vegetable steamer. Following cool down to room temperature and washing with PBST (phosphate buffered saline containing 0.05% Tween-20), the slides were incubated at room temperature for 2 hours with anti-mouse CSAb antibody diluted 1:100 followed by Post Primary reagent of the Bond Refine Polymer Detection Kit (Leica, DS9800), for 30 minutes. Slides were rinsed with PBST and incubated with the Polymer reagent of the Bond Refine Polymer Detection Kit (Leica, DS9800), for 30 minutes, followed by incubation with DAB (3,3'-Diaminobenzidine) for visualization. Slides were counterstained with Harris' Hematoxylin, dehydrated in ethanol, and mounted with media.

Statistical Significance

All statistical analyses were done using GraphPad Prism 7.0.

Antibodies used

The following antibodies were used in this study. SOD100 (EnzoLife sciences) at 1:1000 dilution, SODAb (gift by Prof David Borchelt) at 1:5000 dilution, A11 (EMD Millipore) at 1:500 dilution, anti β-actin (Abcam) at 1:1000, CSAb (in-house) at 1:500 dilution, anti-

mouse HRP secondary antibody (Life technologies) 1:10000 dilution, anti-rabbit HRP secondary antibody (Life technologies) 1:10000 dilution.

Supplementary Text

Prediction of oligomer forming segments in SOD1

Several reports have suggested that oligomers formed by amyloid proteins have a pore or barrel shape and are composed of anti-parallel β strands (*22*, *23*). To investigate segments in SOD1 that may be critical for oligomer formation, we applied a combination of 3D-profiling and manual sequence fitting using a model of anti-parallel β sheet structure that we had previously discovered termed cylindrin (*12*) (Fig. S2). In order to predict which 11-residue segments of SOD1 might form a cylindrin-like structure, we analyzed the cylindrin structure by visual inspection and computational modeling. We examined the structural features of the native cylindrin, and compared these with cylindrin models of segments from other proteins. Our analysis followed three stages:

1. Computational prediction of cylindrin-compatible segments by 3D profiling

Using a process analogous to our 3D profile method for predicting steric-zipper-forming segments (*24*), we used the Rosetta modeling suite (*25*) for high-throughput computational modeling and prediction of cylindrin-forming segments (Figure S2A). Starting from the 6-stranded cylindrin barrel structure (from PDB 3SGO), we stripped off all side-chain atoms, then threaded on each 11-residue sequence segment of several amyloid proteins (The same 11-residue sequence segment was threaded onto each of the six strands of the cylindrin.). Side chains matching the amino acid sequence of the segment being threaded were attached to the backbone and repacked; this selects an energetically favorable rotamer at each position. The backbone was then randomly

perturbed by small sub-Angstrom moves, followed by repacking for up to 1000 iterations, or until energetic convergence. We then used the final, minimized Rosetta energy scores to rank the threaded protein segments—those with the lowest energy show the best compatibility with the cylindrin structure. The default Rosetta energy function (Talaris2013) was used.

2. Analysis of computational predictions and visual comparison with the native cylindrin

Among the lowest-energy computational predictions, one sequence feature immediately stood out – glycine at position 6. A closer look at the native cylindrin structure revealed why: glycine's lack of side chain provides room for the adjacent, inward-facing valine side chains (at position 4) to pack. As shown in Figure S2C, unrolling the cylindrin barrel to view the interior surface reveals a series of 'knobs' (valine 4 side chains, cyan) that can pack into 'holes' (green) provided by glycine. Without these glycine 'holes', the interior of the barrel would be too full, forcing the β-strands apart. A swap in the positions of knobs and holes (that is, moving glycine to position 4, and valine to position 6) might also be expected to allow the barrel to close. However, the computational modeling never gave low scores to segments with swapped knobs and holes. The reason we found is that the cylindrin backbone torsion angles at position 6 favor glycine.

Our analysis of the cylindrin's interior packing also highlighted the importance of the other inward-facing side chains, which pack in symmetric layers (Figure S2B). From the center, and moving outward, these are valine 4, valine 8, and valine 2. The valines form a hydrophobic core, which together with hydrophilic side chains on the exterior, likely

promote assembly of the cylindrin. Based on these observations, our expectation was that good candidates for cylindrin formation would have three features: (1) a glycine at either position 4 or 6; (2) segregated hydrophobic and hydrophilic residues, in inward- and outward-facing positions, respectively; and (3) appropriately sized inward-facing residues, to optimize packing in the small interior of the barrel.

We therefore went on to analyze the predicted structures of the lowest-energy models, to see whether our expectations matched the computational predictions. As mentioned above, all of the lowest-energy segments had glycine at position 6. Regarding segregation of hydrophobic and hydrophilic residues, there was no clear pattern. Some low-energy segments were nearly completely hydrophobic. Others had polar, or even charged, residues positioned in the interior. Some of these polar residues, such as asparagine, were positioned to largely fulfill potential hydrogen bonds. Others, such as serine and histidine, were generally not able to hydrogen bond with adjacent side chains, suggesting their segments are unlikely to form a cylindrin. We concluded that while Rosetta seemed well-able to handle steric considerations when packing side chains, it had more difficulty handling charge and hydrogen-bonding considerations.

The sizes and shapes of interior side chains in low-energy models fit better with our expectations. Valine, and similarly sized side chains like threonine and isoleucine, packed quite well (Figure S2D). Slightly larger side chains of methionine and histidine also fit (Figure S2E, F). Even larger side chains, such as phenylalanine, tyrosine, and tryptophan, were absent in top-scoring segments. Side chains smaller than valine, such as alanine,

serine, and even glycine, also came out in top-scoring segments (Figure S2G, H). Although these did not give rise to steric clashes, they did leave visible gaps in the interior, which we hypothesized would be less favorable than if the holes were filled (similar to the original cylindrin).

3. Manual selection of cylindrin-compatible segments

Although the 3D profile method provided a number of reasonable predictions, there were enough deviations from our expectations that we also performed a manual search for cylindrin-compatible segments (Figure S2I). We began by casting a wide net, using a sequence-based search to pull out any segments that matched either a basic pattern found in the cylindrin core sequence or in variations that we predicted were possible (for example, swapped 'knob' and 'hole' positions). Adjacent to the glycine 'hole', we restricted possible 'knob' residues to five: valine, isoleucine, leucine, methionine, and threonine. Sequences matching at least one of these basic patterns were then screened for clearly unfavorable features at other positions, and removed accordingly.

From an initial group of 143, 11-residue segments spanning the full sequence of SOD1, our screen yielded 4 overlapping sequences from the N-terminal region: segments 28-38, 30-40, 32-42, and 34-44. One of these, 32-42, was also predicted by our computational threading. A re-examination of the 28-38 segment showed that the small backbone movements allowed in our computational threading could not relieve a clash between the proline at position 1 and the position 11 leucine of the neighboring strand, without breaking apart the structure. As mentioned above inward facing glycines are critical for

the hydrophobic packing. Among the 4 segments, 28-38 was the only segment with glycine at position 6 that is conserved in ALS patients and contains a central stretch of amino acids that are conserved in ALS patients (Fig. S3). Interestingly, the segment has also been found to be prone to local unfolding by H/D exchange and mass spectrometry studies and small molecule inhibitors of aggregation are found to bind this segment (*26–28*). Keeping these reports in mind, the segment 28-38 was chosen for further characterization.

Mass assignment by ion-mobility mass spectrometry (IM-MS)

A detailed experimental workflow for IM-MS experiments has been described elsewhere (*29*, *30*). In this experiment, the ions were generated by n-ESI, stored in an ion-funnel, and subsequently pulsed into a drift cell filled with helium gas at P = 13 torr. The ions were moving through the drift cell toward the quadrupole mass analyzer under the influence of both a weak electrical field and a drag force caused by collisions with buffer gas. For the same oligomer with different conformations, those that are more extended will experience more collisions with the buffer gas, thus travel slower than those that are more compact. For oligomers with different sizes, species with higher charges are affected more by the electrical field ('drift' voltage) and travel faster than species with smaller charges. For example, a dimer with z = +2 charge will travel faster than a monomer with z = +1 charge, and the ATD (arrival time distribution) feature corresponding to the dimer will have a shorter arrival time than that of the monomer (*31*). By measuring the arrival times at different pressure to drift-voltage ratios, experimental collision cross sections can be measured for all features in the ATDs. The values can be compared to the cross sections obtained from theoretical modeling and x-ray crystallography.

The mass spectra of the cylindrin and corkscrew forming peptides are shown in Figure S8, panels A and B. Despite the difference in charge states in solution, major peaks with n/z = +1/2, +2/3, +1/1 and +5/4 were observed in the mass spectra for both peptides. SOD1(28-38) has additional peaks of n/z = +1/3 and +3/4. In addition, since SOD1(28-

38) is highly charged, salt-adduct peaks are also observed, which are absent in the mass spectra of the cylindrin segment.

We focused our analysis on the *n/z* = 1/1 mass spectral peaks of both segments since they contain multiple features that may correspond to large oligomers. First, we analyzed the ATD of the cylindrin segment, which has been shown to form hexamers by x-ray crystallography. The ATD shows multiple features (Fig. S8A), and we can unambiguously identify the monomer (σ = 268 Å^2) and dimer (σ = 440 Å^2) at 108.95 and 90.40 ms, respectively. The z = +1 monomer observed at this ATD has a similar cross section to z = +2 monomer at 599 m/z (σ = 263 – 274 Å^2, data not shown). Similarly, the cross section of z = +2 dimer is similar to z = +3 dimer at 799 m/z (σ = 442 – 452 Å^2, data not shown). The next peak at 85.5 ms is assigned a trimer with σ = 625 Å^2, as it does not fit a dimer. The spacing between the 75.75 ms peak and its adjacent peak at 85.5 ms (10.2 ms) is much larger than the spacing between dimer and trimer (4.85 ms). Thus, it cannot be classified as a tetramer and fits a hexamer with a cross section of 1122 Å^2. To resolve the size of the peak at 69.65 ms, we compared the mass spectra at different time points. The ATD of cylindrin after 24 hours shows a rearrangement in the peaks (Fig. S8D). The dimer and trimer peaks are essentially gone, while the hexamer peak at 75.75 ms is relatively unchanged. The peak at 69.65 ms increased in intensity, and no further peaks at shorter times have appeared. Hence the 69.65 ms peak is most likely the terminal stable soluble oligomer. The best assignment for the 69.95 ms peak is a compact hexamer with a cross section of 1020 – 1023 Å^2. If we use the X-ray coordinates of the cylindrin, we obtain a cross section of σ_{av} = 1029 Å^2 (σ_{av} is the average cross section obtained from

the trajectory and projected superposition approximation methods) (*30*, *32*, *33*), in excellent agreement with this assignment. Thus, it appears there are two stable hexamers of cylindrin, one open and one compact.

Next, we analyzed the mass spectra of SOD1(28-38). In this case, the n/z = 1/1 mass spectral peak initially appears to have a single, broad feature as its ATD (Fig S8E). After 24 hours, a more intense ATD is observed and now two features are resolved (Fig. S8F). Given our results for the cylindrin segment discussed above, the arrival times of these two features correspond to open (1189 $Å^2$) and compact (1113 $Å^2$) hexamers. The X-ray coordinates of SOD1(28-38) yield a cross section of σ_{av} = 1182 $Å^2$ that increases to 1226 $Å^2$ after 20-ns of MD relaxation, in good agreement with the experiments. Similar to the cylindrin segment, the terminal species appears to be a hexamer for SOD1(28-38). In addition, the compact feature in the ATD is broad suggesting numerous "cylindrin-like" structures. If we thread the sequence of SOD1(28-38) on the backbone of the cylindrin structure, we obtain a cross section of 1107 $Å^2$, which is near the σ_{av} = 1113 $Å^2$ experimental cross section calculated above. This calculation supports our assignment of the broad peak centered near 74 ms as a compact, cylindrin-like hexamer. Thus, in solution, SOD1(28-38) segment forms oligomers similar in cross section to the observed crystal structure of the corkscrew and a more closed, cylindrin-like structure.

References:

1. W. Kabsch, Automatic processing of rotation diffraction data from crystals of initially unknown symmetry and cell constants. *J. Appl. Crystallogr.* **26**, 795–800 (1993).

2. P. Emsley, K. Cowtan, *Coot* : model-building tools for molecular graphics. *Acta Crystallogr. D Biol. Crystallogr.* **60**, 2126–2132 (2004).

3. A. A. Vagin *et al.*, *REFMAC* 5 dictionary: organization of prior chemical knowledge and guidelines for its use. *Acta Crystallogr. D Biol. Crystallogr.* **60**, 2184–2195 (2004).

4. G. Bricogne *et al.*, BUSTER version 1.10.0. Cambridge, United Kingdom: Global Phasing Ltd.

5. W. Delano, The PyMOL Molecular Graphics System. (2002).

6. D. E. Shaw *et al.*, (ACM Press, 2009; http://dl.acm.org/citation.cfm?doid=1654059.1654099), p. 1.

7. D. E. Shaw *et al.*, (IEEE, 2014; http://ieeexplore.ieee.org/lpdocs/epic03/wrapper.htm?arnumber=7012191), pp. 41–53.

8. V. Hornak *et al.*, Comparison of multiple Amber force fields and development of improved protein backbone parameters. *Proteins Struct. Funct. Bioinforma.* **65**, 712–725 (2006).

9. R. B. Best, G. Hummer, Optimized Molecular Dynamics Force Fields Applied to the Helix−Coil Transition of Polypeptides. *J. Phys. Chem. B*. **113**, 9004–9015 (2009).

10. K. Lindorff-Larsen *et al.*, *Proteins Struct. Funct. Bioinforma.*, in press, doi:10.1002/prot.22711.

11. W. L. Jorgensen, J. Chandrasekhar, J. D. Madura, R. W. Impey, M. L. Klein, Comparison of simple potential functions for simulating liquid water. *J. Chem. Phys.* **79**, 926 (1983).

12. A. Laganowsky *et al.*, Atomic View of a Toxic Amyloid Small Oligomer. *Science*. **335**, 1228–1231 (2012).

13. H. Wichterle, I. Lieberam, J. A. Porter, T. M. Jessell, Directed Differentiation of Embryonic Stem Cells into Motor Neurons. *Cell*. **110**, 385–397 (2002).

14. P. R. Kemper, N. F. Dupuis, M. T. Bowers, A new, higher resolution, ion mobility mass spectrometer. *Int. J. Mass Spectrom.* **287**, 46–57 (2009).

15. *Transport properties of ions in gases*.

16. J. Gidden, A. Ferzoco, E. S. Baker, M. T. Bowers, Duplex Formation and the Onset of Helicity in Poly d(CG)n Oligonucleotides in a Solvent-Free Environment (2004).

17. *Westerfield, M. The Zebrafish Book. The University of Oregon Press, Eugene, Oregon. (2003)*.

18. M. P. Levesque, J. Krauss, C. Koehler, C. Boden, M. P. Harris, New Tools for the Identification of Developmentally Regulated Enhancer Regions in Embryonic and Adult Zebrafish. *Zebrafish*. **10**, 21–29 (2013).

19. B. Sankur, Survey over image thresholding techniques and quantitative performance evaluation. *J. Electron. Imaging*. **13**, 146 (2004).

20. A. D. Pilling, Kinesin-1 and Dynein Are the Primary Motors for Fast Transport of Mitochondria in Drosophila Motor Axons. *Mol. Biol. Cell*. **17**, 2057–2068 (2006).

21. E. A. Greenfield, *Antibodies: A Laboratory Manual, Second edition*.

22. R. Kayed, Common Structure of Soluble Amyloid Oligomers Implies Common Mechanism of Pathogenesis. *Science*. **300**, 486–489 (2003).

23. A. Sandberg *et al.*, Stabilization of neurotoxic Alzheimer amyloid- oligomers by protein engineering. *Proc. Natl. Acad. Sci.* **107**, 15595–15600 (2010).

24. M. J. Thompson *et al.*, The 3D profile method for identifying fibril-forming segments of proteins. *Proc. Natl. Acad. Sci.* **103**, 4074–4078 (2006).

25. A. Leaver-Fay *et al.*, in *Methods in Enzymology* (Elsevier, 2011; http://linkinghub.elsevier.com/retrieve/pii/B9780123812704000196), vol. 487, pp. 545–574.

26. L. Banci *et al.*, Metal-free superoxide dismutase forms soluble oligomers under physiological conditions: A possible general mechanism for familial ALS. *Proc. Natl. Acad. Sci.* **104**, 11263–11267 (2007).

27. A. Durazo *et al.*, Metal-free Superoxide Dismutase-1 and Three Different Amyotrophic Lateral Sclerosis Variants Share a Similar Partially Unfolded -Barrel at Physiological Temperature. *J. Biol. Chem.* **284**, 34382–34389 (2009).

28. G. S. A. Wright, S. V. Antonyuk, N. M. Kershaw, R. W. Strange, S. Samar Hasnain, Ligand binding and aggregation of pathogenic SOD1. *Nat. Commun.* **4**, 1758 (2013).

29. S. L. Bernstein *et al.*, Amyloid-β protein oligomerization and the importance of tetramers and dodecamers in the aetiology of Alzheimer's disease. *Nat. Chem.* **1**, 326–331 (2009).

30. C. Bleiholder, N. F. Dupuis, T. Wyttenbach, M. T. Bowers, Ion mobility–mass spectrometry reveals a conformational conversion from random assembly to β-sheet in amyloid fibril formation. *Nat. Chem.* **3**, 172–177 (2011).

31. S. L. Bernstein *et al.*, Amyloid β-Protein: Monomer Structure and Early Aggregation States of Aβ42 and Its Pro ^{19} Alloform. *J. Am. Chem. Soc.* **127**, 2075–2084 (2005).

32. M. F. Mesleh, J. M. Hunter, A. A. Shvartsburg, G. C. Schatz, M. F. Jarrold, Structural Information from Ion Mobility Measurements: Effects of the Long-Range Potential. *J. Phys. Chem.* **100**, 16082–16086 (1996).

33. C. Bleiholder, S. Contreras, T. D. Do, M. T. Bowers, A novel projection approximation algorithm for the fast and accurate computation of molecular collision cross sections (II). Model parameterization and definition of empirical shape factors for proteins. *Int. J. Mass Spectrom.* **345-347**, 89–96 (2013).

Supplemental figures:

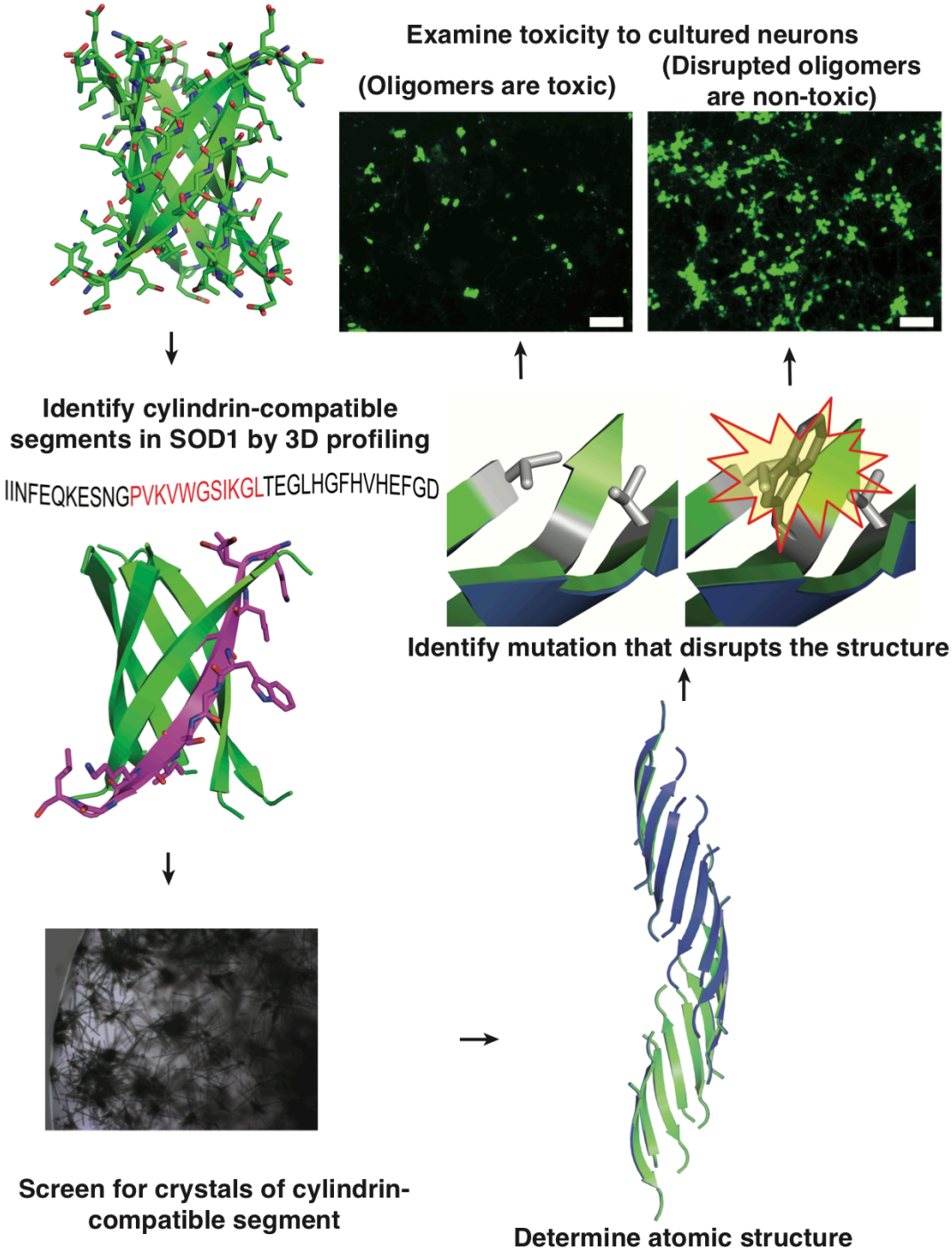

Fig. S1. Discovery of a cytotoxic segment of SOD1. Starting from the cylindrin backbone structure, sequences of SOD1 were examined for structural compatibility. The segment SOD1(28-38) was found to be compatible, and was put into crystallization trials,

and the atomic structure was determined. The significance of the structure to SOD1-linked cytotoxicity was then tested by introducing mutations designed to disrupt the structure.

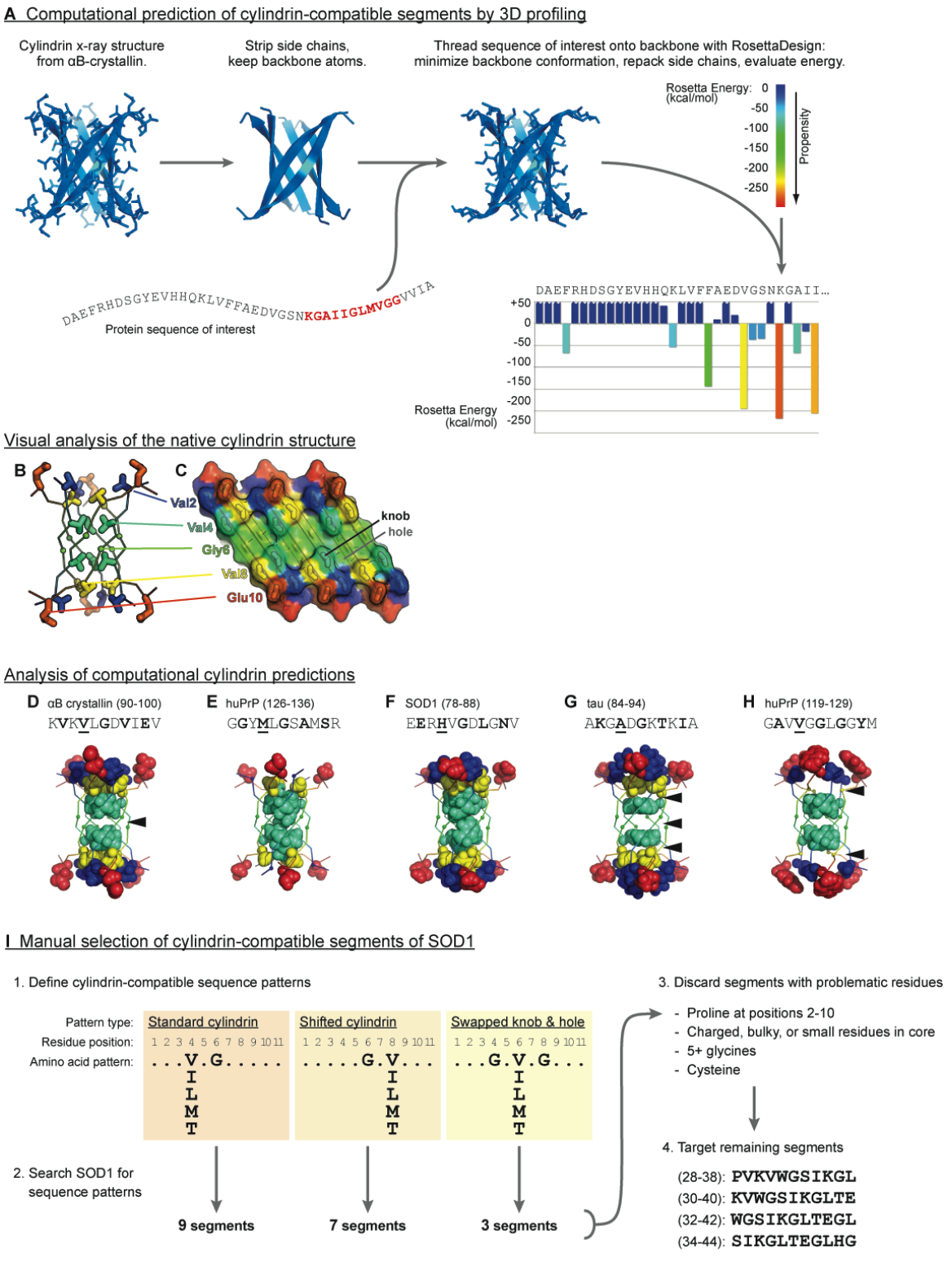

Fig. S2. Prediction of cylindrin-compatible segments

(A) 3D profile method for predicting cylindrin-compatible segments in amyloid proteins. An example of threading with the amyloid-β peptide is shown.

(B,C) Visual analysis of the cylindrin structure revealed a layering of side chains in the core (**B**; backbone shown as a line, with even-numbered, 'inward-facing' side chains shown as sticks, and glycine Cα shown as a small sphere), and a 'knob in hole' packing of valine and glycine residues (**C**; surface rendering) that allows for the small circumference of the barrel.

(D-H) Structures resulting from the 3D profile predictions were analyzed for packing in the barrel core. Representation is similar to panel **B**, but with side-chain atoms represented by spheres with van der Waals radii. The protein of origin and segment sequence are given, with even-numbered, 'inward-facing' residues in bold, and the critical position 4 residue underlined. (**D)** The original cylindrin structure, after Rosetta-based side-chain repacking and energy minimization. Notice the packing of valine 4, cyan, near the center. Although there is a gap between the two layers (arrowhead), it is small. (**E)** In this model of a segment from the human prion protein, methionine (cyan) occupies the central position 4, filling the space more than valine of the cylindrin sequence. (**F)** A histidine side chain at position 4 can also fill the central space, but is not able to satisfy hydrogen bonding groups. (**G)** Alanine at position 4 does not fill the core as well, leaving gaps (arrowheads). (**H)** Adjacent alanine and glycine, at positions 2 and 8 respectively, leave large gaps in outer layers of the cylindrin model core (arrowheads), in spite of a native valine packing in the middle at position 4.

(I) Manual selection of cylindrin-compatible segments. First, three sequence-based criteria, which define the glycine position and the position of an adjacent, appropriate

side chain (with cylindrin-compatible size and charge) in the core, were used in the initial selection of segments. The resulting sequences were further culled based on the presence of undesirable amino acids in specific positions. Prolines were avoided because of their tendency to disrupt β-structure. Charged and bulky inward-facing residues were avoided because of likely disruption to the packing. Small inward-facing residues were avoided because of gaps in packing, *e.g.* as in panel **H** Large numbers of glycines were avoided because of the tendency for these sequences to be flexible rather than adopt a fixed conformation. Cysteines were avoided for experimental purposes. Four overlapping segments of SOD1 resulted from this manual selection.

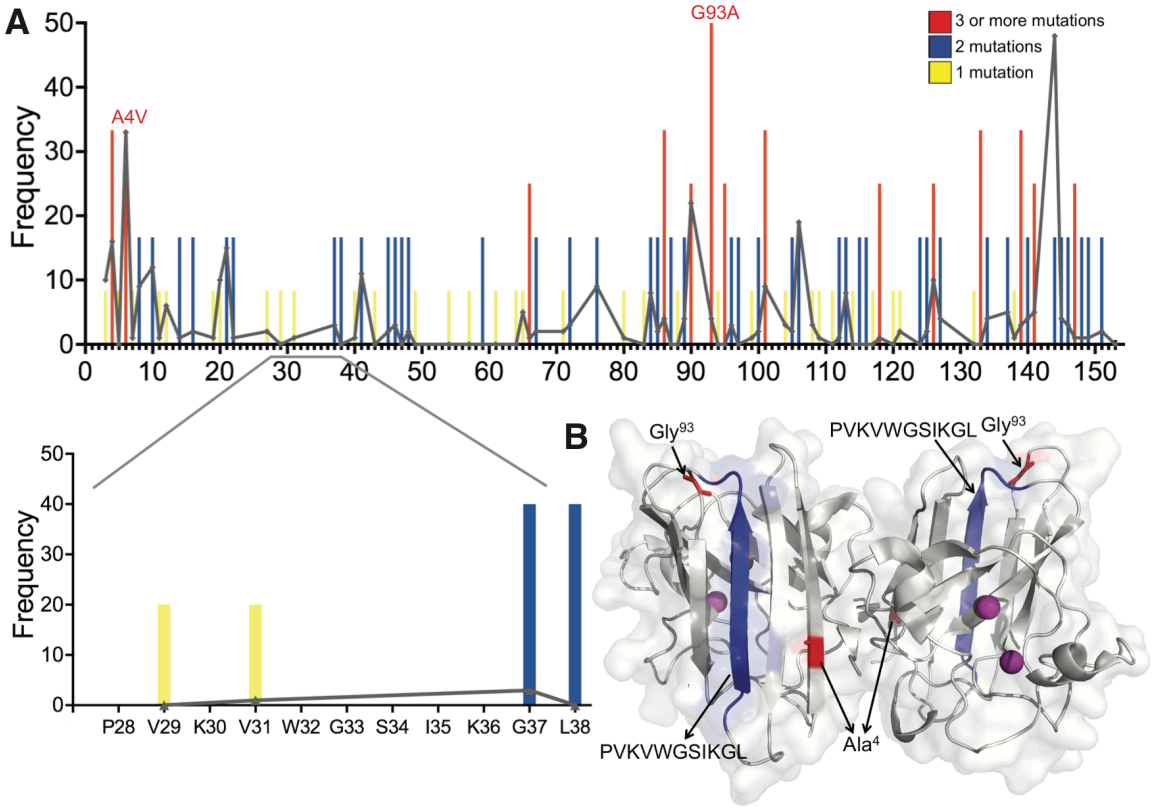

Fig. S3. Frequency distribution of ALS-related mutations in SOD1. (**A**) Histogram representation of the number of familial-disease mutations found at each residue position. Gray connected line refers to the total number of patients known to carry mutations at that residue. The segment 28-38 is expanded. Val29 and Val31 each have one known familial mutation and Gly37 and Leu38 have two known familial mutations. The segment from W32-K36 is currently the longest segment known to be unmutated in ALS patients. Notice that the segment 28-38 has low frequency of individuals with ALS linked mutations. A total of 4 individuals are known to carry mutations in this region. Data were obtained from http://alsod.iop.kcl.ac.uk (**B**) Ribbon diagram of dimeric SOD1 (PDB ID:

2C9S) with the segment 28-38 highlighted in blue. Zinc and copper atoms are shown as magenta spheres, and the familial mutation residues, A4V and G93A are colored red.

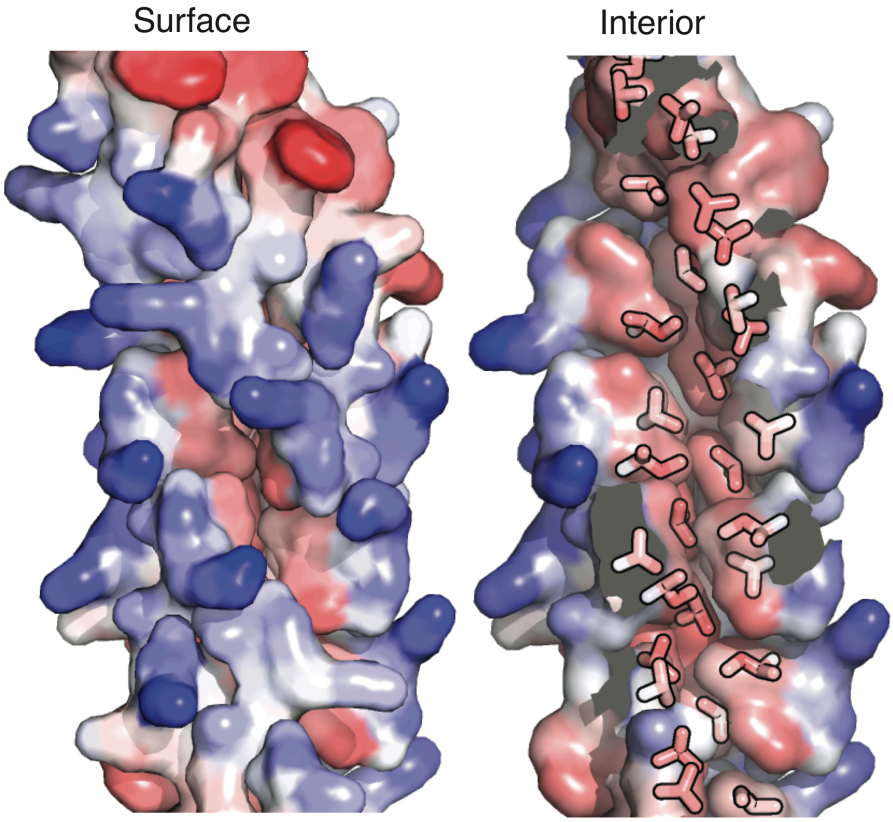

Fig. S4. Surface map of the corkscrew crystal structure showing hydrophobic surface (in red) on the surface (left) and in the inner pocket (right) made up of valine, leucine, and isoleucine side chains.

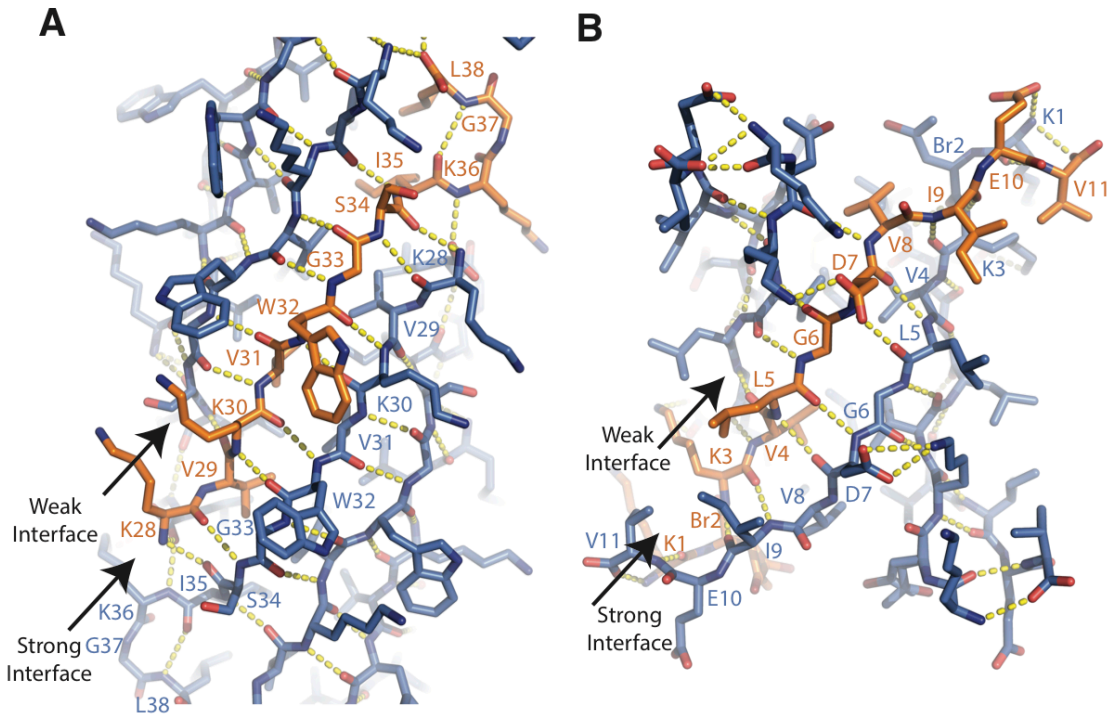

Fig S5. Hydrogen bonding network of corkscrew is composed of alternate weak and strong interfaces similar to the cylindrin structure. (**A**) Hydrogen bonding network of the corkscrew structure. Shown here the orange β strand has a strong interface with the β strand below composed of 9 hydrogen bonds and a weak interface with the β strand above composed of 7 hydrogen bonds. (**B**) Hydrogen bonding network in the cylindrin structure (PDB ID: 3SGO) shares a similar architecture where the orange strand has a stronger interface with the β strand below composed of 12 hydrogen bonds and a weak interface with the β strand above composed of 8 hydrogen bonds. Br2 referes to the non-natural amino acid 2-bromoallyl-glycine that was used for phasing.

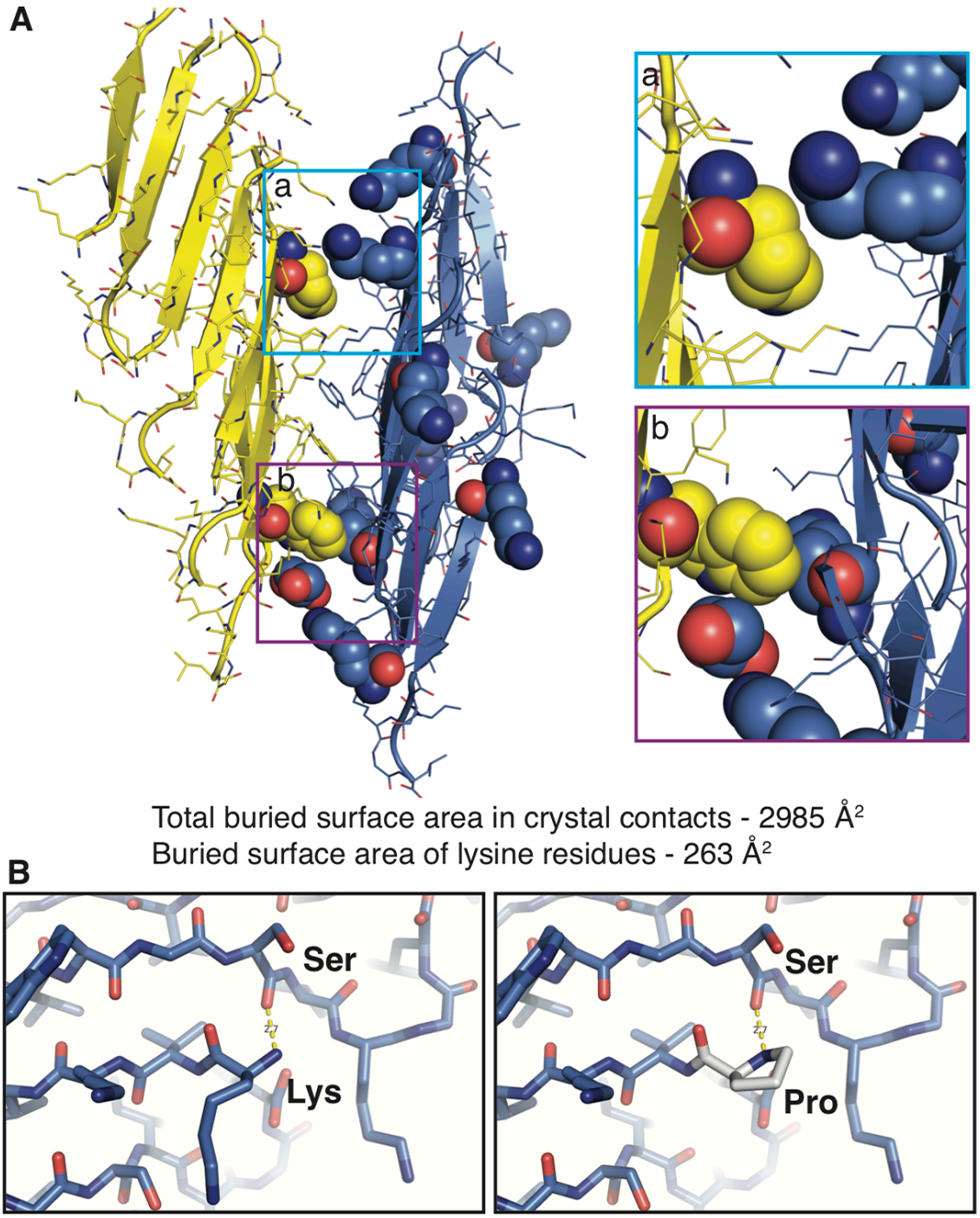

Fig. S6. Mutation of lysine at position 28 contributes weakly to the crystal packing and not to the stability of the corkscrew structure (**A**) Crystal packing of the corkscrew structure. Two asymmetric units forming crystal contacts are shown in blue

and yellow from neighboring corkscrews and N-terminal lysines are shown in sphere representation. Among the eight N-terminal lysines in each asymmetric unit, 5 form weak van der Waals interactions with (**a**) lysine residue and (**b**) tryptophan residue of the neighboring corkscrew. These interactions contribute weakly (~9%) of the total buried surface area in the crystal contacts. Buried surface area in the crystal contacts was calculated by AREAIMOL. (**B**) Lysine at position 28 is not essential for corkscrew formation and replacing it with the native proline residue does not disrupt the potential for hydrogen bonding. The N-terminal lysine forms a hydrogen bond with the serine of adjacent beta strand (Left). A PyMOL generated figure (right) shows that mutating the N-terminal lysine to the native proline residue (gray) maintains the hydrogen bond.

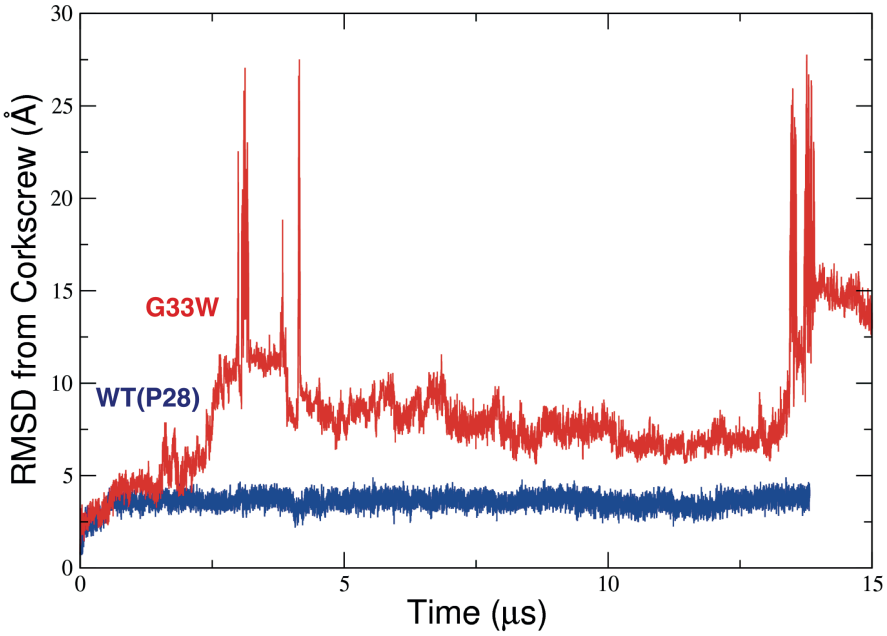

Fig. S7. All-atom MD simulations of the corkscrew structure suggest that the G33W mutant structure is less stable than the wild-type glycine 33 structure in the context of the unmodified 28-38 segment, where residue 28 is a proline (PVKVWGSIKGL). The blue and red curves correspond to Cα root-mean-square deviations (RMSD) from the corkscrew crystal structure in MD simulations of the 8-chain wild-type (PVKVWGSIKGL) and G33W mutant (PVKVWWSIKGL) corkscrews, respectively. The G33W mutant deviates from the corkscrew structure, whereas the wild-type structure remains stable throughout the length of the simulation. The simulations suggest that the dynamics of the backbone at residue 33 may contribute to the instability of the G33W mutant. The G33 residue in the corkscrew structure occupies a region of Ramachandran space different from the allowable region for tryptophan and other non-glycine amino acids. In the wild-type simulations, the backbone dihedral angles of G33 tend to remain

in the lower right quadrant of a Ramachandran plot, whereas those of W33 in the mutant quickly relax to the beta-sheet/alpha-helix regions, leading to deviations from the corkscrew structure. The extra hydrophobicity of G33W may also have an effect, making the mutant corkscrew more likely to collapse.

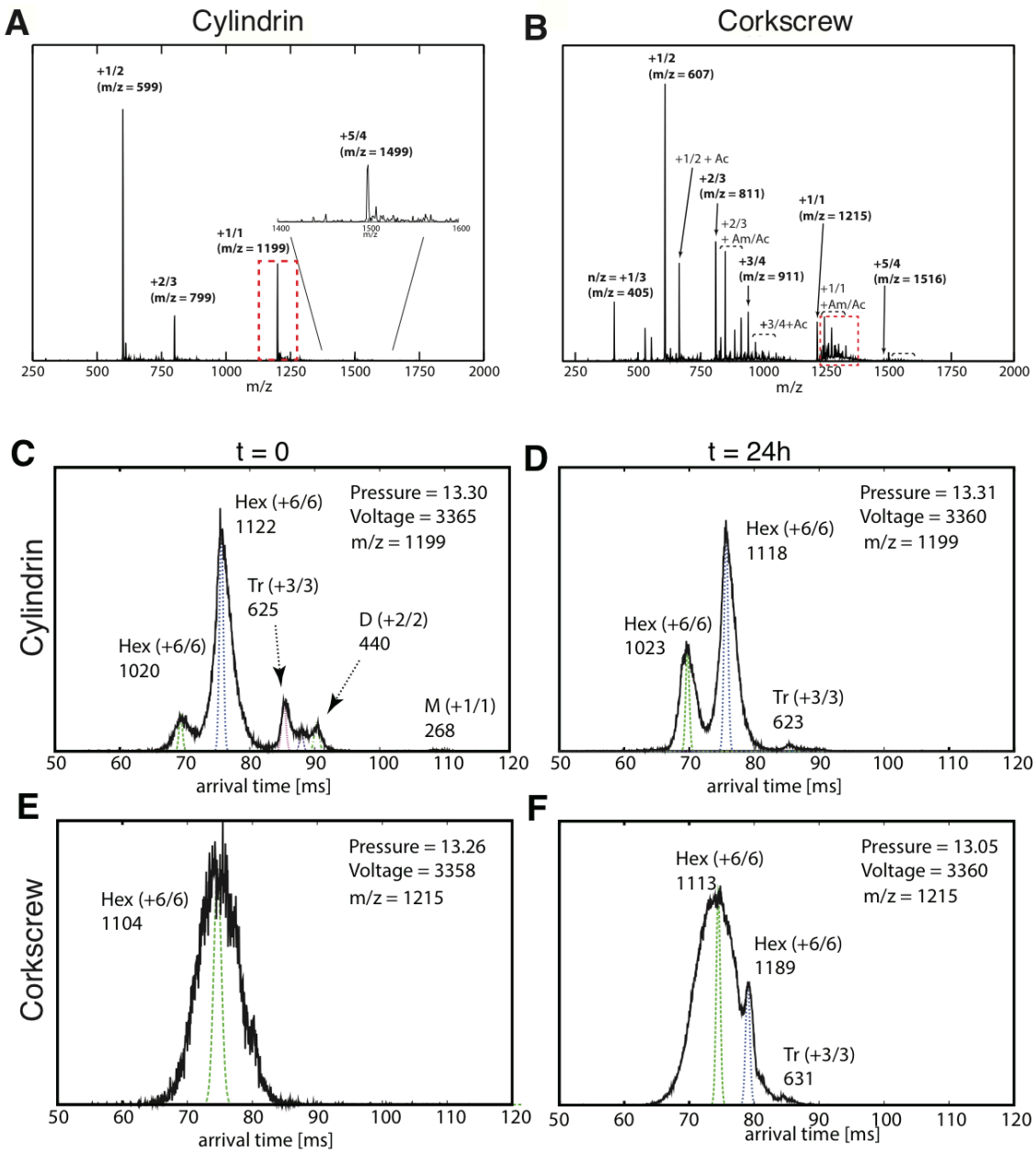

Fig. S8. The corkscrew-forming segment, SOD1(28-38) forms oligomers in solution with cross section similar to the crystal structure. (**A, B**) n-ESI-q mass spectrum of 200 μM cylindrin and SOD1(28-38) peptides in 20 mM ammonium acetate buffer (pH = 7.0), respectively. Each mass spectral peak is annotated with *n/z* where *n* is the oligomer number and *z* is the charge. (**C-F**) Representative ATDs of *n/z* = 1/1 peaks of the cylindrin and SOD1(28-38) peptides incubated for t = 0 and 24 hours. Each ATD feature

is annotated with *n/z* and an experimental collision cross section (M = monomer, D = dimer, Tr = trimer, Hex = hexamer). The narrow dashed lines are the peak shapes predicted for a single conformer of the cross sections given.

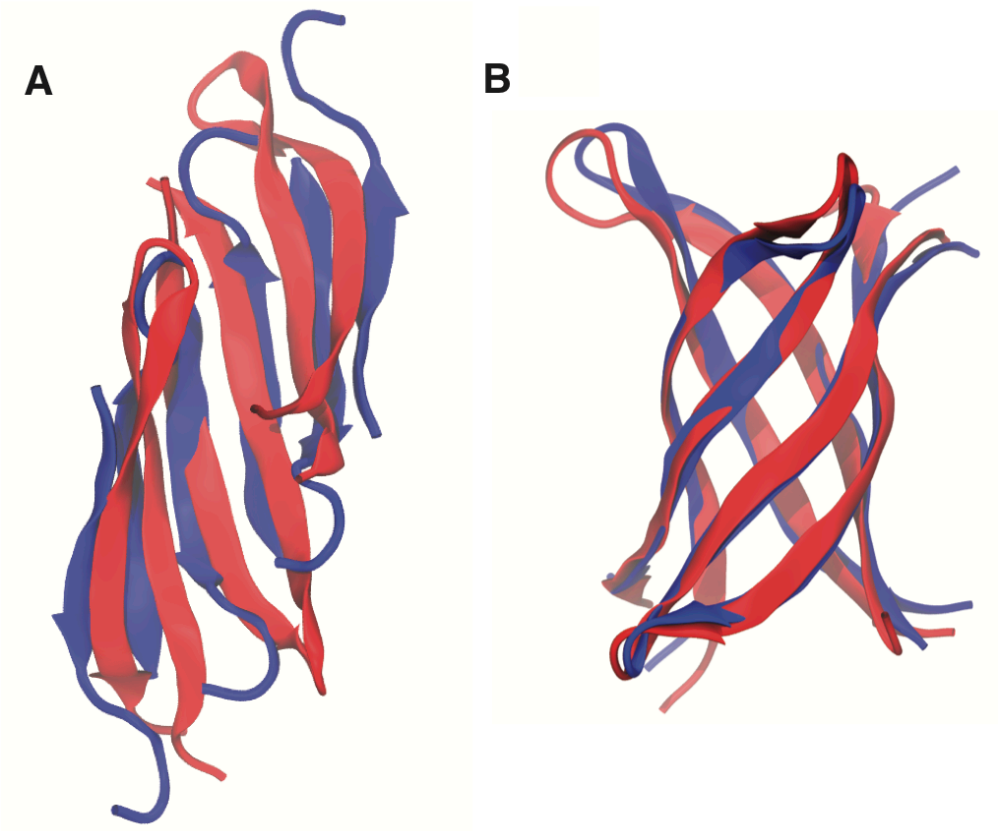

Fig. S9. MD simulations indicate that the SOD1 segment (28-38) preferentially assembles into a corkscrew-like structure. (**A**) Weakly restrained monomers of SOD1 spontaneously assembled into a corkscrew-like structure in MD simulation. A snapshot of an assembled corkscrew-like structure from an MD simulation (red) is overlaid onto the crystal structure (blue). Out of 20 simulations, three successfully assembled to a corkscrew-like structure. Interestingly, in trajectories where a corkscrew did not form, individual monomers often formed interfaces comprised of out-of-register β sheets. (**B**) As a control, we found that monomers of αB crystallin spontaneously assembled into a cylindrin structure using the same simulation protocol. A snapshot of an assembled cylindrin from the MD simulation (red) is overlaid onto the crystal structure (blue,

PDB ID 3SGR). Out of 10 simulations, one successful assembly to cylindrin was obtained. As in the SOD1 assembly runs, in αB crystallin assembly trajectories where a cylindrin did not form we often observed dimers comprised of out-of-register β sheet interfaces. See methods for additional simulation details.

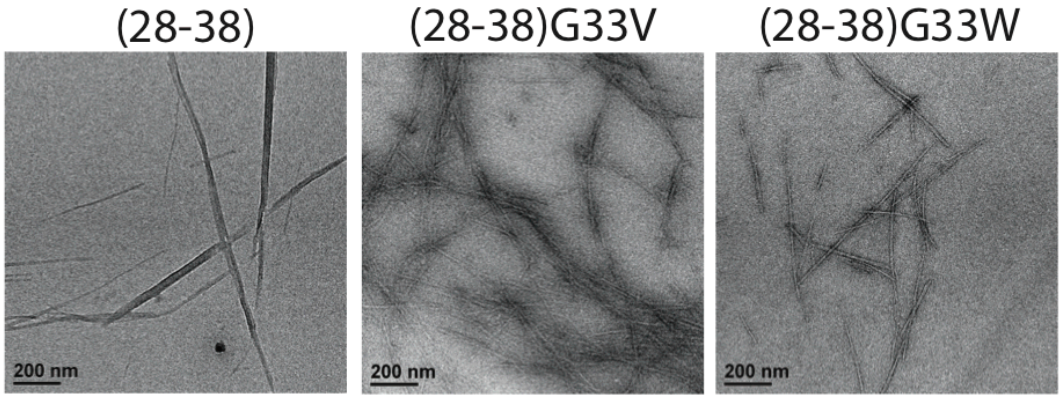

Fig. S10. Electron microscopic characterization of the peptide samples assayed for cytotoxicity. All segments showed some short fibrils when aggregated at 1 mM in 50mM tris-base buffer for 12 hours with agitation. Although SOD1 segment (28-38) is cytotoxic but (28-38)G33V and (28-38)G33W are not, micrographs show no difference in fibril propensity.

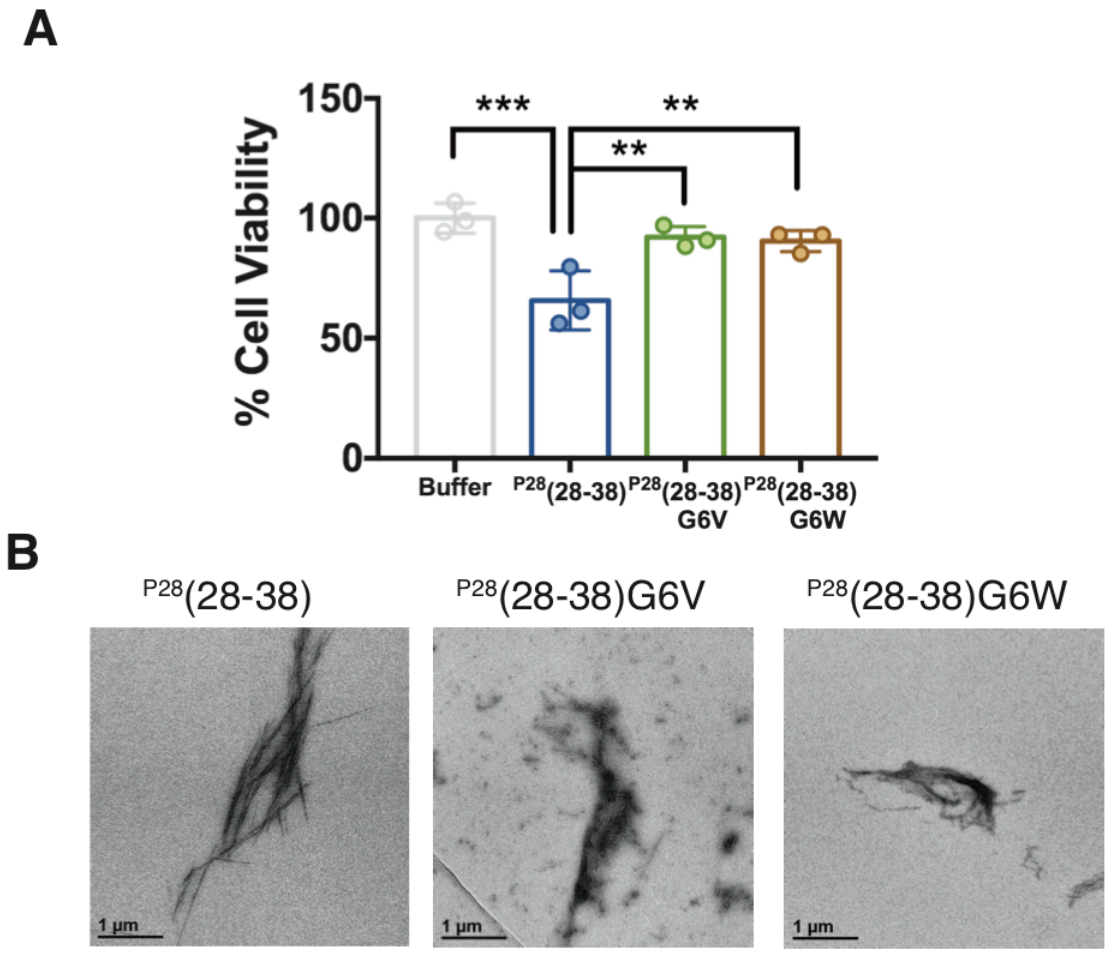

Fig. S11. Segment (28-38) with native proline is toxic and substitution at Gly33 renders it non-toxic. (**A**) Peptides were prepared identically by solubilizing in 50 mM tris-base buffer and overnight incubation at 37 °C with agitation and ES-derived motor neurons were treated with 100 µM final concentration. ^{P28}(28-38) is toxic while the peptides with substitutions G33V and G33W are non-toxic. Symbols represent individual measurements and bars represent average values. Statistical significance was measured by one-way ANOVA. (*$p < 0.05$, **$p < 0.01$)

(**B**) Electron micrographs of all three peptides showed similar sparse fibrils and thus substitution at Gly33 does not change the fibrillation propensity.

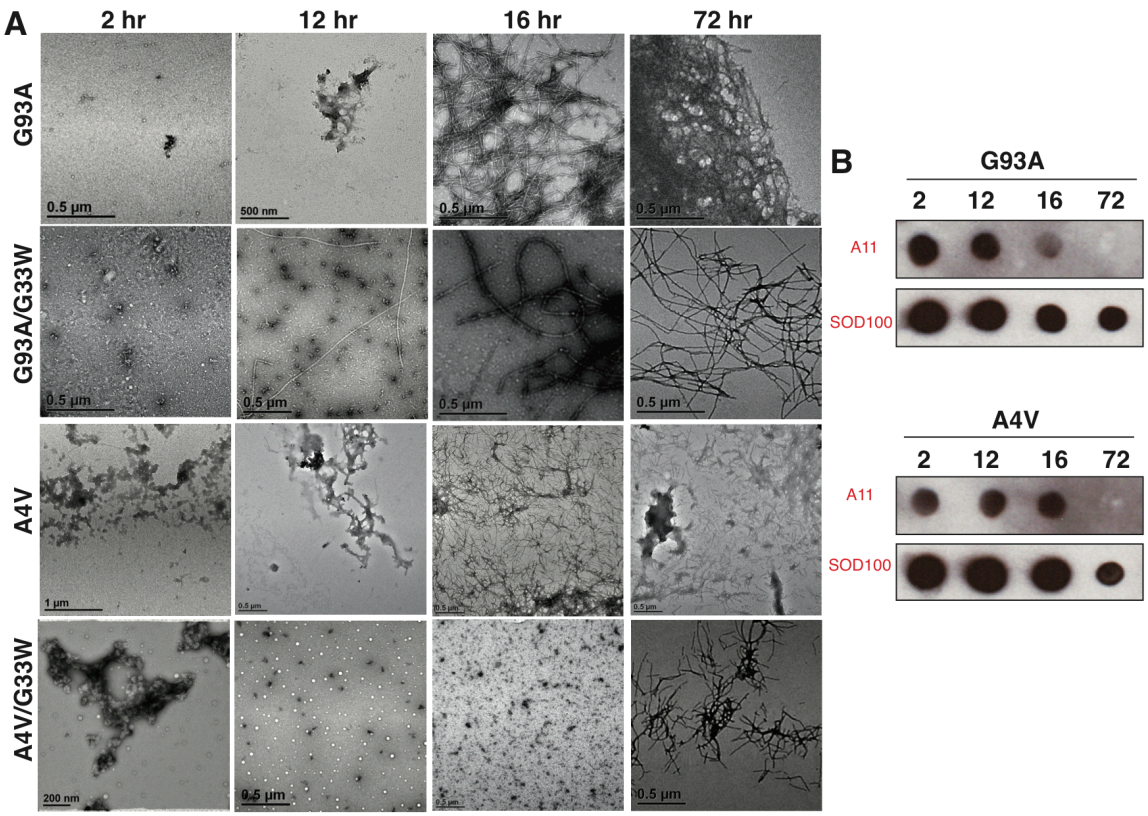

Fig. S12. (**A**) Representative electron micrographs of various preparations of the familial mutants A4V and G93A and the double mutants A4V/G33W and G93A/G33W. Some large aggregates can be seen at 2-16 hr time points but no fibrils whereas at 72 hours all constructs show large fibril loads. (**B**) Dot blots of the familial mutants aggregated for different time points. Samples aggregated for 12-16 hours are A11 positive and both proteins when aggregated for 72 hours lose A11 reactivity. SOD100 was used as loading control.

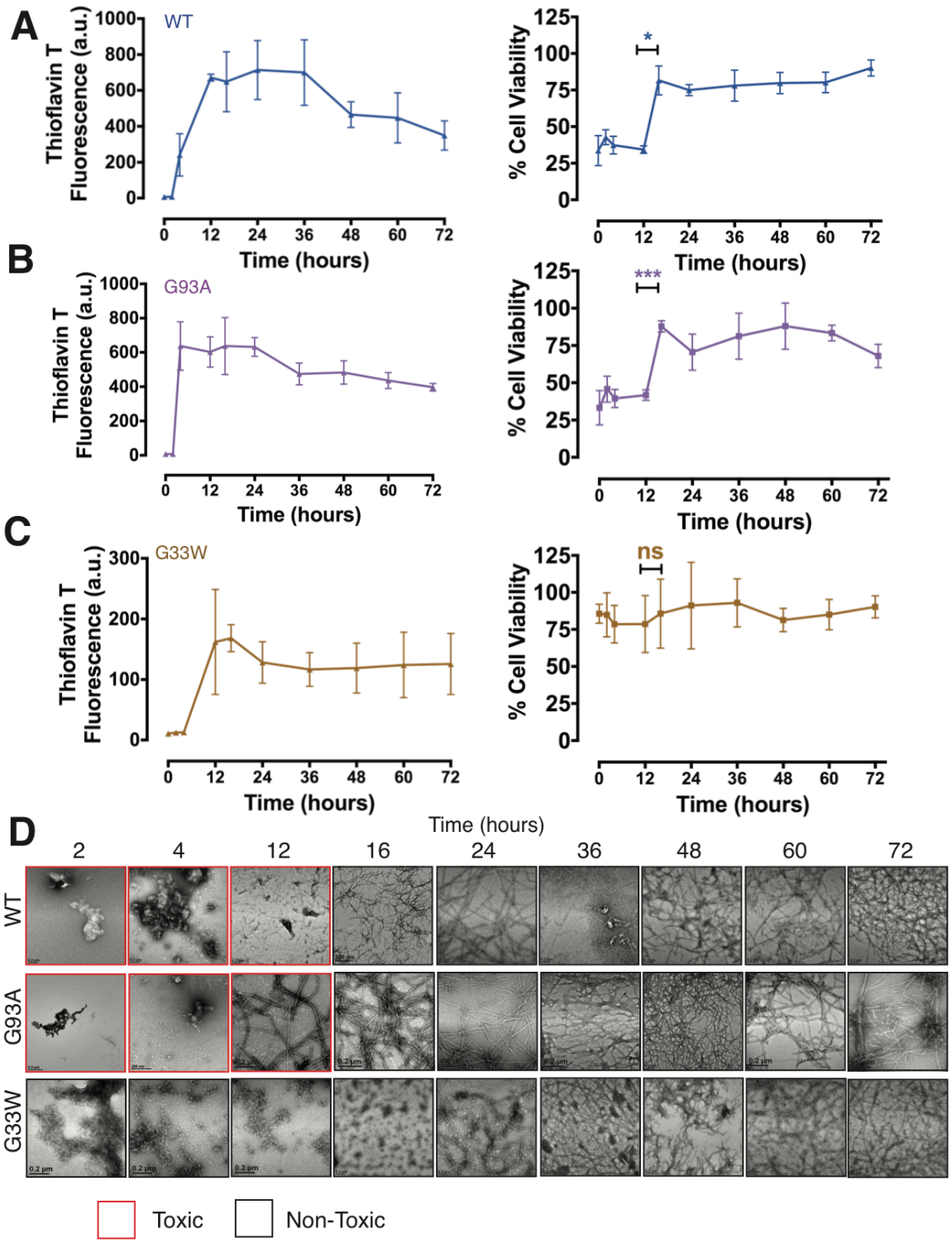
A
WT
Thioflavin T Fluorescence (a.u.)
1000
800
600
400
200
0
0 12 24 36 48 60 72
Time (hours)
% Cell Viability
125
100
75
50
25
0
*
0 12 24 36 48 60 72
Time (hours)
B
G93A
Thioflavin T Fluorescence (a.u.)
1000
800
600
400
200
0
0 12 24 36 48 60 72
Time (hours)
% Cell Viability
125
100
75
50
25
0
***
0 12 24 36 48 60 72
Time (hours)
C
G33W
Thioflavin T Fluorescence (a.u.)
300
200
100
0
0 12 24 36 48 60 72
Time (hours)
% Cell Viability
125
100
75
50
25
0
ns
0 12 24 36 48 60 72
Time (hours)
D
Time (hours)
2 4 12 16 24 36 48 60 72
WT
G93A
G33W
Toxic
Non-Toxic

Fig. S13. WT and mutant SOD1 show similar kinetics of aggregation and cytotoxicity. (**A**) Thioflavin T assay of 80 μM WT protein shows a lag time of 2-4 hours before fibrils first appear (left). Cell viability (right) of ES-derived primary motor neurons incubated with protein aggregated for indicated times shows WT is only toxic when shaken up to 12 hours, when abundant fibrils first appear. (**B**) Similar to WT, the mutant G93A shows a lag time of 2-4 hours in a thioflavin T assay (left). Cell viability (right) of ES-derived primary motor neurons incubated with protein aggregated for indicated times shows G93A is also toxic when shaken up to 12 hours, when abundant fibrils first appear. (**C**) Thioflavin T assay (left) shows G33W, the corkscrew-disrupted mutant protein behaves similar to WT and G93A with a lag phase of 2-4 hours. However, it is non-toxic at all time points (right). Results shown as Mean+SD (n=3). Statistical significance was analyzed using a two-tailed T-test with Welch's correction (*$P < 0.05$, ***$P < 0.001$, ns not significant). (**D**) Electron micrographs of SOD1 constructs aggregated for different lengths of time. Samples aggregated up to 12 hours tend to show no fibrils while samples aggregated for 16 hours or more show a large fibril load. Scale bar 200 nm.

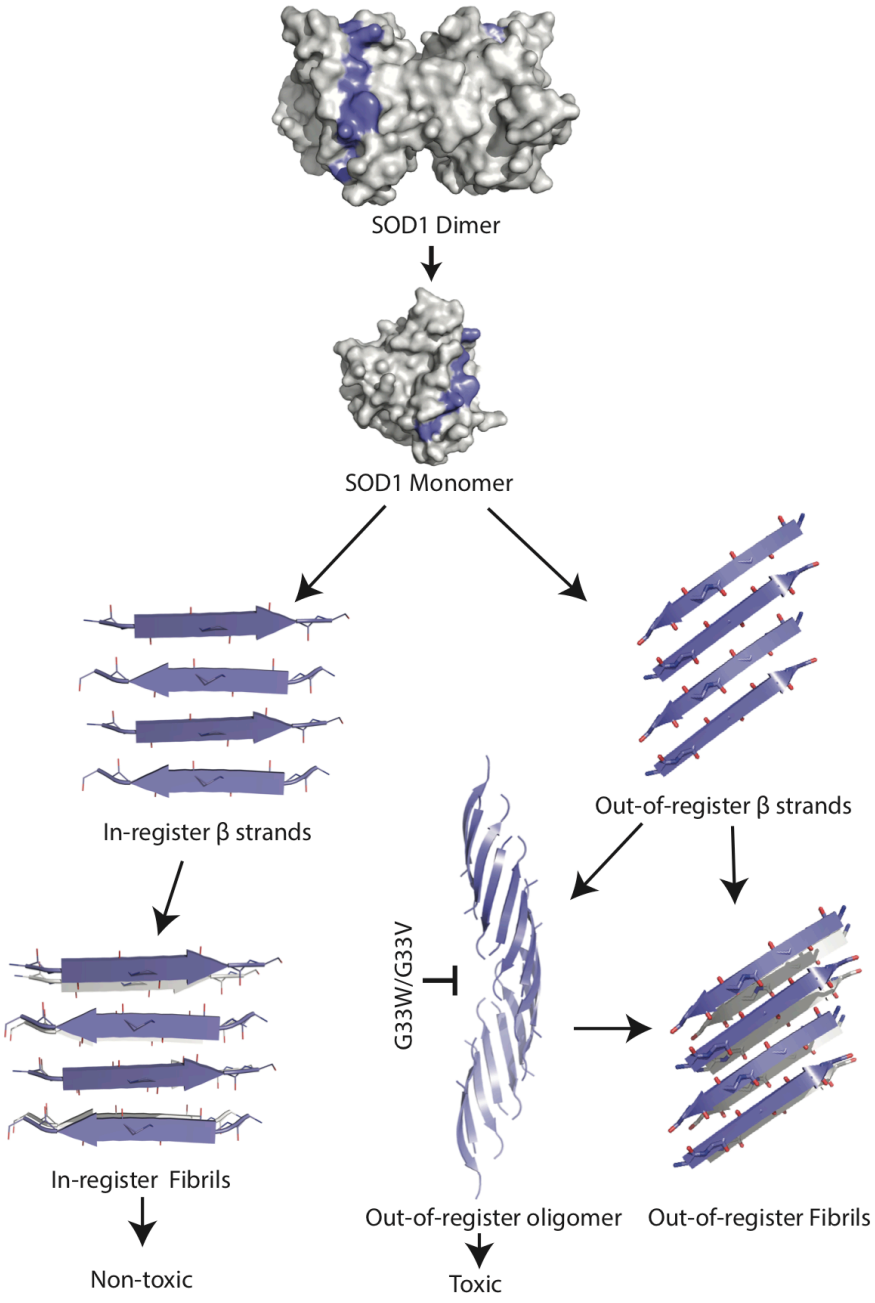

Fig. S14. SOD1 aggregation pathway. SOD1 forms a stable dimer that is resistant to aggregation. Its destabilization into monomers renders it prone to aggregation into in-register β-sheet rich fibrils. The corkscrew structure determined here, suggests that there is an off-pathway for oligomer formation independent of the in-register fibrils. The

mutations G33W and G33V specifically prevent corkscrew formation, an out-of-register oligomer. Fibril formation and cytotoxicity assays suggest that G33W and G33V do not affect the in-register fibril formation pathway and large fibrils are non-toxic.

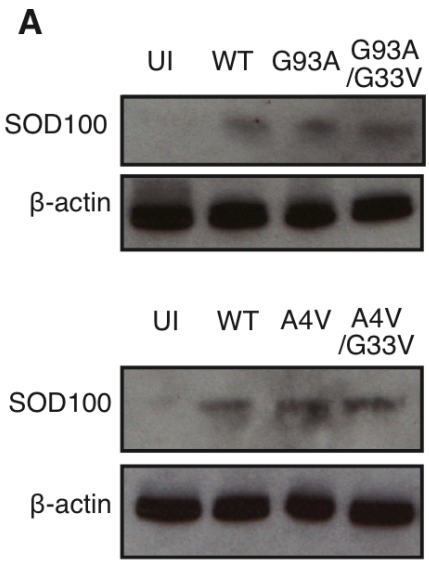

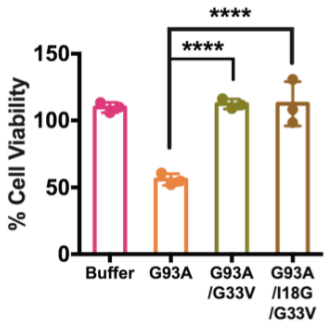

C

	% Deformed
WT	2.33
G93A	10.34
G93A/G33V	2.88

	% Deformed
WT	0
A4V	30
A4V/G33V	3.125

D

	Axon Length (n)	Mitochondria (n)	
		Size (a.u.)	Number
WT	1± .01 (365)	14.08	58 (365)
A4V	0.92 ± .01 (515)	30.17	32 (468)
A4V/G33V	0.95 ± .01 (575)	10.57	54 (400)

	Axon Length (n)	Mitochondria (n)	
		Size (a.u.)	Number
WT	1 ± .01 (360)	10.78	78 (171)
G93A	0.95 ± .01 (390)	14.68	39 (374)
G93A/G33V	1.03 ± .01 (375)	11.68	59 (361)

Fig. S15. Expression of A4V and G93A mutant proteins causes axon shortening and mitochondrial clustering in zebrafish model. (A) Western blotting on zebrafish embryos to confirm expression of the mRNA injected. SOD100 was used to detect SOD1 and β-actin was used as loading control. UI refers to uninjected zebrafish. (**B**) Construct G93A/G33V/I18G is non-toxic to ES derived motor neurons similar to the G93A/G33V mutant. Results shown as Mean ± SD. Bars show average values and symbols represent individual measurements. Statistical significance was analyzed by one-way ANOVA (**C**)

Zebrafish at 2dpf were imaged and higher percentage of A4V (30%) and G93A (10%) injected zebrafish displayed significant deformation compared to WT and the G33V expressing fish. (**D**) Average axon length (normalized to WT construct) and mitochondrial size of the different constructs. n refers to the total number of measurements made for each group.

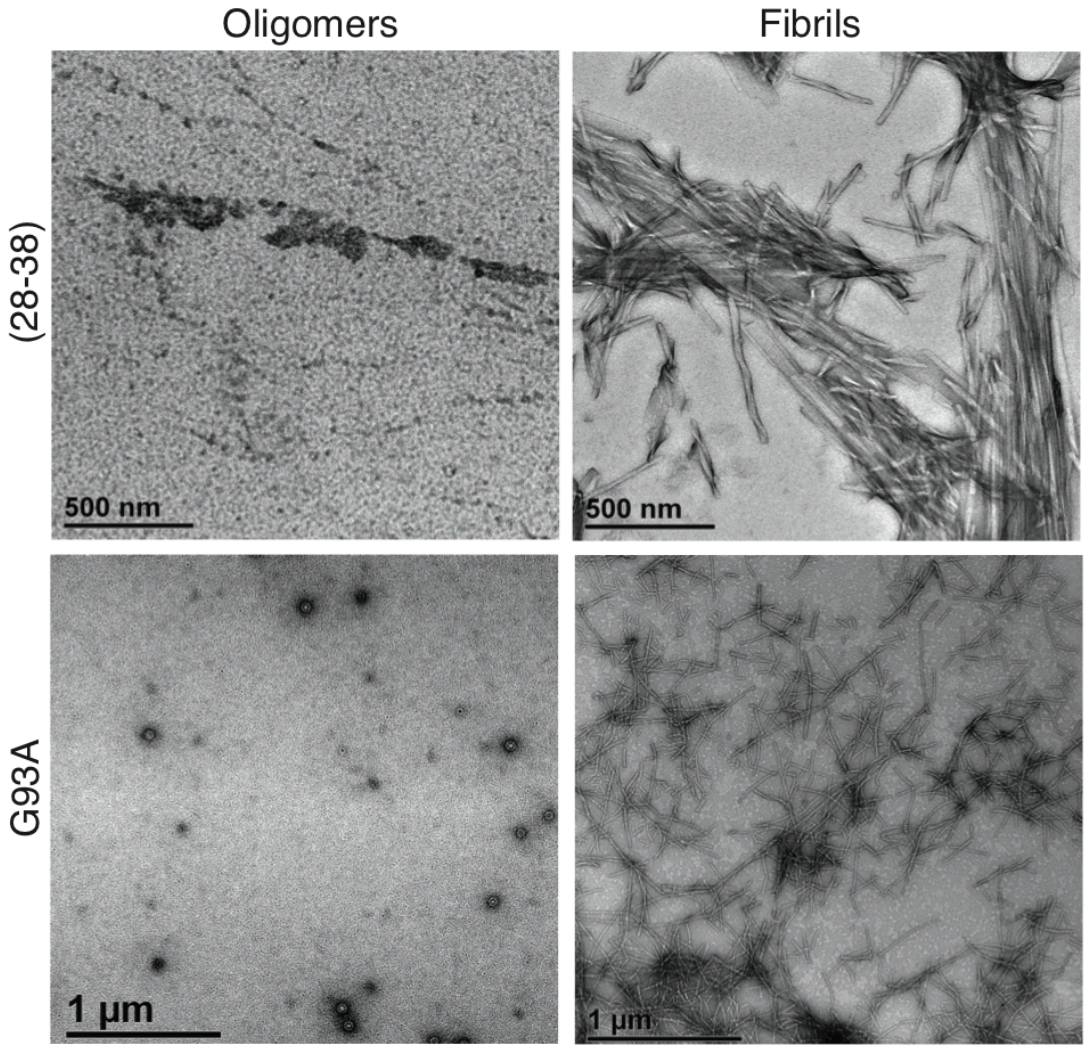

Fig. S16. Electron micrographs of samples used for CSAb binding shown in figure 4B, 4E. The corkscrew-forming segment SOD1(28-38) at 8 mM was incubated at 37°C for 12-16 hrs with and without agitation and probed for CSAb binding (Fig. 4E). The sample that showed no visible fibrils (top, left) was CSAb-positive, whereas the sample that was rich in fibrils (top, right) was CSAb-negative. Full-length apo-G93A protein at 80 µM that was aggregated for 12 hrs with agitation was CSAb positive and did not have any fibrils (bottom, left) whereas the sample aggregated for 72 hrs that had abundant fibrils (bottom, right) was CSAb negative.

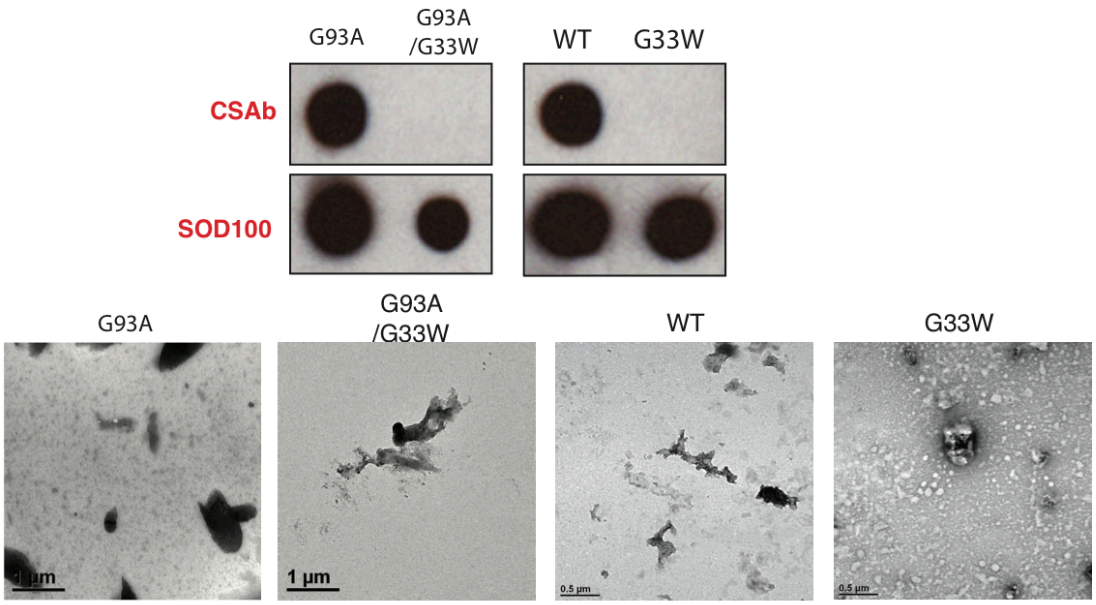

Fig. S17. CSAb does not recognize corkscrew-disrupting mutant protein. Proteins G93A, G93A/G33W, WT and G33W were aggregated for 2 hours and probed for CSAb reactivity. Both WT and G93A constructs showed aggregates by electron microscopy and were CSAb positive but G93A/G33W and G33W were not CSAb reactive. SOD100 was used to compare loading.

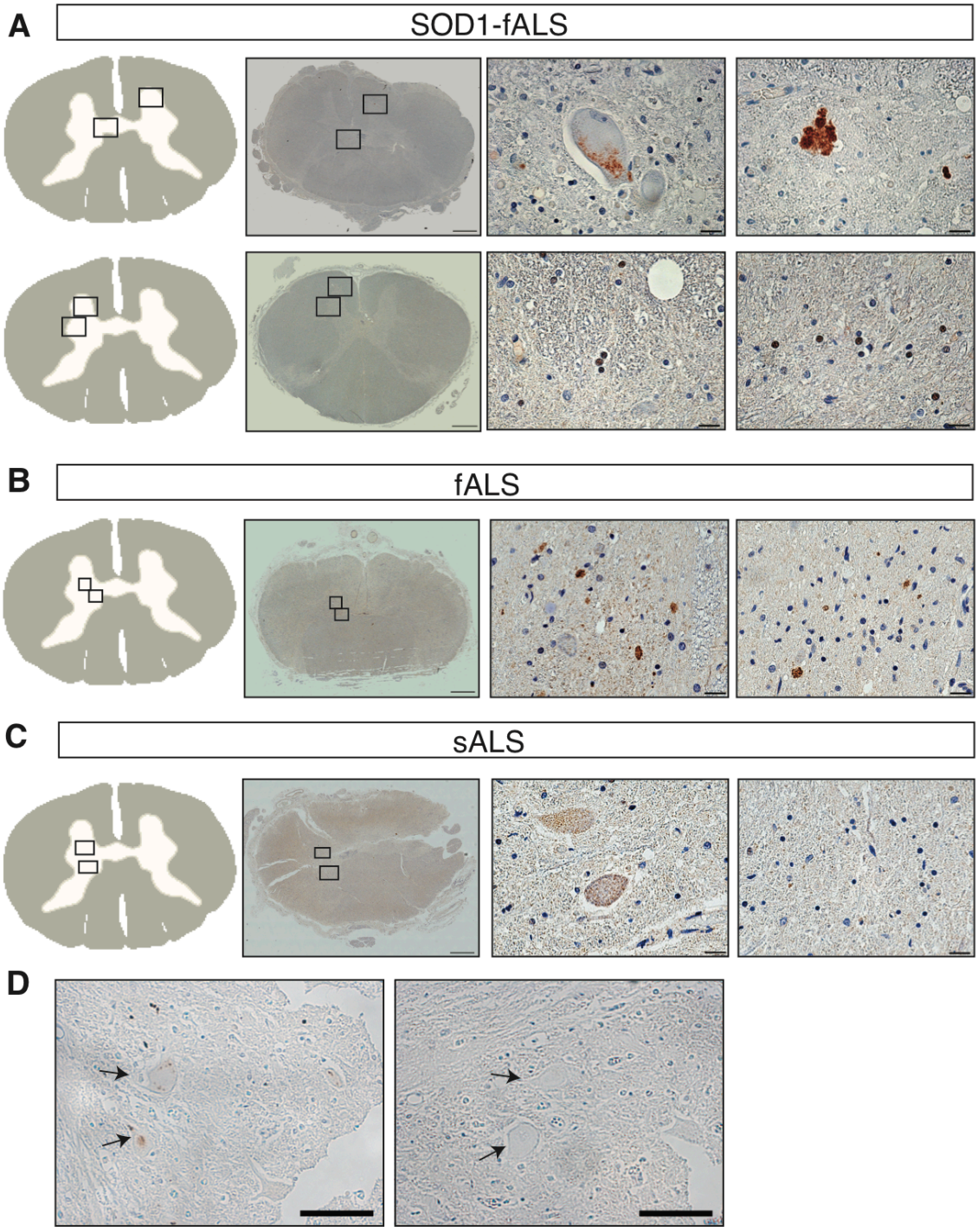

Fig. S18. CSAb reactivity in different ALS subjects. Micrographs of human ALS tissues probed for CSAb reactivity. (**A**) In 2 different SOD1-fALS patients we found

different reactivity patterns. In one subject, we found predominantly cytoplasmic reactivity in the gray matter. In another subject, we observed predominantly nuclear reactivity in non-neuronal cells in the gray matter. (**B**) In non-SOD1 linked fALS subjects we found both neuronal and non-neuronal reactivity. (**C**) In sALS subject, we observed reactivity in motor neurons but not in non-neuronal cells. (**D**) The specificity of the reactivity was measured by removing the primary antibody from the protocol. Scale bar of entire tissue sections (in **A,B,C**) 1000 μm and 20 μm of higher magnifications.

Table S1. X-Ray Data Collection and Refinement Statistics

	KVKVWGSIKGL	KVKVWGSIKGL (iodide)
Beam line	APS 24-ID-E	APS 24-ID-E
Resolution Å	1.9	2.1
Total unique reflections	8378	11489
Total reflections observed	47323	43500
Space group	$P2_12_12_1$	$P2_12_12_1$
Rsym	16.5% (48.4%)	9.5% (41.8%)
I/σ	8.4 (4.3)	11.1 (3.6)
Completeness	95.5 %	96.7%
Wavelength (Å)	0.9791	0.9791
Unit cell dimensions **a b c (Å)** **α β γ (°)**	 33.20 44.44 71.23 90.0 90.0 90.0	 33.09 44.39 71.43 90.0 90.0 90.0
Refinement		
Resolution (Å)	2-35.49	2.1- 19.3
Reflections for refinement (after merging Friedel Pairs)	6690	6249
Rfree/Rwork (%)	25.08/21.09	26.2/21.2
Molecules in the Asymmetric unit	8	8
Solvent content (%)	54.6	54.6
Matthews coefficient	2.71	2.71
Total water molecules	34	52
Total iodide atoms	0	2
Glycerol molecule	0	1
Rmsd bond length (Å)	0.010	0.010
Rmsd angles (°)	1.022	0.88
Ramachandran plot **Allowed** **Generous** **Disallowed**	 100 0 0	 100 0 0

Table S2. Comparison of buried surface area (BSA) and shape complementarity (Sc) of corkscrew with cylindrin and steric zippers.

	Corkscrew	Cylindrin*	Steric Zipper**
Sc	0.79	0.74	0.68
BSA	984	943	1034
BSA/Residue	89	86	94

* PDB ID: 3SGO

** PDB ID: 4RIL

BSA values were calculated using AREAIMOL. The area buried was calculated by subtracting the solvent accessible surface area of one chain of the assembly from the total solvent accessible surface area of an isolated chain.

Shape complementarity was calculated for one chain of the assembly. The interface characterized in the shape complementarity calculation is between one chain and the remaining chains of the assembly.

Table S3. Comparison of oligomers formed by cylindrin and corkscrew by ion mobility mass spectrometry. Cross sections of different oligomers formed by cylindrin and corkscrew segments are given.

Oligomer (n)	Cylindrin (MW=1199)	SOD1(28-38) (MW=1215)
1	268(+1); 262, 273(+2)	273, 288(+2), 290, 306 (+3)
2	440(+2), 442, 452 (+3)	443, 456 (+3)
3	625 (+3)	631 (+3), 639 (+4)
6	1023 (+6), 1118 (+6)	1113 (+6), 1189 (+6), 1222 (+8)

Table S4. Clinical information of samples used for CSAb reactivity.

(NK – not known, NA – not applicable)

	Clinical Diagnosis	CSAb (Non-neuronal)	CSAb (Neuronal)	Pathologic diagnosis	Braak NFT stage	Thal amyloid phase	TDP-43	FHx	Age	Sex	Race
1	ALS	0.09	1	ALS	0	0	Yes	No	46	M	Caucasian
2	ALS	0.08	0	ALS	0	0	Yes	No	59	F	Caucasian
3	ALS	0.10	0.2	ALS	0	0	Yes	No	48	M	Caucasian
4	ALS	0.046	0.94	ALS	I	0	Yes	No	58	F	Caucasian
5	ALS	0.06	1	ALS	I	0	Yes	No	56	F	Caucasian
6	ALS	0.05	0	ALS	NK	NK	NK	NK	36	M	Not specified
7	Control	0.04	0.07	Control	0	0	NA	No	57	M	Caucasian
8	Control	0.09	0.50	Control	0	0	No	No	67	M	Caucasian
9	Control	0.09	0.27	Control	III	0	NA	No	71	F	Caucasian
10	Control	0.04	0	Control	III	1	NA	No	72	M	Caucasian
11	Control	0	0	Control	NK	NK	NA	NA	62	F	Caucasian
12	Control	0	0	Control	NK	NK	NA	NA	69	F	Not specified
13	Control	0	0	Control	NK	NK	NA	NA	72	M	Not Specified
14	Control	0.07	0.13	Control	NK	NK	NA	NA	57	M	Not Specified
15	Control	0.10	0.20	Control	0	0	NA	NA	92	F	Not Specified
16	Control	0.02	0	Control	0	0	NA	NA	80	M	Not Specified
17	ALS	0.20	0.46	ALS, familial (SOD1 A4V)	I	0	No	Yes	55	F	Caucasian
18	ALS	0.11	0.93	ALS, familial (SOD1 G141X)	0	0	No	Yes	42	F	Caucasian
19	ALS	0.14	0.87	ALS, familial (SOD1)	0	0	No	Yes	55	M	Caucasian
20	ALS	0.01	1	ALS, familial (SOD1 A4V)	NK	NK	NK	NK	68	M	Not specified
21	ALS	0	0.06	ALS, familial (SOD1 A4V)	NK	NK	NK	NK	65	F	Not specified
22	ALS	0.10	0.87	ALS, familial (SOD1 A4V)	NK	NK	NK	NK	21	F	Not specified
23	ALS	0.05	0.83	ALS, familial (Chr9)	I	0	Yes	Yes	58	M	Caucasian
24	ALS	0.21	0.74	ALS, familial (Chr9)	I	0	Yes	No	51	F	Caucasian
25	ALS	0.26	0.94	ALS, familial (Chr9)	I	0	Yes	No	49	F	Caucasian
26	ALS-MCI	0.09	0	ALS, familial (Chr9)	I	0	Yes	No	53	M	Caucasian

27	ALS	0.12	1	ALS, familial (Chr9)	II	0	Yes	Yes	58	F	Caucasian

Chapter 3: Atomic structures of oligomeric segments of SOD1 suggest molecular differences between toxic and non-toxic amyloid oligomers

Abstract: The aggregation cascade of disease-related amyloidogenic proteins involves multiple intermediate states and ultimately results in insoluble amyloid fibrils. The molecular details and biochemical properties of these intermediates have been largely unknown. Here, we report crystal structures of variants of a cytotoxic oligomer-forming segment 28-38 of the ALS-linked protein, SOD1. The crystal structures reveal three different architectures: corkscrew oligomeric structure, non-twisting curved sheet structure and a steric zipper proto-filament structure. Cytotoxicity assays suggest that corkscrew oligomeric assembly is cytotoxic and other structures are relatively benign. Our works highlights the polymorphism associated with the segment 28-38 of SOD1 and identifies the molecular features of toxic and non-toxic entities.

Title: Atomic structures of oligomeric segments of SOD1 suggest molecular differences between toxic and non-toxic amyloid oligomers

Authors: Smriti Sangwan[1], Michael R. Sawaya[1], Kevin Murray[1], Michael P. Hughes[1] and David S. Eisenberg[1]

Affiliations: [1]Howard Hughes Medical Institute, UCLA-DOE and Molecular Biology Institutes, Department of Biological Chemistry Los Angeles, California, USA.

Corresponding Author: David S. Eisenberg, email: david@mbi.ucla.edu

Abstract: The aggregation cascade of disease-related amyloidogenic proteins involves multiple intermediate states and ultimately results in insoluble amyloid fibrils. The molecular details and biochemical properties of these intermediates have been largely unknown. Here, we report crystal structures of variants of a cytotoxic oligomer-forming segment 28-38 of the ALS-linked protein, SOD1. The crystal structures reveal three different architectures: corkscrew oligomeric structure, non-twisting curved sheet structure and a steric zipper proto-filament structure. Cytotoxicity assays suggest that corkscrew oligomeric assembly is cytotoxic and other structures are relatively benign. Our works highlights the polymorphism associated with the segment 28-38 of SOD1 and identifies the molecular features of toxic and non-toxic entities.

Introduction:

Amyloid aggregation is implicated in a number of neurodegenerative and systemic diseases. Among the variety of protein aggregates known to exist, fibrillar species are the most readily recognized, having characteristic amyloid-like properties including the cross-β X-ray diffraction pattern, binding to specific dyes and birefringence upon binding to Congo Red (1). The cross-β diffraction pattern suggests that amyloid fibrils are composed of packed β-sheets. Indeed the crystal structures of amyloid-forming short peptides have revealed a β-sheet architecture termed steric zipper (2, 3). Their structural and thermodynamic stability suggests that amyloid fibers represent the energetic end state of the aggregation pathway.

Aggregated species that evolve prior to fiber deposition are largely uncharacterized. The aggregation cascade of proteins is thought to evolve slowly on a time scale of decades and potentially has multiple intermediate states. A detailed investigation of these intermediates has been challenging, as these states are transient and difficult to isolate. Further, multiple segments in any protein may act synergistically or independently to form different intermediate structures. Thus, the identification of these intermediate states and detailed characterization of their cytotoxic roles has been limited.

Studies over the last two decades have suggested that small oligomers that form transiently in the aggregation pathway exacerbate disease progression by exerting toxicity in neuronal cells (4, 5). The failure of fiber-inhibiting therapeutics in clinical trials and the low cytotoxicity of amyloid fibers in various model systems suggest that small

oligomers may be the toxic intermediate state in amyloid diseases. It is accepted that amyloid oligomers are β-sheet rich, cytotoxic and bind conformational antibodies such as A11. Structural studies have revealed anti-parallel, β-sheet rich oligomeric structures of proteins such as amyloid-β, α-B crystallin and SOD1 (6, 7). Although it is appreciated that the aggregation of these proteins has multiple intermediates, the molecular details and biochemical properties of these intermediates are largely unknown.

ALS is a fatal neurodegenerative disease caused by degeneration of motor neurons that results in loss of muscle control and paralysis. SOD1, a ubiquitously expressing cytosolic protein is found in insoluble aggregates in a subset of familial ALS patients. An exceptionally stable protein, the aggregation of SOD1 has been attributed to structural perturbations induced by the familial mutations or oxidative damage accumulated over time (8, 9). Recently we discovered that SOD1 forms cytotoxic soluble oligomers with the segment 28-38 of SOD1 as the oligomeric core. The segment is cytotoxic to cultured motor neurons and substitutions at Gly33 with bulky residues alleviate toxicity by disrupting oligomer formation. Here we report three new crystal structures of different variants of this segment that reveal possible aggregation intermediates. Biochemical characterization of these aggregation states helps differentiate the molecular features of toxic and non-toxic structures.

Results:

1. **Segment 28-38 of SOD1 has a high aggregation propensity** – One of the critical questions raised by the discovery of corkscrew (Sangwan et al.) is whether it is the only toxic conformation or if the segment forms more than one toxic intermediate state. Additionally, the presence of familial mutations in the segment led us to investigate the effect of these mutations. Notably, the segment has a low frequency of familial mutations and only three amino acid substitutions (Ala, Arg and Val) have been found so far. Among the various familial mutations found in this segment: Ala substitutes for V29 and V31 and Arg and Val substitutes for G37 and L38. We hypothesized that G37R would have a potentially large effect on the aggregation kinetics of this segment due to the change from a small amino acid to a charged amino acid (Fig. 1A, left). G37R has been previously characterized extensively and shown to increase the aggregation propensity of the full-length protein leading to rapid disease onset and progression in transgenic mice models (10). We also analyzed the fiber-forming propensity of the segment using ZipperDB (11), an algorithm that predicts the propensity of six residue segments to form amyloid fibrils (Fig. 1A, right). ZipperDB showed two aggregation-prone subsegments - 31-KVWGSI-36 and 33-GSIKGL-38. Thus, we set out to characterize the G37R mutant as well as the shorter 6-residue subsegments.

2. **Crystal structure of segment 28-38 with familial mutation G37R reveals a different corkscrew geometry** – We obtained crystals of the segment 28-38 harboring the familial mutation G37R (i.e. the tenth residue in the sequence KVKVWGSIKRL). The peptide used in crystallization trials has an additional residue change of P28K used to increase solubility of the segment. This substitution has been shown previously to contribute

minimally to the structure and cytotoxic properties. The structure was solved by molecular replacement using the native corkscrew as a search model (sequence KVKVWGSIKGL, PDB ID 5DLI). The structure reveals a twisted b-sheet with the same antiparallel, out-of-register β-strand construction as the wild type corkscrew (Fig. 1B); however G37R has more strands per turn (20 vs. 16), a shorter pitch length (59 Å vs. 71 Å) and larger diameter (38 Å vs. 25 Å). This difference is supported by Arg37, which engages in multiple inter- and intra-strand interactions. The charged side chain of Arg37 forms hydrogen bonds with the C-terminal carboxylate (Leu38) of alternate strands or of the same strand (Fig. 1C). These interactions are not possible with native Gly residue and support the shorter pitch length. The overall similarity of the mutant structure to the corkscrew suggests that the segment has a high propensity to form antiparallel, out-of-register assemblies although single point substitutions can induce subtle changes in the overall architecture.

3. **Orange G supports untwisting of the corkscrew segment 28-38 with familial mutation G37R**– In our efforts to obtain phases for the mutant segment; we crystallized a derivative with a bromo-allyl valine at position 2 (sequence KBKVWGSIKRL). We obtained crystals in the presence of orange G, a small aromatic dye previously shown to modulate amyloid formation of Alzheimer's disease-associated proteins, amyloid-β and tau (12). The crystals displayed a needle-like morphology distinctly different from the crystals of the mutant peptide KVKVWGSIKRL. The crystals diffracted to 1.8 Å and phases were obtained by molecular replacement using the corkscrew structure as a search model. The structure revealed a curved b-sheet with the same antiparallel, out-of-register

β-sheet construction as the wild type and G37R corkscrews, but surprisingly no twist (Fig. 2A).

As with both corkscrews, the curvature of the sheet is stabilized by short hydrophobic side chains (valine and isoleucine) pointing into the concave interior and charged and bulky residues pointing outward from the convex exterior; however, all twist is eliminated apparently due to orange G-mediated contacts between neighboring sheets. Stacked aromatic side chains of W32 intercalate with the aromatic rings of orange G (Fig. 2B). The aromatic rings of orange G stack against the Trp32 aromatic side chains and the sulfate moieties of orange G form salt bridges with K30 of both sheets (Fig. 2C, 2D). Together, these interactions result in a high binding energy (-12.4 kcal/mol) and favorable shape complementarity (0.82). Previously, orange G had been observed bound to a steric zipper composed of a 6-residue segment of amyloid-β. The aromatic rings of orange G stacked with similar aromatic stacking and salt bridges but in a slightly altered conformation (13).

4. **Crystal structure of the segment 30-KVWGSI-35 reveals a steric zipper –** We also obtained diffraction quality crystals of the subsegment, 30-KVWGSI-35. The 6-residue segment forms a steric zipper composed of in-register, anti-parallel β-sheets that are arranged face-to-back. It is a Class 7 zipper (3). Notably, the side chains of neighboring sheets do not pack as tightly as most pathogenic steric zippers, apparently due to the conflicting sizes and properties of the side chains in the interface (shape complementarity =0.65); a void between sheets is filled adventitiously by a trifluoroacetic acid molecule.

The side chain of W32 extends along the zipper axis and stacks against the backbone of G33 of the strand above it in the sheet (Fig. 3B) and results in staggering of the sheets relative to each other (Fig. 3C).

5. **Variant peptides show distinct diffraction patterns** – We performed fiber diffraction on the native corkscrew forming peptide (KVKVWGSIKGL, PDB ID 5DLI) as well as the familial mutant crystallized here (KVKVWGSIKRL and KBKVWGSIKRL). 28-38 and G37R mutant peptides produce a distinct diffraction ring at 4.6 Å (Fig. 4E). The absence of reflections at 10 Å indicates a β-sheet rich structure that is devoid of pairs of sheets. Interestingly, the segment forming untwisted structure (KBKVWGSIKRL) gives a distinct diffraction pattern with multiple rings notably at 4.75 Å and 9.5 Å. We also collected the diffraction patterns after fibrillization and found that the native 28-38 segment shows rings at 4.6 Å and 11.9. The segment KBKVWGSIKRL shows diffraction at 4.75 Å, 9.5 Å and 13.1 indicative of a mixture of different β-sheet structures. Together, these data suggest that the corkscrew assembly is the predominant oligomeric intermediate state.

6. **Orange G favors untwisting of the corkscrew and alleviates toxicity of the segment –** We investigated the cytotoxic properties of G37R 28-38 segment (KVKVWGSIKRL) in different aggregation states. For these experiments, we incubated the segment at 37° both under quiescent conditions to promote oligomer assembly and shaking conditions to promote fibril assembly. We then assessed the cytotoxic properties of both preparations on cultured cells. Although the segment was cytotoxic in both conditions, we observed

higher cytotoxicity in oligomer-promoting quiescent conditions (Fig. 5A). Transmission electron microscopy (TEM) verified that samples prepared under quiescent conditions contained no fibrils whereas those prepared by agitation showed fibrils (Fig. 5B). Additionally, we utilized the propensity of the curved sheet architecture to bind orange G. We hypothesized that under oligomer-forming conditions, the addition of orange G would drive the equilibrium towards the non-twisting sheet architecture and thus rescue toxicity. We incubated the mutant peptide (KVKVWGSIKRL) with orange G under oligomer-promoting conditions and assessed cytotoxicity thereafter. Given that orange G is a known modulator of fibril formation, we only added sub-stoichiometric amounts to induce subtle changes in populating corkscrew or untwisted conformations. We observed a small but significant rescue of toxicity (Fig. 5E). As a control, we used 8-hydroxypyrene 1,3,6 – trisulfonic acid, a small molecule dye that we predicted would not affect the aggregation kinetics as it has low affinity for all types of amyloid architectures as calculated by computational calculations (Fig. 5C, 5D). Co-incubation with 8-hydroxypyrene 1,3,6 trisulfonic acid did not affect the cytotoxic properties suggesting that orange G was specifically rescuing toxicity by promoting untwisting of the β-sheet. Taken together, these data suggest that out-of-register twisted sheets are cytotoxic while untwisted sheets are relatively non-toxic.

Discussion:

Building on our discovery of segment 28-38 as the toxic oligomeric core of SOD1, here we characterize the segment by determining three atomic structures of its variants and

characterizing their biochemical properties. The three structures we determined possibly reveal three different aggregation states: corkscrew, a soluble oligomer, the untwisted sheet, an out of register intermediate structure and steric zipper representing the fibrillar state.

The crystal structure of the G37R mutant segment suggests that the mutation stabilizes the corkscrew oligomer assembly. More than 180 different ALS-linked familial mutations are known in the 153-residue dimeric protein, SOD1. Among those found in segment 28-38, G37R was one of the first familial mutations found in familial ALS patients (14). In transgenic mouse models, overexpression of the G37R mutant protein leads to rapid disease onset and progression (10) and in cell culture models it has been shown to increase oligomer formation and toxicity (15). The atomic structure of the 28-38 segment with the mutation G37R forms a corkscrew assembly composed of anti-parallel out-of-register β-strands. The change from a small glycine residue to a large arginine residue forms several hydrogen bonds stabilizing the corkscrew assembly. This stabilization of the corkscrew oligomers could explain the increased toxicity of the G37R mutant protein.

Our structures of wild type and G37R mutant SOD1 segment 28-38 suggest that the corkscrew architecture is robust and may accommodate a range of other sequences with the same pattern. That is, small hydrophobic residues alternating with bulky or like-charged residues, forming the concave and convex surfaces of the corkscrew, respectively. Hence, the corkscrew architecture may be implied in pathology of other neurological amyloid diseases.

We obtained the atomic structure of the G37R variant peptide, KBKVWGSIKRL in a novel conformation. Instead of extended β-sheet conformation seen in steric zippers and corkscrew, here the strands are curved forming a dry interface on both faces of the strands. This structure belongs to the growing class of out-of-register steric zippers (16). KDWSFY a short segment of β2-microglobulin and NFGAILS a short segment of IAPP were previously reported to form out-of-register sheet structures (17, 18). An out-of-register sheet structure of a 11-residue segment of IAPP was recently determined (19). Notably, the IAPP structure was composed of a single sheet and was also found to be non-toxic. The 11-residue structure reported here is composed of pairs of sheets and is the longest segment crystallized in an out-of-register mating sheet conformation. Similar to the structure of KDWSFY, the mating sheets of the zipper are not parallel to each other but form a crossing angle of ~45°.

Diffraction of the native corkscrew forming segment KVKVWGSIKGL as well as the G37R mutant KVKVWGSIKRL showed similar diffraction patterns with a diffuse ring at 4.6 Å. The absence of reflections at 10 Å suggests a single sheet architecture of the oligomer different from the classical amyloid cross-β diffraction that shows reflections at 4.8 Å and 10.4 Å. Indeed under shaking conditions the diffraction pattern of KVKVWGSIKGL showed diffraction at 4.6 Å and 11.9 Å.

We determined the crystal structure of the variant peptide, KBKVWGISKRL in an out-of-register untwisted conformation. Orange G that was used as an additive was found to

bind in the interface between the two sheets. Docking simulations also suggested that orange G has a high propensity to bind the interface compared to the twisted corkscrew structure. Based on these results, we hypothesized that binding of orange G stabilizes the untwisted structure and drives the equilibrium from cytotoxic corkscrew oligomers to the untwisted structure. Indeed, in cytotoxicity assays we observed a partial rescue of cytotoxicity upon addition of orange G. Although we cannot rule out if orange G stabilizes other non-toxic intermediates, our results suggest that small molecules designed to stabilize untwisted structure can alleviate cytotoxicity of aggregated proteins.

In summary, our structural studies of the SOD1 segment suggest that twisted sheets are cytotoxic whereas steric zipper and non-twisted sheets are relatively non-toxic.

Acknowledgements: We thank Michael Collazo, Duilio Cascio, and staff at Argonne Photon Source (APS), Northeastern Collaborative Access Team beamline 24-ID-E. The beamline is funded by the National Institute of General Medical Sciences from the National Institutes of Health (P41 GM103403). The Pilatus 6M detector is funded by a NIH-ORIP HEI grant (S10 RR029205). APS is a U.S. Department of Energy (DOE) Office of Science User Facility operated for the DOE Office of Science by Argonne National Laboratory under Contract No. DE-AC02-06CH11357. SS is supported by the UCLA Graduate Division Dissertation Year Fellowship. We thank HHMI and NIH (Ag054022) for support.

Author Contributions: SS and DSE designed research and wrote the manuscript. SS and MRS solved the crystal structures. KM performed the computational predictions. SS and MPH performed the fiber diffraction. SS performed the cytotoxicity assays.

Figure Legends

Fig. 1. Crystal structure of SOD1 segment harboring a familial mutation, G37R. (A) (Left) Frequency of ALS-associated mutations in SOD-1 residues 28-38. (Right) Estimated energies of steric zippers formed by six-residue segments within segment 28-38. Segments KVWGSI and GSIKGL have energies of −23 kcal/mol or lower and are predicted to form fibrils. (B) 2.9 Å crystal structure of the toxic oligomeric core of SOD1, residues 28-38 with the familial mutation G37R reveals a corkscrew assembly of anti-parallel β-strands with a hydrophobic cleft composed of valine and isoleucine residues. 20 strands form one complete turn with a pitch length of 59 Å and diameter of 38 Å. (C) Arg37 forms multiple inter- and intra-chain interactions that increase the stability of the assembly. (Top) Shown here Arg37 of β7 forms an intra-chain hydrogen bond with Leu38 and an inter-chain hydrogen bond with Leu38 of β9. (Bottom) Arg37 also forms inter-chain hydrogen bonds. Shown here Arg37 of β14 is engaged in hydrogen bonds with Leu38 of β12 and Arg37 of β16.

Fig. 2. Polymorphic form of the segment 28-38 with the familial mutation G37R. (A) Atomic structure of the segment 28-38 with familial mutation G37R at 1.8 Å resolution reveals a novel architecture of highly curved sheets mating via stacking of aromatic side chains of W32 residue. The curved architecture enables both faces of the sheets to exclude water molecules as shown here in side and top views. (B) The weak interface composed of W32 stacking forms a pocket where small molecules can bind. Orange G (shown in orange sticks) was co-crystallized and found to bind in the pocket. (C) Electron density map contoured at 1.0 σ showing clear density for orange G. (D) Orange G

stabilizes the assembly by forming a network of hydrogen bonds with K30 and W32 of one sheet and K30 of the opposing sheet. Water molecules are colored red.

Fig. 3. Segment 30-KVWGSI-35 of SOD1 forms a steric zipper assembly. (A) 1.45 Å resolution structure of segment KVWGSI shows two β-sheets composed of anti-parallel β-strands forming a class 7 steric zipper via face to back stacking. Shown here in top (left) and side (right) views. Trifluoroacetic acid (TFA) is colored orange. (B) The two sheets do not pack tightly due to the bulky tryptophan side chain in the inner interface, (C) Instead of a flat parallel packing, the W32 side chain protrudes along the fiber axis and aligns with the G33 of strand above it as shown here in sphere representation, which causes staggering of the sheets relative to each other.

Fig. 4. Structural comparison of segment 28-38 and its variants. (A) The native 28-38 segment (PDB ID: 5DLI) forms a corkscrew-like assembly of anti-parallel, out-of-register β-strands. 16 strands form one complete turn with 71 Å pitch length and 25 Å diameter. (B) The mutant segment with a familial mutation, G37R forms a corkscrew-like assembly but with a different pitch length and diameter. 20 strands form one complete turn with 59 Å pitch length and 38 Å diameter. (C) A second form of the variant segment was obtained which revealed a novel architecture of curved out-of register sheets. The sheets are not exactly perpendicular to fibril axis and instead are tilted with a crossing angle of ~45°. (D) A shorter 6-residue segment within 28-38 forms a steric zipper composed of pairs of β-sheets. The sheets are perpendicular to the fibril axis with a 0° crossing angle. (E) Comparison of diffraction patterns of the different variant segments.

(Top) 28-38 and G37R mutant segments show diffuse diffraction rings at 4.6 Å. The G37R segment forming out-of-register pairs of sheets forms sharp diffraction rings at 4.75 Å and 9.5 Å. (Bottom) The segment 28-38 and the sheet forming structures under shaking conditions reveal cross-β diffraction indicative of pairs of sheets.

Fig. 5. Familial mutant segment is cytotoxic and addition of orange G partially alleviates the cytotoxicity. (A) Segment KVKVWGSIKRL was aggregated under quiescent and shaking conditions at different concentrations and its cytotoxicity was assessed thereafter. Under oligomer-forming, quiescent conditions the segment was more cytotoxic. (B) Electron micrographs of the segment under different conditions. Some fibrils can be seen in shaking conditions but not under quiescent conditions suggesting that cytotoxicity is a property of soluble corkscrew-like oligomers. (C,D) Docking simulations of the different structures determined here and the small molecule dye orange G. Binding Energy is reported in Rossetta Energy Units (REU). Notice that orange G has lower binding energy to form 2 than wild type. A small molecule 8-hydroxypyrene 1,3,6 – trisulfonic acid was used as a negative control and had high binding energies to wild type corkscrew as well as untwisted structure. (E) Cytotoxicity of 800 μM segment when aggregated in the presence of 100 μM orange G or a non-binding control molecule. Addition of orange G alleviates the cytotoxic effects suggesting that the untwisted curved sheet architecture is relatively benign. Results shown as Mean+SD. Statistical significance was analyzed by one-way ANOVA (ns not significant, ** $p < .01$, **** $p < .0001$)

Figures

Fig. 1

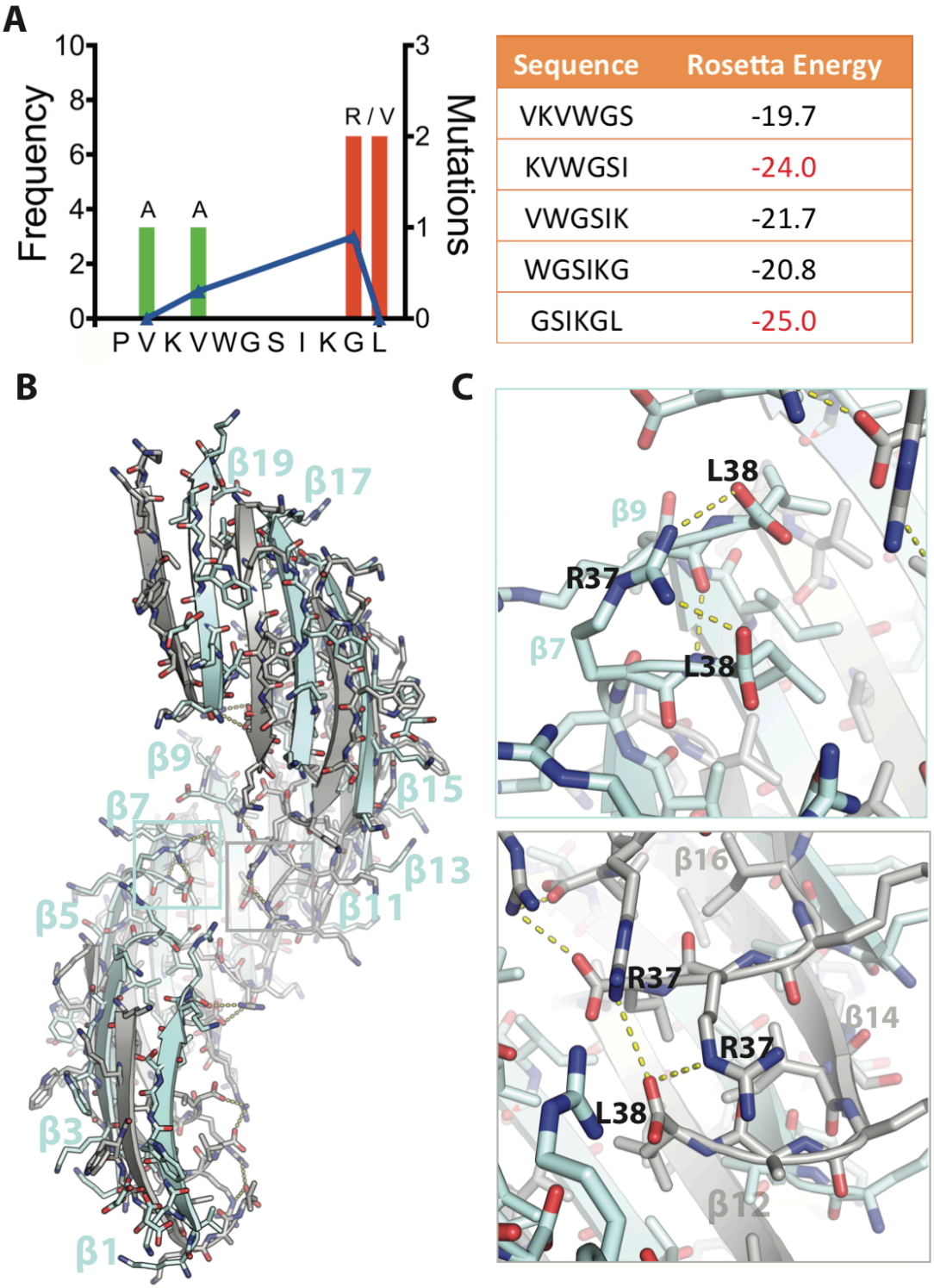

Sequence	Rosetta Energy
VKVWGS	-19.7
KVWGSI	-24.0
VWGSIK	-21.7
WGSIKG	-20.8
GSIKGL	-25.0

Fig. 2

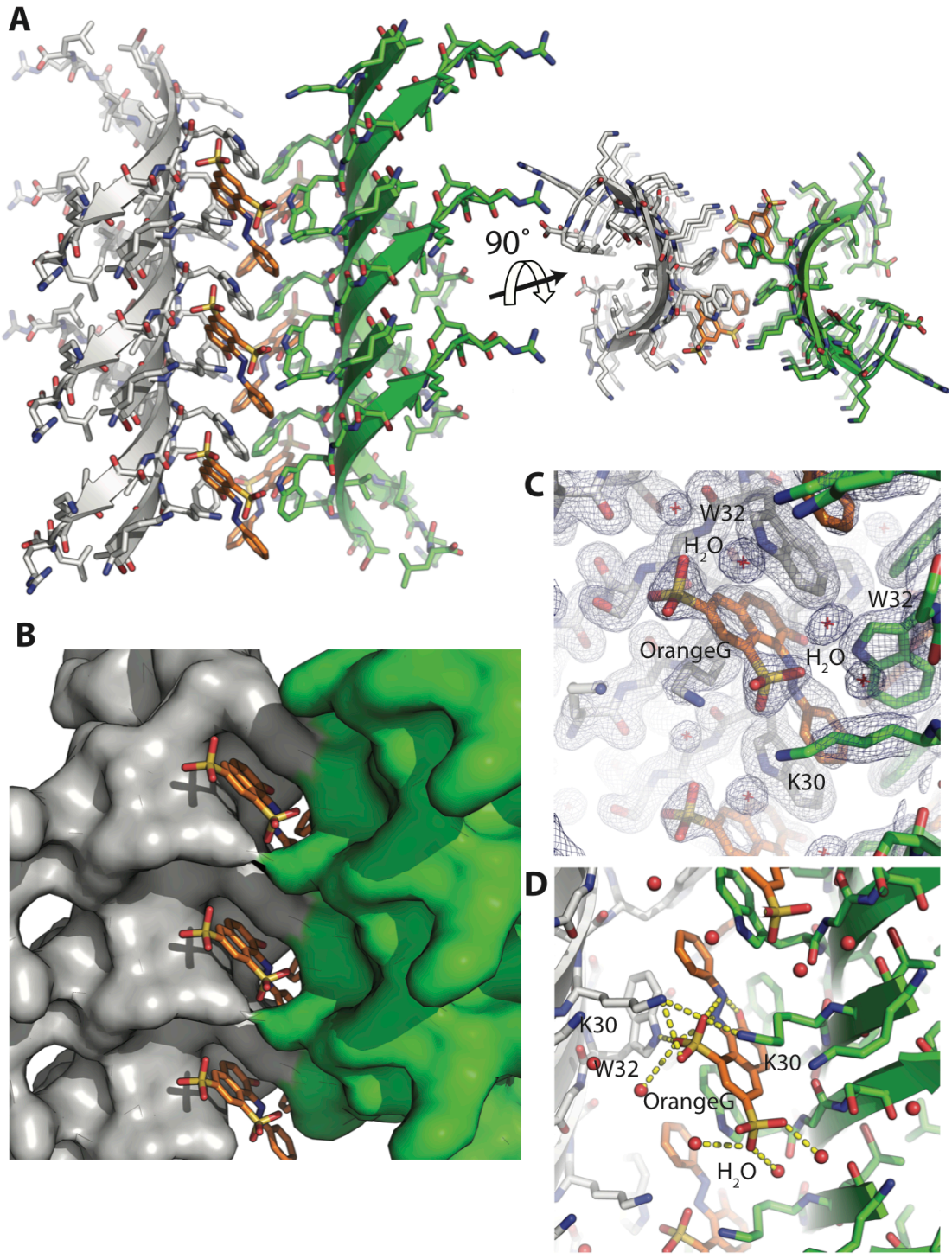

Fig. 3

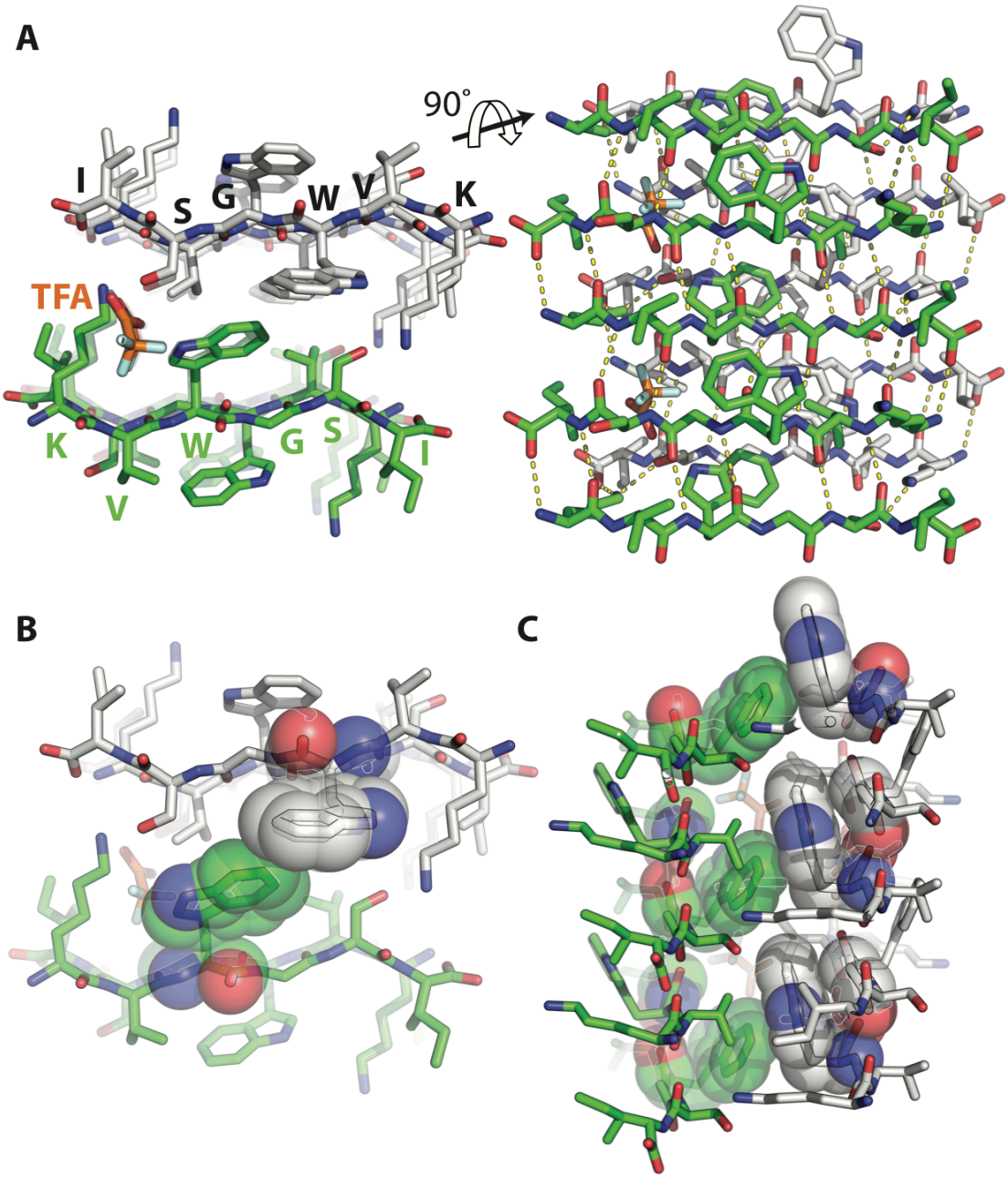

Fig. 4

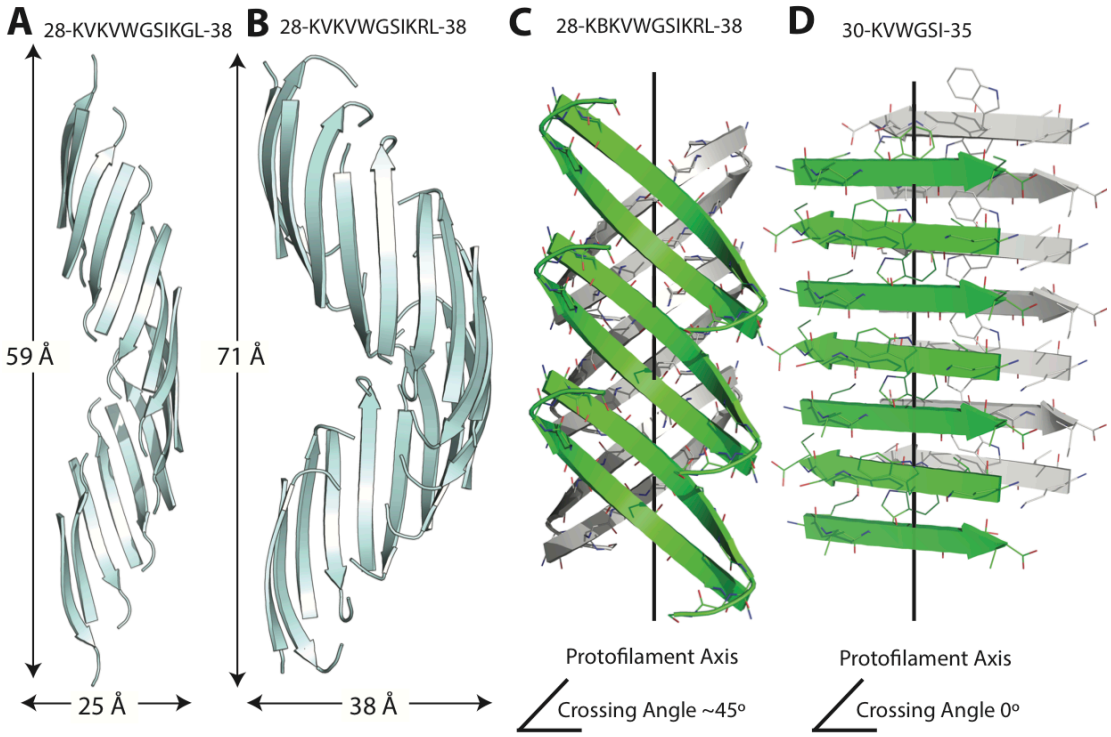
A 28-KVKVWGSIKGL-38
B 28-KVKVWGSIKRL-38
C 28-KBKVWGSIKRL-38
D 30-KVWGSI-35
59 Å
71 Å
25 Å
38 Å
Protofilament Axis
Crossing Angle ~45°
Protofilament Axis
Crossing Angle 0°

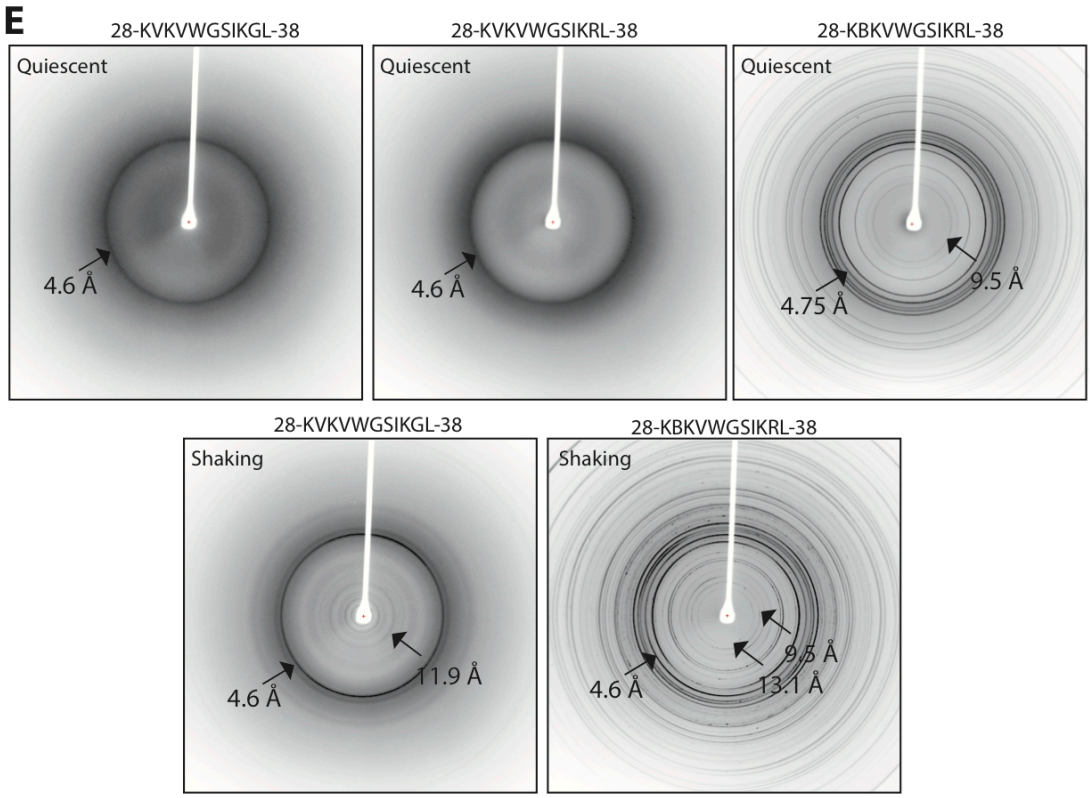
E
28-KVKVWGSIKGL-38
Quiescent
4.6 Å
28-KVKVWGSIKRL-38
Quiescent
4.6 Å
28-KBKVWGSIKRL-38
Quiescent
4.75 Å
9.5 Å
28-KVKVWGSIKGL-38
Shaking
4.6 Å
11.9 Å
28-KBKVWGSIKRL-38
Shaking
4.6 Å
9.5 Å
13.1 Å

Fig. 5

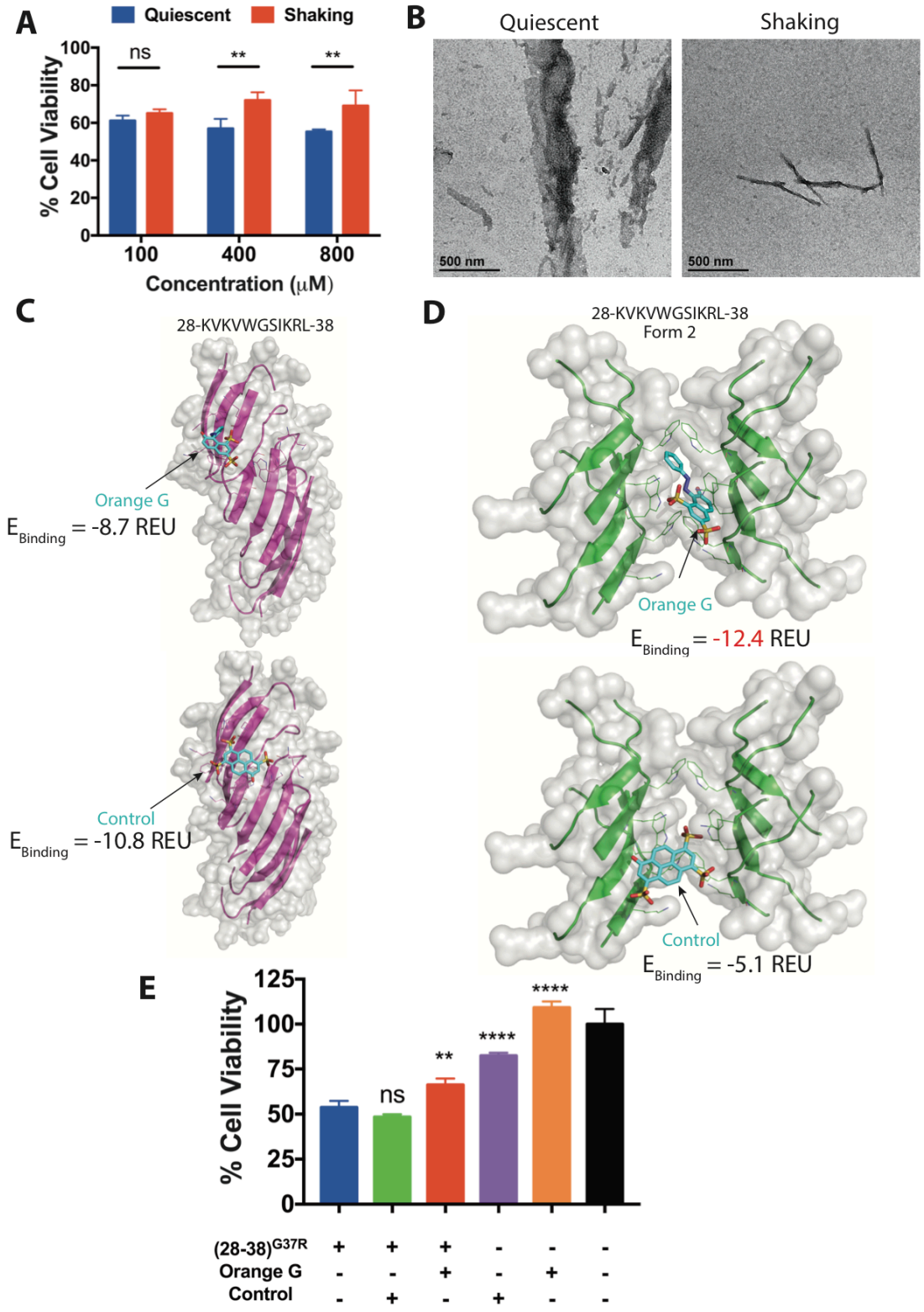
A
Quiescent
Shaking
% Cell Viability
ns
**
**
100
80
60
40
20
0
100
400
800
Concentration (μM)
B
Quiescent
Shaking
500 nm
500 nm
C
28-KVKVWGSIKRL-38
Orange G
E Binding = -8.7 REU
Control
E Binding = -10.8 REU
D
28-KVKVWGSIKRL-38
Form 2
Orange G
E Binding = -12.4 REU
Control
E Binding = -5.1 REU
E
% Cell Viability
125
100
75
50
25
0
ns
**
****
****
(28-38)G37R + + + - - -
Orange G - - + - + -
Control - + - + - -

Table 1: Data collection and refinement statistics

	KVKVWGSIKRL (Form 1)	KBrKVWGSIKRL (Form 2)	KVWGSI
Beam line	APS 24-ID-E	APS 24-ID-E	APS 24-ID-E
Resolution Å	2.9	1.80	1.45
Total unique reflections	5444	2330	1738
Total reflections observed	27350	7194	11632
Space group	$P3_12_1$	C2	$P2_12_12_1$
Rsym	18.3% (90.7%)	21.1%(197.9%)	16.6 %(55.0%)
I/σ	8.9 (1.0)	4.06(0.48)	8.6(1.6)
Completeness	98.9 %	96.6	89.6
Wavelength (Å)	0.9791	0.9791	0.9791
Unit cell dimensions a b c (Å) α β γ (°)	59.61 59.61 98.92 90.0 90.0 120.0	56.94 11.64 44.93 90.0 127.3 90.0	9.51 20.28 44.24 90.0 90.0 90.0
Refinement			
Resolution (Å)	2.8 - 45.8	1.8 - 35.7	1.4 - 22.1
Reflections for refinement	5422	2327	1564
R_{free}/R_{work} (%)	25.04/21.32	26.70/23.03	16.97/17.06
Molecules in the Asymmetric unit	10	2	2
Solvent content (%)	71	50	24
Matthews coefficient	4.19	2.45	1.61
Total water molecules	14	16	6
Glycerol molecule	1	0	0

Malonate molecule	3	0	0
TFA molecule	0	0	1
Orange G	0	1	0
Rmsd bond length (Å)	0.010	0.010	0.020
Rmsd angles (°)	1.18	1.25	2.00
Ramachandran plot **Allowed** **Generous** **Disallowed**	 96 4.44 0	 94 5.56 0	 100 0 0

Table 2: Comparison of shape complementarity (Sc) and buried surface area (A_b) of oligomers of SOD1 segments.

	KVKVWGSIKRL Form 1	KVKVWGSIKRL Form 2	KVWGSI
Sc	0.76	0.76	0.64
A_b (Å^2)	1195	1047	621
A_b/Residue (Å^2)	109	95	104

For the Sc calculation, we examined the interface between one chain and the remaining chains of the assembly.

A_b values were calculated using AREAIMOL. The area buried was calculated by subtracting the solvent accessible surface area of one chain of the assembly from the total solvent accessible surface area of an isolated chain. Notice that the N-terminal prolyl residue of these SOD1 segments has been replaced by lysyl to improve solubility.

Materials and Methods:

Crystallization: All peptides were commercially obtained from Genscript inc. with more than 98% purity. All data were collected at the Advanced Photon Source (Chicago, IL) on beamline 24-ID-E and data were processed using DENZO and SCALEPACK or XDS (20). Structures were built using COOT (21). Model refinement was performed using REFMAC (22) and BUSTER (23). Figures were generated using PyMOL (24).

28-KVKVWGSIKRL38: Crystals of segment 28-38 with P28K and G37R substitution were grown by hanging drop vapor diffusion using VDX plates (Hampton Research, Aliso, Viejo, CA). Lyophilized peptide was dissolved to 50 mg/ml in 50 mM Tris-base buffer, 1 mM Orange G. The reservoir solution contained 0.3 M sodium malonate and 15% PEG 3350. Crystallization drops were prepared by mixing peptide with reservoir in a 3:1 ratio, in a total volume of 4 μL. The crystals were subsequently flash frozen in liquid nitrogen and mounted with CrystalCap HT Cryoloops (Hampton Research, Aliso Viejo, CA). Four strands composed of the core of the corkscrew structure PDB ID: 5DLI, residues VKVWGSI were used as the initial model for molecular replacement.

28-KBKVWGSIKRL-38: Lyophilized peptide (KBKVWGSIKRL, B represents the non-natural amino acid bromo-allyl valine) was dissolved to 50 mg/ml in 50 mM Tris-base buffer with 1 mM Orange G. The reservoir solution contained 0.1 M HEPES

pH 7.5, 0.2 M sodium citrate and 15% MPD. Needle-like crystals appeared overnight and were directly flash frozen from the original screening plate.

30-KVWGSI-35: Lyophilized peptide was dissolved to 50 mg/ml in water and filtered by 0.1 μm filter. Crystals were grown by hanging drop vapor diffusion using VDX plates (Hampton Research, Aliso, Viejo, CA). Crystallization drops were prepared by mixing peptide with reservoir in a 2:1 ratio, in a total volume of 3 μL. The reservoir solution contained 4 M Sodium Formate. Crystals were mounted on pulled glass capillaries without any cryoprotectant. A pair of anti-parallel β-strands was used as an initial model for molecular replacement.

Fiber Diffraction: Peptide segments were dissolved in 50 mM tris-base buffer at 25 mg/ml and incubated at 37 °C without agitation to form oligomers for four days. For fibril preparations, the peptide segments were incubated at 37 °C in Torry Pine shakers for four days.

Segment Aggregation: Peptide segments were aggregated by incubation at 37 °C for 12 hours with agitation in 50 mM tris-base buffer and added to cultured neurons. For testing the effect of small molecules, peptides were co-incubated with Orange G (Sigma Aldrich, Cat # 861286) and 8 hydroxypyrene 1,3,6 – trisulfonic acid (Sigma Aldrich, Cat # 1529) at 37 °C overnight without agitation and added to cultured cells at a final concentration of 800 μM peptide and 100 μM small molecule.

Ligand Docking: Three dimensional structures of the ligands used for docking simulation were downloaded from the PubChem Compound Database (CID=24181578, 4254851)(25). We generated the ligand perturbation ensemble using the method described previously (26). A torsion angle deviation of ±5° for each rotatable bond of the ligand was applied to generate 100 conformations for each ligand. Ligand docking was performed using the HighResDocker protocol in Rosetta version 3.5, using the talaris2014 energy function (27). Docking poses were sampled in a 7 Å box centered at the known binding site of Orange G to the variant form 1, or to the corresponding residues in the corkscrew structure. Small ligand perturbations were coupled with cycles of side chain repacking, in which rotamers of side chains around the ligand are optimized in a Monte-Carlo minimization algorithm. Ligand poses were ranked based on lowest binding energy.

Cell Culture: Rat Neuroblastoma (PC12) cells were obtained from ATCC (CRL 1721). Cells were cultured in RPMI 1640 media with 10% heat inactivated horse serum and 5% fetal bovine serum.

Cytotoxicity Assays

Cells were plated at 10,000 cells per well in 96-well tissue culture plates and allowed to adhere overnight before treatment with aggregated peptides. Upon treatment with the aggregated peptides, cells were incubated overnight and cell viability was measured using the commercially available MTT assay (Promega Cat#G4100) according to the manufacturer's protocol with 4 hour incubation with the MTT reagent. All data were

normalized using buffer as 100% viability and 0.2% SDS as 0% viability. Experiments were performed in triplicates.

Electron Microscopy

Each 3-5 μL sample was spotted directly on freshly glow-discharged carbon-coated electron microscopy grids (Ted Pella, Redding, CA). After 4 min incubation, grids were rinsed twice with 5 μL distilled water and stained with 5 μl of 2% uranyl acetate for 1 min. Excess uranyl acetate was removed by blotting and specimens were examined on a T-12 electron microscope at an accelerating voltage of 80 kV. Images were recorded digitally by wide angle (top mount) BioScan 600W 1 × 1K digital camera (Gatan, Pleasanton, CA).

References:

1. Eisenberg D, Jucker M (2012) The Amyloid State of Proteins in Human Diseases. *Cell* 148(6):1188–1203.

2. Nelson R, et al. (2005) Structure of the cross-β spine of amyloid-like fibrils. *Nature* 435(7043):773–778.

3. Sawaya MR, et al. (2007) Atomic structures of amyloid cross-β spines reveal varied steric zippers. *Nature* 447(7143):453–457.

4. Bernstein SL, et al. (2009) Amyloid-β protein oligomerization and the importance of tetramers and dodecamers in the aetiology of Alzheimer's disease. *Nat Chem* 1(4):326–331.

5. Celej MS, et al. (2012) Toxic prefibrillar α-synuclein amyloid oligomers adopt a distinctive antiparallel β-sheet structure. *Biochem J* 443(3):719–726.

6. Laganowsky A, et al. (2012) Atomic View of a Toxic Amyloid Small Oligomer. *Science* 335(6073):1228–1231.

7. Liu C, et al. (2011) Characteristics of Amyloid-Related Oligomers Revealed by Crystal Structures of Macrocyclic β-Sheet Mimics. *J Am Chem Soc* 133(17):6736–6744.

8. Guareschi S, et al. (2012) An over-oxidized form of superoxide dismutase found in sporadic amyotrophic lateral sclerosis with bulbar onset shares a toxic mechanism with mutant SOD1. *Proc Natl Acad Sci* 109(13):5074–5079.

9. Valentine JS, Hart PJ (2003) Misfolded CuZnSOD and amyotrophic lateral sclerosis. *Proc Natl Acad Sci* 100(7):3617–3622.

10. Wong PC, et al. (1995) An adverse property of a familial ALS-linked SOD1 mutation causes motor neuron disease characterized by vacuolar degeneration of mitochondria. *Neuron* 14(6):1105–1116.

11. Goldschmidt L, Teng PK, Riek R, Eisenberg D (2010) Identifying the amylome, proteins capable of forming amyloid-like fibrils. *Proc Natl Acad Sci* 107(8):3487–3492.

12. Necula M, Kayed R, Milton S, Glabe CG (2007) Small Molecule Inhibitors of Aggregation Indicate That Amyloid beta Oligomerization and Fibrillization Pathways Are Independent and Distinct. *J Biol Chem* 282(14):10311–10324.

13. Landau M, et al. (2011) Towards a Pharmacophore for Amyloid. *PLoS Biol* 9(6):e1001080.

14. Rosen DR, et al. (1993) Mutations in Cu/Zn superoxide dismutase gene are associated with familial amyotrophic lateral sclerosis. *Nature* 362(6415):59–62.

15. McAlary L, Aquilina JA, Yerbury JJ (2016) Susceptibility of Mutant SOD1 to Form a Destabilized Monomer Predicts Cellular Aggregation and Toxicity but Not In vitro Aggregation Propensity. *Front Neurosci* 10. doi:10.3389/fnins.2016.00499.

16. Eisenberg DS, Sawaya MR (2017) Structural Studies of Amyloid Proteins at the Molecular Level. *Annu Rev Biochem* 86(1). doi:10.1146/annurev-biochem-061516-045104.

17. Liu C, et al. (2012) Out-of-register β-sheets suggest a pathway to toxic amyloid aggregates. *Proc Natl Acad Sci* 109(51):20913–20918.

18. Soriaga AB, Sangwan S, Macdonald R, Sawaya MR, Eisenberg D (2016) Crystal Structures of IAPP Amyloidogenic Segments Reveal a Novel Packing Motif of Out-of-Register Beta Sheets. *J Phys Chem B* 120(26):5810–5816.

19. Krotee P, et al. (2017) Atomic structures of fibrillar segments of hIAPP suggest tightly mated β-sheets are important for cytotoxicity. *eLife* 6. doi:10.7554/eLife.19273.

20. Kabsch W (1993) Automatic processing of rotation diffraction data from crystals of initially unknown symmetry and cell constants. *J Appl Crystallogr* 26(6):795–800.

21. Emsley P, Cowtan K (2004) *Coot* : model-building tools for molecular graphics. *Acta Crystallogr D Biol Crystallogr* 60(12):2126–2132.

22. Vagin AA, et al. (2004) *REFMAC* 5 dictionary: organization of prior chemical knowledge and guidelines for its use. *Acta Crystallogr D Biol Crystallogr* 60(12):2184–2195.

23. Bricogne G, et al. BUSTER version 1.10.0. Cambridge, United Kingdom: Global Phasing Ltd.

24. Delano W The PyMOL Molecular Graphics System. (2002).

25. National Center for Biotechnology Information. PubChem BioAssay Database.

26. Jiang L (13AD) Structure-based discovery of fiber-binding compounds that reduce the cytotoxicity of amyloid beta. eLife 2013;2:e00857.

27. Lemmon G, Meiler J (2012) Rosetta Ligand Docking with Flexible XML Protocols. *Computational Drug Discovery and Design*, ed Baron R (Springer New York, New York, NY), pp 143–155.

Chapter 4: Inhibition of synucleinopathic seeding by structure-based designed inhibitors

Abstract: Seeding, in the context of amyloid disease, is the sequential transfer of pathologic protein aggregates along connected tissues. This process contributes to progression and severity of neurodegenerative diseases. To date, there are no therapeutics that specifically target seeding, in part, due to lack of information of the structural properties of pathological seeds. Here we use a rational approach based on the atomic structure of the core of PD-related α-synuclein fibrils, to design small peptidic inhibitors. The inhibitors prevent aggregation of α-synuclein in vitro and in cell culture models. The inhibitors also show efficacy in preventing seeding by patient-derived α-synuclein fibrils both in vitro and in cell culture models. Our results suggest that pathological seeds of α-syn contain steric zippers and suggest a therapeutic approach targeted at the spread and progression that may be applicable for PD and related synucleinopathies.

Title: Inhibition of synucleinopathic seeding by structure-based designed inhibitors

Authors: Smriti Sangwan[1], Kevin Murray[1], Shruti Sahay[1], Lin Jiang[2], Michel Goedert[3] and David S. Eisenberg[1]

Affiliations: [1]Howard Hughes Medical Institute, UCLA-DOE and Molecular Biology Institutes, Department of Biological Chemistry Los Angeles, California, USA. [2]Department of Neurology, David Geffen School of Medicine, University of California, Los Angeles, Los Angeles, United States. [3]MRC Laboratory of Molecular Biology, Cambridge, UK.

Corresponding Author: David S. Eisenberg, email: david@mbi.ucla.edu

Abstract:

Seeding, in the context of amyloid disease, is the sequential transfer of pathologic protein aggregates along connected tissues. This process contributes to progression and severity of neurodegenerative diseases. To date, there are no therapeutics that specifically target seeding, in part, due to lack of information of the structural properties of pathological seeds. Here we use a rational approach based on the atomic structure of the core of PD-related α-synuclein fibrils, to design small peptidic inhibitors. The inhibitors prevent aggregation of α-synuclein in vitro and in cell culture models. The inhibitors also show efficacy in preventing seeding by patient-derived α-synuclein fibrils both in vitro and in

cell culture models. Our results suggest that pathological seeds of α-syn contain steric zippers and suggest a therapeutic approach targeted at the spread and progression that may be applicable for PD and related synucleinopathies.

Introduction:

Parkinson's disease (PD), dementia with lewy bodies (DLB) and multiple system atrophy (MSA) are together classified as Synucleinopathies, a class of neurodegenerative diseases characterized by the pathological accumulation of the protein, α-synuclein (α-syn) in neuronal cells (1). Together these make up the second most common form of neurodegenerative disease. α-synuclein, a 140 amino acid protein is found in amyloid deposits in neuronal cells in disease conditions. A causative link between α-syn amyloid formation and disease progression is supported by the findings that gene duplications and familial mutations that increase amyloid load also cause early-onset PD, and more than 90% sporadic PD patients stain positive for α-syn deposits.

Based on structural studies, a number of different models for α-syn fibrils have been proposed. Limited proteolysis and NMR studies suggest that the fibril core is composed of residues 30-100 (2). Crystal structures and NMR studies suggest different models of α-syn fibrils. In one model based on crystal structures of short segments, two monomers per sheet form extended steric zippers (3). In a second ssNMR-based model, a greek key topology with one monomer per sheet has been shown (4). Taken together these studies suggest that α-syn can form polymorphic fibrillar architectures.

The segment 68-78 of α-syn termed NACore forms the core of α-syn fibrils. NACore, resides within the 35-residue NAC (non-amyloid β component) domain found in amyloid deposits (3). NACore aggregates readily, and the aggregates display properties such as diffraction pattern and cytotoxicity similar to full-length α-syn. Additionally, β-synuclein, a homologue does not contain residues 74-84 and is not found in amyloid deposits, and removal of residues 71-82 has been shown previously to reduce the aggregation and toxicity in vitro and in a drosophila model (5, 6). Additionally, a modification at Thr72 prevents its aggregation propensity

Apart from the spontaneous aggregation of intracellular α-syn into amyloid fibrils, a second phenomenon that contributes to disease progression is the prion-like spread of α-syn aggregates (7). Braak staging has shown that pathology gradually spreads over time through connected brain regions, and cell culture and animal models show that small amounts of α-syn aggregates can act as seeds and induce aggregation of the native protein (8–12). Although distinct from canonical prions that can be transmitted from person to person, this phenomenon of 'seeding' seems the driver of disease progression.

Although α-syn amyloid formation has been extensively characterized, little headway has been made in developing therapeutics that can prevent spontaneous α-syn aggregation or reduce the prion-like spread. Among promising approaches are antibodies that sequester α-syn aggregates and small molecule stabilizers that bind α-syn monomers (13, 14). Here we report a third class of inhibitors that bind α-syn seeds and prevent their growth and

elongation. The inhibitors are designed using the atomic structure of NACore as a template. We show the efficacy of these inhibitors in preventing fibril formation and seeding in vitro and in cell-based seeding model systems.

Results:

1. Rational design of α-synuclein aggregation inhibitors: We utilized the atomic structure of NACore [68-GAVVTGVTAVA-78] as a template and using computational and structure-based approaches designed peptidic inhibitors. The atomic structure of NACore revealed a pair of self-complementary β-sheets forming a steric zipper (15). The inhibitors are predicted by Rossetta-based computational modeling to bind the steric zipper interface and 'cap' the fibrils. We identified 3 candidates, S37, S61 and S71 that bind favorably with one or both ends of the zipper (Fig. 1). The binding energies and shape complementarity of the three inhibitors are also favorable (Fig 1B). All the inhibitors retain most residues of the native sequence of NACore but contain one or more modified residues. Rodriquez et al. showed that a smaller 9-residue segment within NACore [69-AVVTGVTAV-77] aggregates slower than NACore and the structure is similar to NACore. In order to prevent the self-aggregation of our designed inhibitors, we used the shorter segment along with one or more modifications. S37 has a W mutation at Thr72 and an additional poly-lysine tag at the C-terminus to induce charge-charge repulsion. It is predicted to bind both tips of the steric zipper fibril. S61 and S62 retain the same inhibitor sequence as S37 but instead of poly-lysine tag, a TAT tag is added to aid solubility and prevent self-aggregation. S71 has a methylated glycine at Gly73 that

weakens hydrogen bonding along the β-sheet and an additional TAT tag for solubility and cell penetration.

2. Designed inhibitors prevent aggregation in vitro: We tested the efficacy of the inhibitors in an in vitro aggregation assay. Recombinantly purified α-syn was aggregated in the presence of the inhibitors and monitored by measuring fluorescence of Thioflavin T, an amyloid binding dye. All three inhibitors prevented aggregation with a significant reduction in ThT fluorescence (Fig. 1C, 1D, 1E).

3. α-syn aggregates formed in the presence of inhibitors show reduced seeding in cell culture models: We tested the efficacy of the inhibitors in preventing aggregation in a cell culture model. For these assays, we utilized two HEK293T cells that stably express YFP-labeled full-length WT α-syn and A53T α-syn (16). In this model, lipofectamine-mediated transfection of recombinant fibrils leads to aggregation of the endogenous YFP-labeled protein that are seen as fluorescent puncta. Additionally, these puncta increase in size and number over time. This proliferation of aggregates over time is indicative of a 'seeding' phenomenon whereby a small amount of amyloid fibrils induces aggregation of the endogenous protein. First we tested the parent peptide segment, NACore to check its effect on seeding. α-syn was aggregated in the presence of molar excess of NACore (Fig. 2B). The mixture was transfected in cells and puncta formation was visualized and the number of puncta were counted as particles per well. As expected, NACore did not cause a significant reduction in puncta formation in either cell line. Next we aggregated 50 μM α-syn in the presence of 500 μM, 250 μM, 100 μM and

50 μM inhibitor corresponding to 10, 5, 2 and 1 fold excess. The mixture was then transfected in cells and aggregation was monitored over time for up to 3 days by fluorescence imaging (Fig. 2A). S37 caused a significant reduction in seeding for up to 2 days in both WT and A53T expressing cell lines. Similar to S37, S61 (Fig 2D) also caused a reduction in puncta formation with maximum efficacy at 2, 5 and 10 fold excess in both cell lines. Aggregates formed in the presence of S62 (Fig. 2E) were also seeding incompetent with significantly less particles forming at all inhibitor concentrations. S71 was tested at equimolar and sub-stoichiometric ratios and found to reduce the seeding potency of the aggregates (Fig. 2F). These results suggest that the inhibitors prevent formation of seeding competent aggregates.

4. Co-transfection of α-syn fibrils with the inhibitors prevents seeding by fibrils in cell culture: Next, we tested the efficacy of the inhibitors to prevent seeding in the cell culture model (Fig. 3A). We transfected the α-syn fibrils along with the different inhibitors. NACore, the parent aggregating peptide did not affect the seeding potency of α-syn fibrils (Fig. 3B). S37 caused significant reduction in seeding in both cell lines at 12.5 μM and 6.25 μM concentrations for up to 2 days (Fig. 3C). S61 at concentrations of 2.5 μM and 1.25 μM caused a prolonged reduction of seeding lasting up to 6 days in WT α-syn cells and 2 days in A53T α-syn HEK cells (Fig. 3D). S62 was effective at concentrations of 12.5 μM and 6.25 μM in both cell lines (Fig. 3E). S71 was effective at all concentrations. Together these results suggest that inhibitors can cap fibril seeds and prevent their elongation.

5. Fibrils extracted from PD brain tissues seed in vitro and increase seeding potency in cell culture: Next we extracted insoluble protein aggregates from frozen autopsy PD brain tissues. We obtained tissues from 4 different subjects including the substantia nigra and frontal regions of one subject and temporal and frontal regions of other subjects. Using previously described protocols (17) that included precipitation with the ionic detergent sarkosyl, we extracted insoluble protein aggregates (Fig. 4A). All samples robustly seeded α-syn aggregation in vitro and in our cell culture model. In vitro addition of 2 % seeds increased the ThT fluorescence 4 to 10 fold (Fig. 4B, 4C, 4D) along with a small decrease in the lag time. The seeded samples were then transfected in HEK cells. Consistent with the ThT assay, all seeded samples induced rapid puncta formation (Fig. 4E, 4F, 4G). Thus, fibrils extracted from PD brain tissues seeds recombinant protein, and the aggregates formed upon seeding induce rapid puncta formation in cell culture.

6. Inhibitors prevent seeding by PD fibrils in vitro and in cell culture: We tested the effect of the different inhibitors in preventing α-syn aggregation in the presence of PD extracted seeds. S61 and S62 were most effective showing efficacy against all seeds as measured by ThT fluorescence assay (Fig. 5). S71 also reduced aggregation of two different seeds (Fig. 5B, 5D) whereas S37 showed marginal reduction in ThT fluorescence (Fig. 5D). Next we tested the seeding potency of the α-syn aggregates formed in the presence of PD seeds and the different inhibitors (Fig. 6A). Aggregates formed in the presence of S71 (Fig. 6B, 6C and 6D) did not induce puncta formation in both WT and A53T expressing HEK cells. S61 also showed efficacy (Fig. 6C).

Consistent with the in vitro assay, S37 was not effective in reducing the seeding potency of aggregates. Together these results suggest that S61 and S71 can prevent formation of seeding competent fibrils.

7. Inhibitors prevent seeding of PD fibrils seeded α-syn fibrils: We tested the efficacy of the inhibitors in preventing seeding by PD fibrils in cell culture. α-syn aggregates formed in the presence of PD fibrils were transfected in WT HEK cells along with the different inhibitors (Fig. 7A). S37 prevented puncta formation for up to 2 days for two different PD filaments at concentrations of 12.5 μM – 1.25 μM (Fig. 7B). Similar to S37, S61 also showed efficacy for up to 2 days at concentrations of 12.5 μM - 1.25 μM, and S71 also prevented seeding at similar concentrations. These results suggest that inhibitors robustly prevent seeding in cell culture.

Discussion:

We describe a structure-based approach to halt α-syn aggregation. We hypothesized that the atomic structure of NACore is preserved in α-syn seeds and recruits the endogenous protein into a zipper conformation. Using the atomic structure of NACore, we developed inhibitors that hinder fibril formation and tested their efficacy in vitro and in cell culture. The inhibitors are optimized to cap the ends of the fibril, preventing further addition of monomers. We used the software Rosetta to design peptide sequences that interact favorably with the NACore segment. The energy function used by Rosetta takes into account electrostatic interactions, hydrogen bonding, Van der Waals forces, among other

terms to assess binding energy. Once a specific residue has been shown to produce favorable binding in a certain position of the designed peptide, it can be fixed and prevented from further design, while the rest of the sequence is further refined. We performed this process of fixing and redesign iteratively until an optimal set of sequences was identified. This rational design process allowed for computationally sampling of orders of magnitude more inhibitor sequences than what was experimentally feasible to test.

To find the most effective inhibitors, nearly 100 different designs were tested empirically with sequential rounds of optimization on the inhibitor design. For example, we observed that the location of the tag on N or C terminus can affect its efficiency. Additionally, the type of modification added can also affect its efficacy. In our case, only a Trp substitution at Thr72 was effective whereas Arg substitution was not. Although the computational approach is not powerful enough to identify one successful design, it can narrow our search for candidate inhibitors, which can then be refined through rational design.

The efficiency of capping inhibitors in preventing seeding was tested using a cell-based assay. In this system, transfection of nanomolar amounts of α-syn seeds caused endogenous protein aggregation. The aggregates display amyloidogenic properties - binding to amyloid-specific small molecules, faithfully transferred upon cell division and remarkable specificity (16). For example, α-syn fibrils can only seed α-syn protein into aggregates. Notably, in this system we do not observe acute cell death upon formation of aggregates with only a mild slowing of cell proliferation. Our inhibitors prevented puncta

formation in this system with a single administration of inhibitors effective for 2-3 days. It will be interesting to test if the inhibitors can prevent propagation of seeds over a long period of time by dosing at regular intervals of time. The cell culture seeding assay it does not recapitulate other features of neurodegenerative diseases, notably cellular toxicity and the role of neuronal and non-neuronal cell types. The promising results in the cell culture assay merit testing our inhibitors in other model systems.

Patient-extracted fibrils differ in seeding capacity and display strain-like characteristics. In vitro the PD patient extracted fibrils caused dramatic increase in α-syn aggregation, and in cell culture model the seeded samples increased puncta formation. Notably, unlike previous reports where patient derived α-syn filaments seeds in cell culture, in our assays we did not observe seeding in cell culture (18, 19). Previous reports utilized substantia nigra tissues whereas we used frontal and temporal tissues, which might differ in seeding potency. Indeed in previous reports, fibrils extracted from different brain regions have been shown to differ in seeding capacity reminiscent of different strains (18). Furthermore, the different inhibitors varied in efficiency against different seeds. For example, S61 was effective against seeds A and B only whereas S71 was effective against seeds B and D. Recently, an NMR structure of full length α-syn fibrils was reported in which the NACore segment was not found in an extended zipper conformation although the segment 68-78 is found in the core of the fibril (4). It is conceivable that the NMR structure and the steric zipper structure are different polymorphs. In the absence of a diagnostic method to identify different polymorphs in

human subjects, theoretically a cocktail of different inhibitors targeting different polymorphs could be useful.

In summary, we used a combination of computational methods and rational design to develop a line of inhibitors targeted at preventing the spread of α-syn aggregates. Our approach was only made possible by the determination of the atomic structure of the core of α-syn amyloid fibrils, and this approach can be adopted for other diseases where seeding plays a role in disease progression.

Acknowledgements: The authors thank Dr. Marc Diamond for sharing the YFP labeled α-syn expressing HEK cells. SS is supported by a UCLA graduate division Dissertation Year fellowship.

Author Contributions: SS and DSE designed research and wrote the manuscript. SS performed all experiments. SS designed inhibitors. KM and LJ performed computational experiments. SS assisted with fiber extraction from PD tissues. MG contributed protocols.

Materials and methods:

α-synuclein purification: The α-synuclein construct was transformed into Escherichia coli expression cell line BL21 (DE3) gold (Agilent Technologies). For expression, 10 ml LB + Amp (100 μg/mL) was inoculated from transformed colonies and grown overnight. 30 ml of starting culture was added to a 2 L flask containing 1 L LB + Amp (100 μg/mL) and grown for 3 hours at 37 °C to OD600 = 0.6. IPTG was then added to 0.5 mM to induce protein expression, which continued for an additional 3 hours. The bacterial pellet was collected by centrifugation at 4000 rpm for 10 mins. Cell pellet was resuspended in 15 mL/L pellet lysis buffer (100 mM Tris- HCl pH 8.0, 1 mM EDTA pH 8.0) and lysed by sonication. Crude cell lysate was clarified by centrifugation at 15,000g for 30 min at 4 °C. 10 mg/ml Streptomycin was added to the supernantant and stirred on ice for 30 mins followed by centrifugation at 15000 rpm for 30 mins. Protein was then purified by ammonium sulfate precipitation by adding 0.22 g.ml ammonium sulfate and stirred on ice for 30 mins followed by centrifugation at 15000 rpm for 30 mins. The supernatant was discarded and the pellet re-suspended in 12 mL/L pellet of 20 mM Tris pH 8.0. The solution was then dialyzed against 4 L 20 mM tris pH 8.0 overnight to remove residual ammonium sulfate. Next day the protein was purified by HiPrep Q HP 16/10 column (GE Healthcare) using buffer A (20mM Tris pH 8.0) and buffer B (20mM Tris pH 8.0; 0.5M NaCl) using a gradient from 0-100% buffer B over 100 mL. Fractions containing protein were collected and pooled and injected on a preparative size exclusion silica G3000 column (Tosoh Bioscience). The column buffer comprised 0.1 M sodium sulfate, 25 mM

sodium phosphate, and 1 mM sodium azide, pH 6.5. Protein fractions were collected and concentration measured by Pierce BCA protein assay (Thermo #23225).

Inhibitor synthesis: Inhibitors were commercially obtained from Genscript Inc. at greater than 98% purity and solubilized in 100% DMSO at 10 mM concentration. Solublized inhibitors were filtered with 0.1 μM filter and stored at -20 °C in 20 μL aliquots until further use.

Thioflavin T assays: Fibril formation assays were performed with 50 μM protein concentration in conditions identical to those used for aggregating proteins for seeding assay, but with the addition of ThT. All assays were carried out in black Nunc 96-well optical bottom plates (Thermo Scientific). Plates were agitated at 600 rpm in 3-mm rotation diameter in a Varioskan microplate reader (Thermo) at 37 °C. Fluorescence measurements were recorded every 30 mins using λex = 444 nm, λem = 482 nm, with an integration time of 200 μs.

Aggregation assays: Purified α-synuclein was dialyzed in 0.1 M sodium sulfate, 25 mM sodium phosphate and aggregated by shaking in Torrey Pine shakers at 50 μM at 37 °C at speed 9 for 5-6 days.

Extraction of sarkosyl insoluble protein filaments from PD human brain tissues: Human frozen brain tissues were obtained from UCLA Brain Tumor Translational Resource (BTTR). Sarkosyl insoluble protein was extracted using previously described

protocols. Briefly, frozen tissue was homogenized in ice cold PBS using a dounce homogenizer at 200 mg/mL. The homogenate was then diluted in buffer A (10mM Tris 7.4, 800mM NaCl, 1mM EGTA, 10% Sucrose) to 50 mg/mL in total volume of 1 mL and centrifuged at 20,700 g for 20 min at 4°C. The supernatant was collected in an ultracentrifuge tube and pellet was resuspended in 0.5 mL buffer A followed by centrifugation at 20700 g for 20 mins at 4 °C. The supernatants pooled together. 150 µl 10% sarkosyl (w/v) in Millipore water was then added and incubated for 1 h at room temperature on flat rotating shaker at 700 rpm. The solution was then centrifuged at 100,000 g for 1 h at 4°C using SW 55 Rotor (Beckman Coulter). The supernatanat was discarded and pellet was washed with 5 mL Buffer A and centrifuged at 100,000 g for 20 mins at 4 °C. The pellet was resuspended in 100 µl 50 mM Tris pH7.4

HEK 293T cell culture: HEK293T cells that stably express YFP labeled WT α-syn and A53T α-syn were a generous gift from Dr. Marc Diamond. Cells were grown in Dulbecco's modified Eagle's medium (Gibco) supplemented with 10% fetal bovine serum (HyClone), 1% penicillin/streptomycin (Gibco), and 1% glutamax (Gibco) in a humidified incubator in 37°C, 5% CO2.

Seeding in HEK293T cells: 10,000 cells in 90 µL media were plated in 96 well black wall plate (Cat #3660) and allowed to adhere overnight. α-syn was transfected at a final monomer concentration of 125 nM. Lipofectamine 2000 was diluted in OptiMEM media (2.5 + 17.5 µL) and incubated at room temperautre for 5 mins. Protein aggregates were diluted in OptiMEM media (1:20) and sonicated in a water bath sonicator for 3 mins at

low pulse. Diluted lipofectamine and protein samples were then mixed 1:1 and incubated at room temperature for 20 mins and thereafter 10 μL was added to each well. All samples are added in triplicates and experiments were repeated a minimum of two times. For co-transfection of α-syn fibrils with inhibitors, the fibrils and inhibitors were diluted in OptiMEM and incubated for 3 hours followed by sonication.

Measurement of intracellular puncta in cells: Puncta formation and cell growth was measured using Celigo Imaging Cell Cytometer allowing for unbiased measurement. Wells were imaged using fluorescent GFP channel and confluence was measured using Celigo analysis software. Images of entire well were taken and particles counted by ImageJ by particle analysis. Same settings were used to analyze wells of one plate at all days. Total particles counted in each well were normalized against the confluence and reported as particles per well.

Figure Legend

Fig. 1: Design of α-syn seeding inhibitors. (A) Structure based design of α-syn aggregation inhibitors. Structure of NACore is composed of two self-complementary β-sheets forming steric zipper. Three types of inhibitors (maroon, orange and cyan) were identified that bind one or both ends. **(B)** Binding energies of the different inhibitors calculated by Rossetta show S37 and S62 bind both interfaces while S71 is only predicted to bind one interface. Shape complementarity of all three inhibitors is high. **(C)** Thioflavin T assay to measure α-syn aggregation and the effect of inhibitors. 50 μM α-syn and inhibitors at 5 fold molar excess were added.

Fig. 2: α-syn aggregates formed in the presence of inhibitors are not seeding competent. (A) Experimental design of cell culture seeding assay. α-syn was aggregated in the presence of inhibitors and the mixture was transfected in HEK293 cells expressing YFP labeled WT α-syn or A53T α-syn (green). Upon transfection endogenous α-syn formed fluorescent puncta (red) **(B)** NACore does not affect seeding capacity of α-syn fibrils. **(C,D,E)** 50 μM α-syn aggregated in 10, 5, 2 and 1 fold excess of S37, S61 and S62 was not seeding competent as measured by counting total number of particles formed per well in both WT and A53T expressing cells. **(F)** 50 μM α-syn aggregated in excess of S71 was not seeding competent as measured by counting total number of particles formed per well in both WT and A53T expressing cells. Results shown as Mean $\pm$ SD (n=3). Statistical significance was analyzed by two way ANOVA.

Fig. 3: Inhibitors prevent seeding in cell culture. (A) Experimental design of cell culture seeding assay. 125 nM recombinant α-syn fibrils were transfected with different amounts of inhibitors and aggregation monitored over time. **(B)** NACore does not affect seeding capacity **(C, D, E, F)** S37, S61, S62 and S71 reduce seeding capacity of α-syn. All data reported as particles counted per well and normalized to particles counted in buffer treated wells. Results shown as Mean ± SD (n=3). Statistical significance was analyzed by two way ANOVA.

Fig. 4: PD brain tissue extracted filaments seed α-syn aggregation in vitro and in cell culture. (A) Protocol for extraction of sarkosyl insoluble protein filaments from PD brain tissues. **(B,C,D)** 2% seeds from 3 different subjects induce rapid α-syn aggregation with 4-10 fold increase in ThT fluorescence. **(E,F,G)** α-syn seeded by filaments from PD subjects induce more particles than α-syn alone. All data reported as particles counted per well and normalized to particles counted in buffer treated wells. Results shown as Mean ± SD (n=3). Statistical significance was analyzed by two way ANOVA.

Fig. 5: Inhibitors prevent seeding by PD tissue extracted filaments. Filaments from 4 different subjects were tested for seeding α-syn aggregation and monitored by ThT assay. S61 and S62 were effective against all seeds that were tested. S71 was effective against seeds B and D.

Fig. 6: α-syn fibrils formed in the presence of PD filament seeds and inhibitors are not seeding competent. (A) Experimental design of cell culture seeding assay **(B, C, D)**

Inhibitors were tested for inhibition of seeding by three different PD brain extracted tissues. S71 was effective against all three seeds while S61 was effective against Seeds B. All data reported as particles counted in each well normalized to the particles counted in buffer treated wells. Results shown as Mean ± SD (n=3). Statistical significance was analyzed by two way ANOVA.

Fig. 7: Inhibitors reduce seeding by PD filament seeded α-syn fibrils in cell culture. **(A)** Experimental design of cell culture seeding assay. **(B,C,D)** α-syn fibrils formed in the presence of two different PD related filaments were transfected in YFP- α-syn HEK cells and fluorescence measured thereafter for up to 6 days. S37 prevented seeding at concentrations of 12.5 μM - 1.25 μM. S61 prevented seeding with a pronounced effect on Day 2. S71 reduced seeding at concentrations of 6.25 μM. All data reported as number of particles counted per well normalized to particles counted on Day 0 before transfection. Results shown as Mean ± SD (n=3). Statistical significance was analyzed by two-way ANOVA.

Figures

Fig. 1

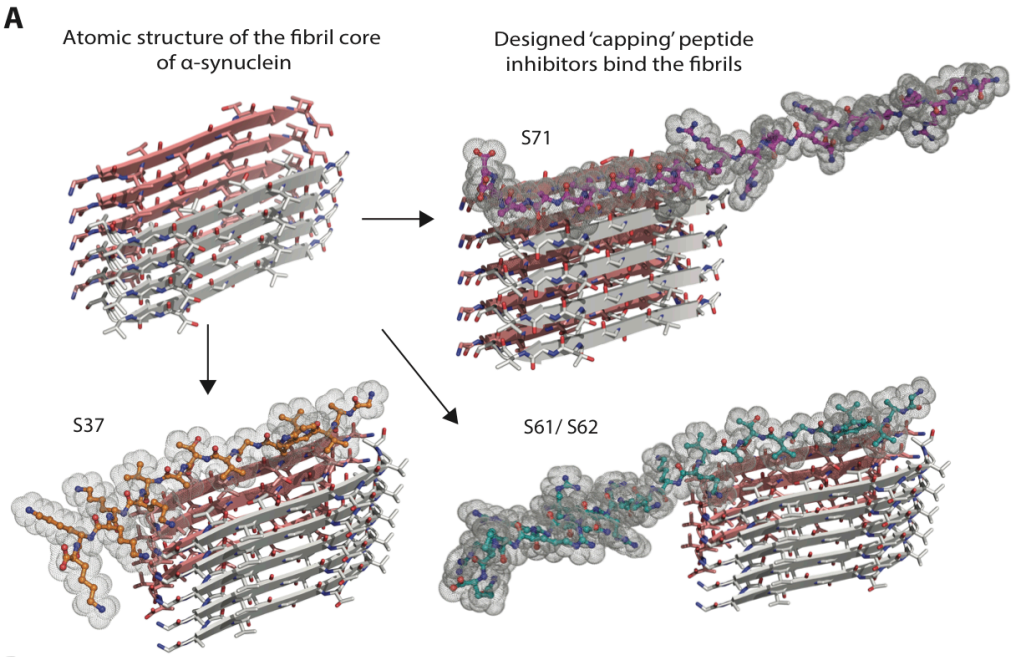

B

Inhibitor	Sequence	Top Binding Energy (REU)	Bottom Binding Energy (REU)	Sc
S37	G**AVVWGVTAV**KKKKK	-36.127	-39.357	0.721
S62	G**AVVWGVTAV**KKGRKKRRQRRRPQ	-36.127	-39.357	0.721
S71	YGRKKRRQRRR**AVVT{nme-Gly}VTAV**AE	does not bind	-38.441	0.747

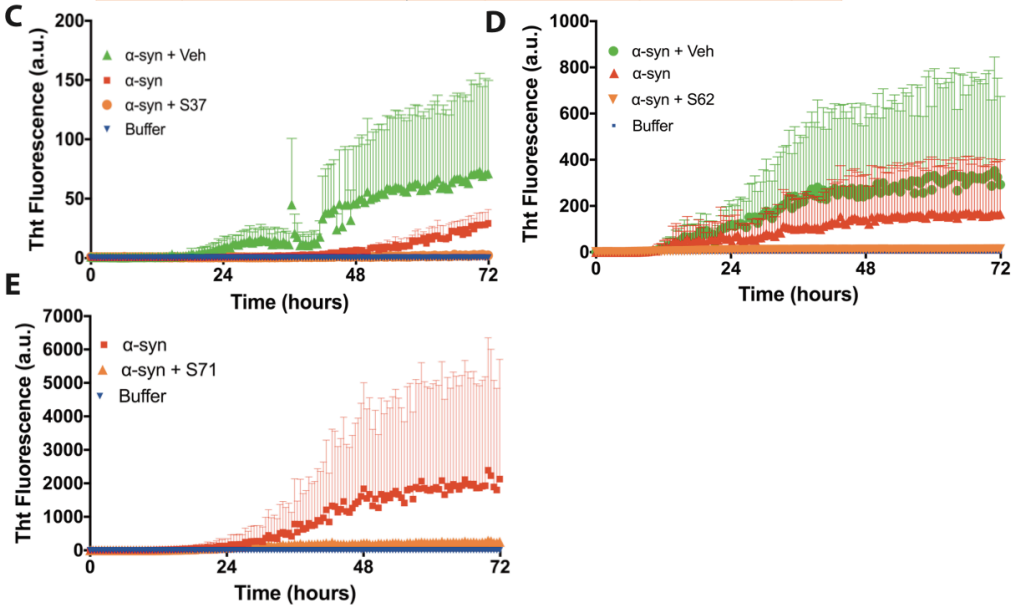

Fig. 2

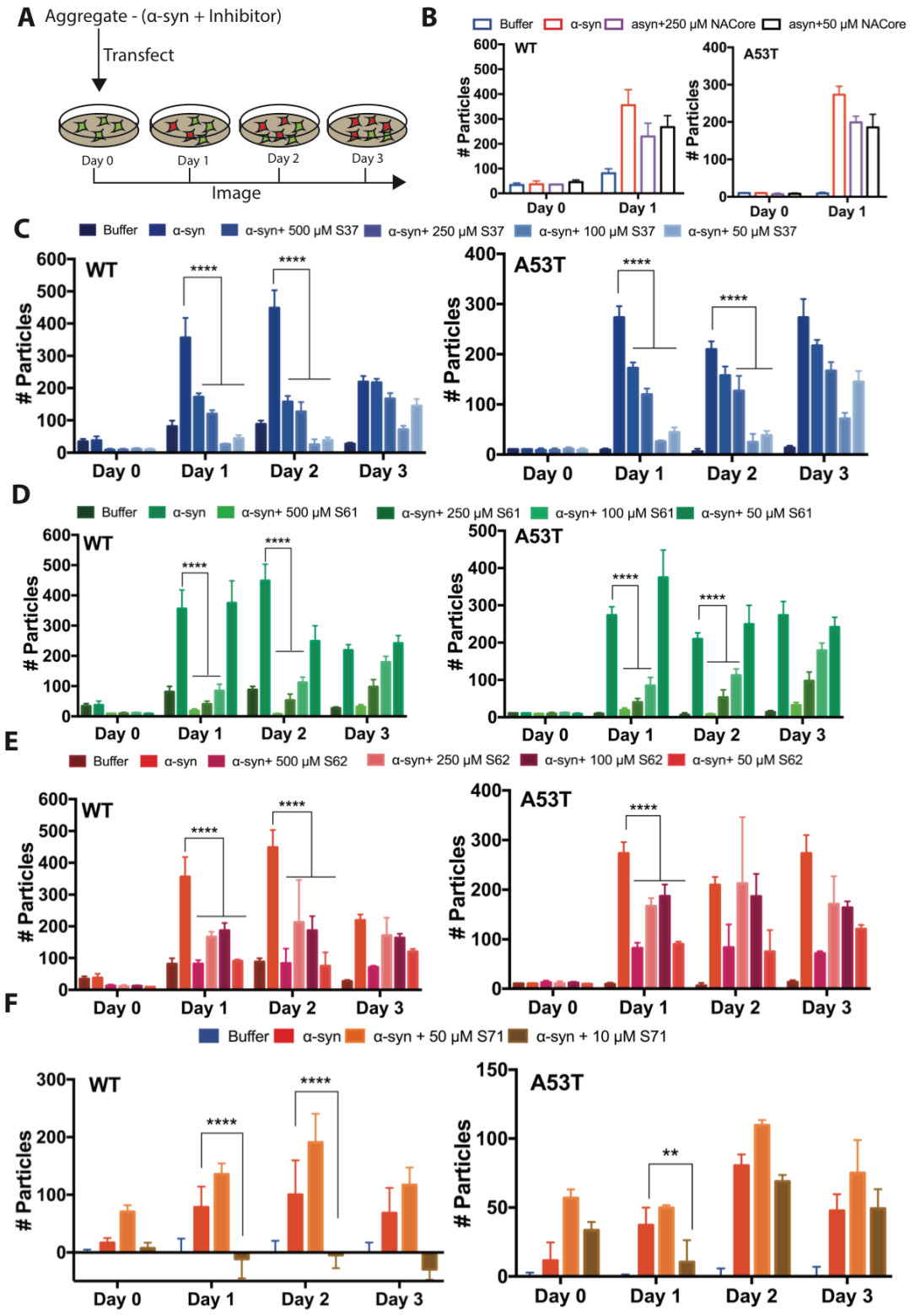
A
Aggregate - (α-syn + Inhibitor)
Transfect
Day 0
Day 1
Day 2
Day 3
Image
B
Buffer
α-syn
asyn+250 μM NACore
asyn+50 μM NACore
WT
A53T
Particles
C
Buffer
α-syn
α-syn+ 500 μM S37
α-syn+ 250 μM S37
α-syn+ 100 μM S37
α-syn+ 50 μM S37
D
Buffer
α-syn
α-syn+ 500 μM S61
α-syn+ 250 μM S61
α-syn+ 100 μM S61
α-syn+ 50 μM S61
E
Buffer
α-syn
α-syn+ 500 μM S62
α-syn+ 250 μM S62
α-syn+ 100 μM S62
α-syn+ 50 μM S62
F
Buffer
α-syn
α-syn + 50 μM S71
α-syn + 10 μM S71
Day 0
Day 1
Day 2
Day 3

Fig. 3

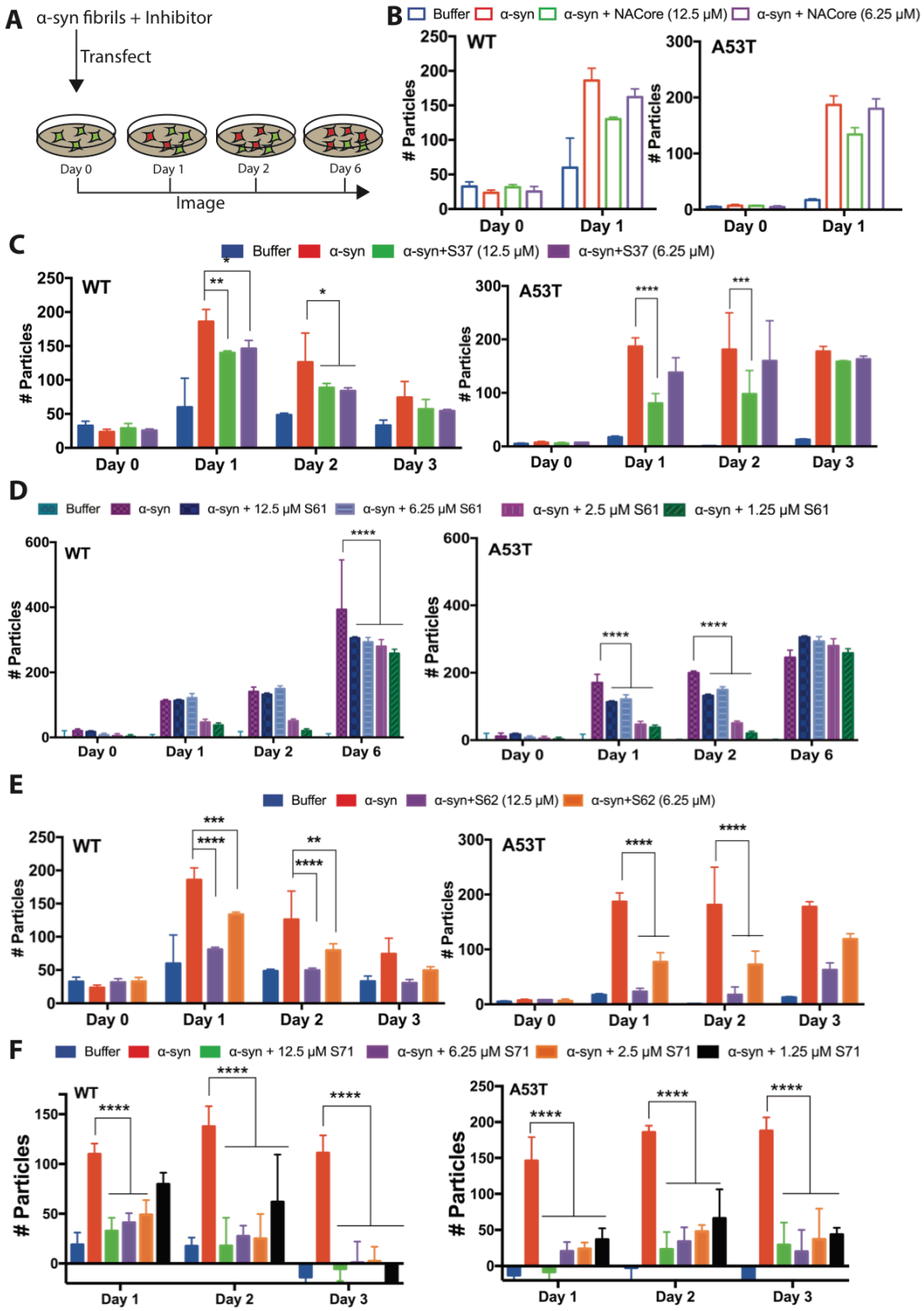
A
α-syn fibrils + Inhibitor
Transfect
Day 0
Day 1
Day 2
Day 6
Image
B
Buffer
α-syn
α-syn + NACore (12.5 μM)
α-syn + NACore (6.25 μM)
WT
A53T
Particles
Day 0
Day 1
C
Buffer
α-syn
α-syn+S37 (12.5 μM)
α-syn+S37 (6.25 μM)
WT
A53T
Particles
Day 0
Day 1
Day 2
Day 3
D
Buffer
α-syn
α-syn + 12.5 μM S61
α-syn + 6.25 μM S61
α-syn + 2.5 μM S61
α-syn + 1.25 μM S61
WT
A53T
Particles
Day 0
Day 1
Day 2
Day 6
E
Buffer
α-syn
α-syn+S62 (12.5 μM)
α-syn+S62 (6.25 μM)
WT
A53T
Particles
Day 0
Day 1
Day 2
Day 3
F
Buffer
α-syn
α-syn + 12.5 μM S71
α-syn + 6.25 μM S71
α-syn + 2.5 μM S71
α-syn + 1.25 μM S71
WT
A53T
Particles
Day 1
Day 2
Day 3

Fig. 4

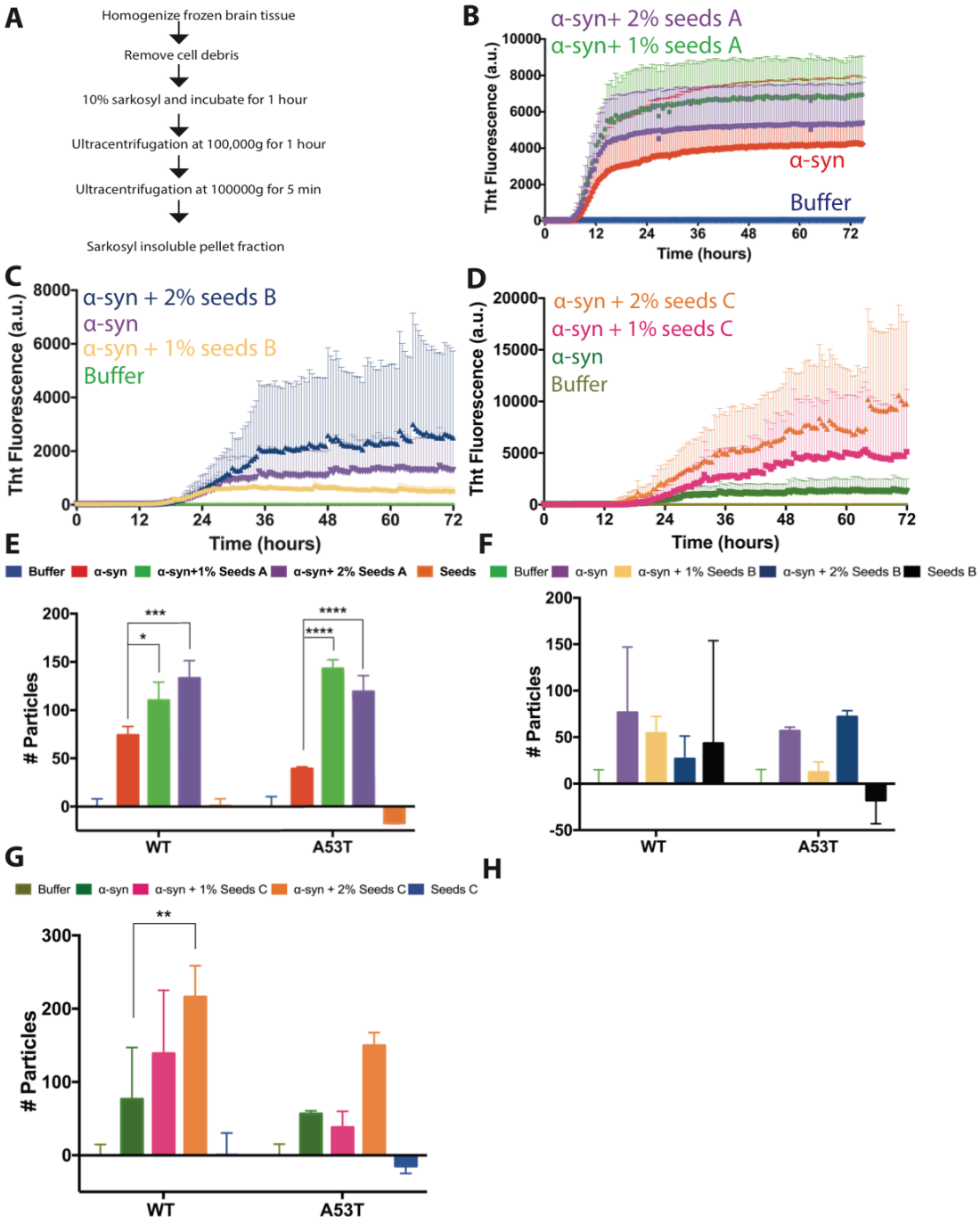
A
Homogenize frozen brain tissue
Remove cell debris
10% sarkosyl and incubate for 1 hour
Ultracentrifugation at 100,000g for 1 hour
Ultracentrifugation at 100000g for 5 min
Sarkosyl insoluble pellet fraction
B
α-syn+ 2% seeds A
α-syn+ 1% seeds A
α-syn
Buffer
Tht Fluorescence (a.u.)
Time (hours)
C
α-syn + 2% seeds B
α-syn
α-syn + 1% seeds B
Buffer
Tht Fluorescence (a.u.)
Time (hours)
D
α-syn + 2% seeds C
α-syn + 1% seeds C
α-syn
Buffer
Tht Fluorescence (a.u.)
Time (hours)
E
Buffer
α-syn
α-syn+1% Seeds A
α-syn+ 2% Seeds A
Seeds
Particles
WT
A53T
F
Buffer
α-syn
α-syn + 1% Seeds B
α-syn + 2% Seeds B
Seeds B
Particles
WT
A53T
G
Buffer
α-syn
α-syn + 1% Seeds C
α-syn + 2% Seeds C
Seeds C
Particles
WT
A53T
H

Fig. 5

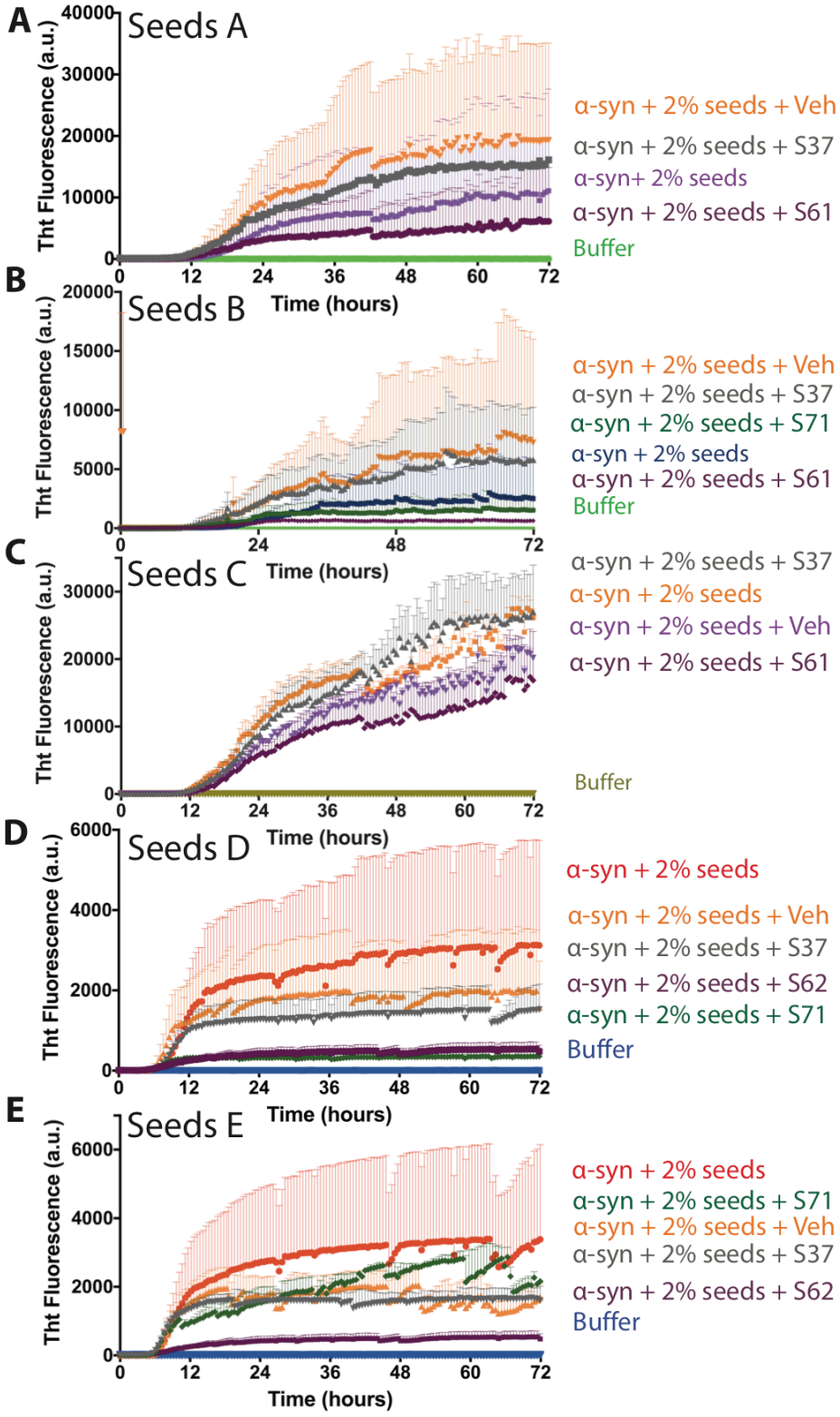
A
Seeds A
Tht Fluorescence (a.u.)
40000
30000
20000
10000
0
0
12
24
36
48
60
72
Time (hours)
α-syn + 2% seeds + Veh
α-syn + 2% seeds + S37
α-syn+ 2% seeds
α-syn + 2% seeds + S61
Buffer
B
Seeds B
Tht Fluorescence (a.u.)
20000
15000
10000
5000
0
0
24
48
72
Time (hours)
α-syn + 2% seeds + Veh
α-syn + 2% seeds + S37
α-syn + 2% seeds + S71
α-syn + 2% seeds
α-syn + 2% seeds + S61
Buffer
C
Seeds C
Tht Fluorescence (a.u.)
30000
20000
10000
0
0
12
24
36
48
60
72
Time (hours)
α-syn + 2% seeds + S37
α-syn + 2% seeds
α-syn + 2% seeds + Veh
α-syn + 2% seeds + S61
Buffer
D
Seeds D
Tht Fluorescence (a.u.)
6000
4000
2000
0
0
12
24
36
48
60
72
Time (hours)
α-syn + 2% seeds
α-syn + 2% seeds + Veh
α-syn + 2% seeds + S37
α-syn + 2% seeds + S62
α-syn + 2% seeds + S71
Buffer
E
Seeds E
Tht Fluorescence (a.u.)
6000
4000
2000
0
0
12
24
36
48
60
72
Time (hours)
α-syn + 2% seeds
α-syn + 2% seeds + S71
α-syn + 2% seeds + Veh
α-syn + 2% seeds + S37
α-syn + 2% seeds + S62
Buffer

Fig. 6

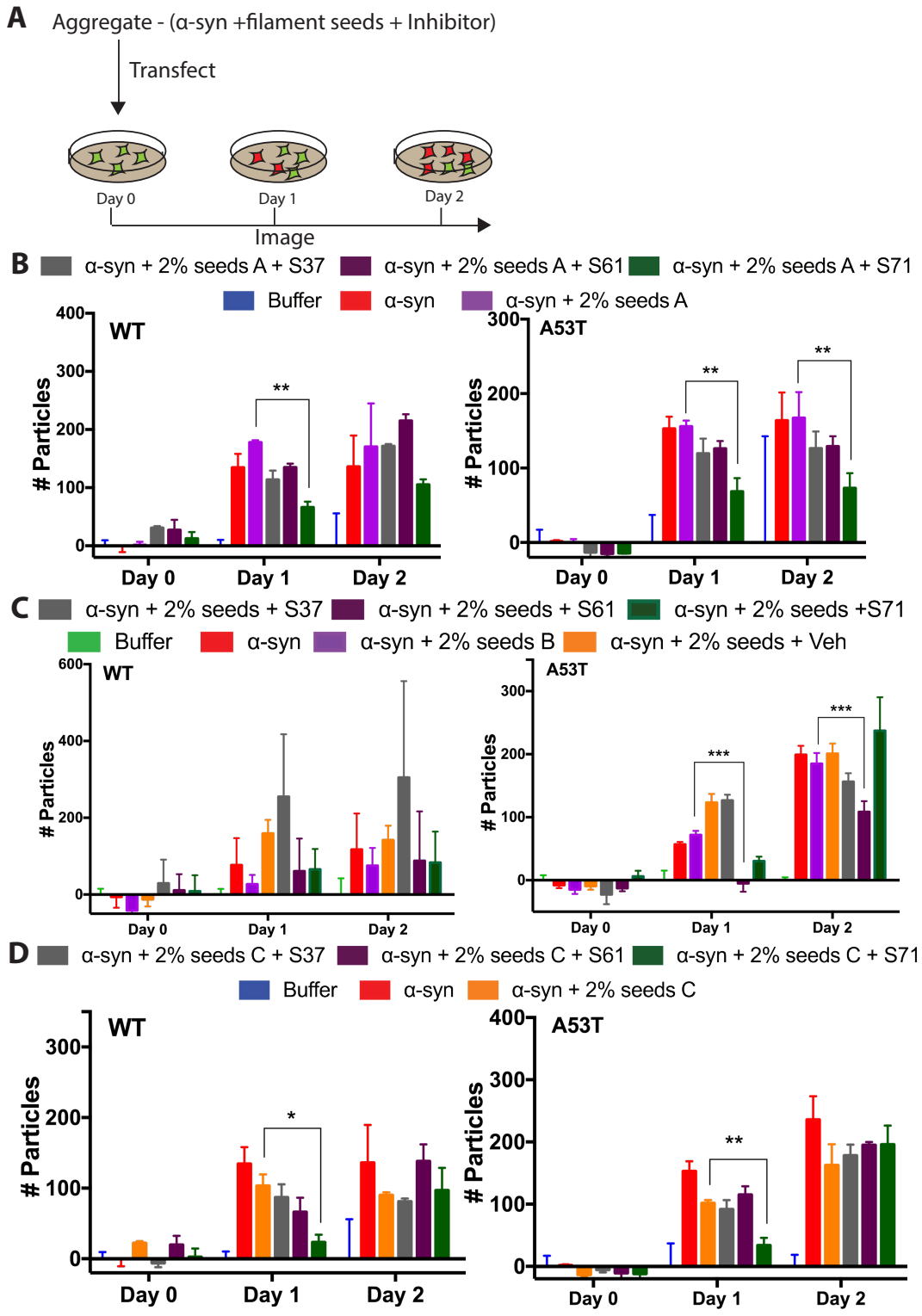
A
Aggregate - (α-syn +filament seeds + Inhibitor)
Transfect
Day 0
Day 1
Day 2
Image
B
α-syn + 2% seeds A + S37
α-syn + 2% seeds A + S61
α-syn + 2% seeds A + S71
Buffer
α-syn
α-syn + 2% seeds A
WT
A53T
Particles
Day 0
Day 1
Day 2
C
α-syn + 2% seeds + S37
α-syn + 2% seeds + S61
α-syn + 2% seeds +S71
Buffer
α-syn
α-syn + 2% seeds B
α-syn + 2% seeds + Veh
WT
A53T
Particles
Day 0
Day 1
Day 2
D
α-syn + 2% seeds C + S37
α-syn + 2% seeds C + S61
α-syn + 2% seeds C + S71
Buffer
α-syn
α-syn + 2% seeds C
WT
A53T
Particles
Day 0
Day 1
Day 2

Fig. 7

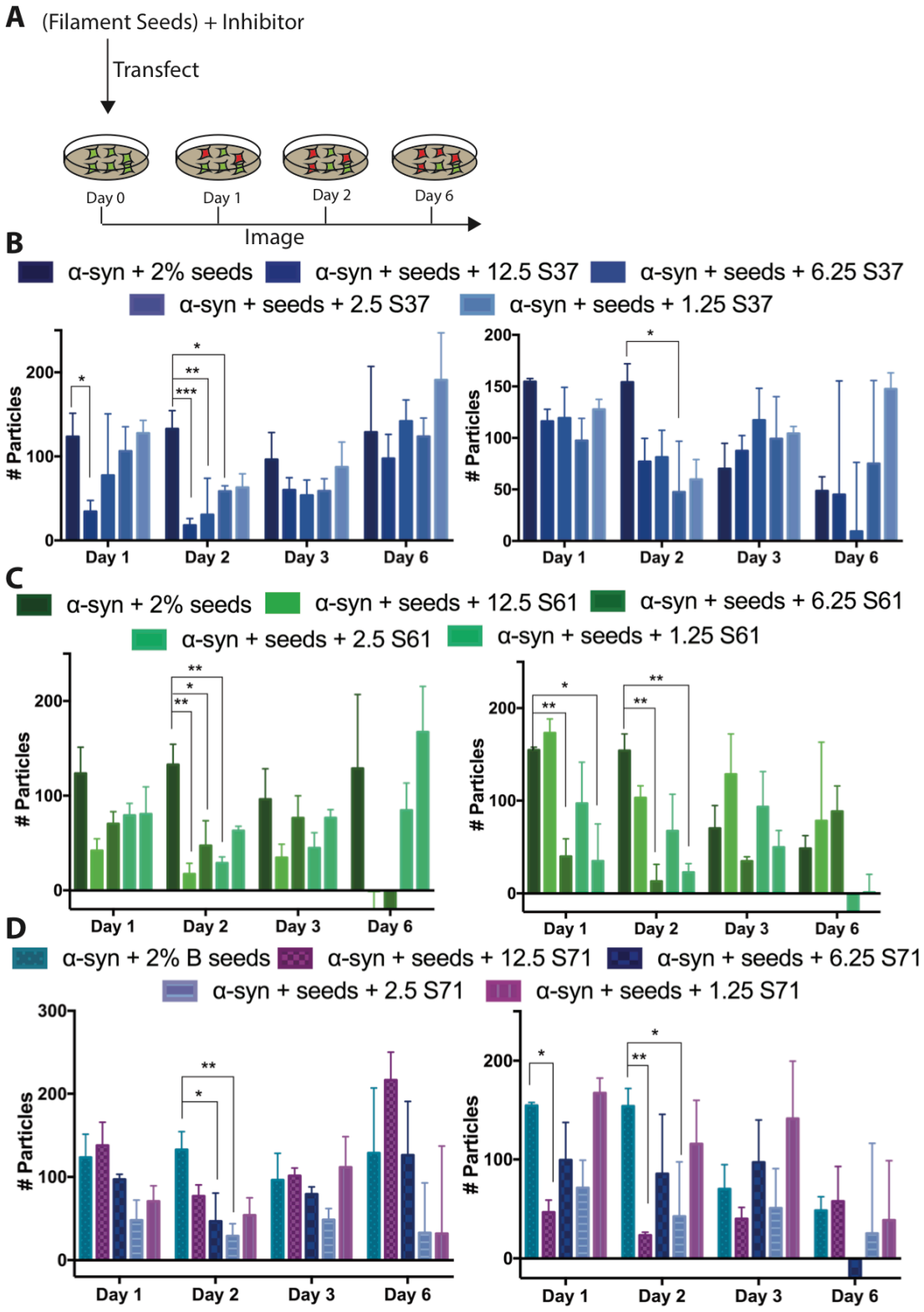
A
(Filament Seeds) + Inhibitor
Transfect
Day 0
Day 1
Day 2
Day 6
Image
B
α-syn + 2% seeds
α-syn + seeds + 12.5 S37
α-syn + seeds + 6.25 S37
α-syn + seeds + 2.5 S37
α-syn + seeds + 1.25 S37
Particles
Day 1
Day 2
Day 3
Day 6
C
α-syn + 2% seeds
α-syn + seeds + 12.5 S61
α-syn + seeds + 6.25 S61
α-syn + seeds + 2.5 S61
α-syn + seeds + 1.25 S61
Particles
Day 1
Day 2
Day 3
Day 6
D
α-syn + 2% B seeds
α-syn + seeds + 12.5 S71
α-syn + seeds + 6.25 S71
α-syn + seeds + 2.5 S71
α-syn + seeds + 1.25 S71
Particles
Day 1
Day 2
Day 3
Day 6

Table 1: Clinical Information of human tissues used in this study

Specimen ID	Brain Region	Age	Sex	Braak Stage	Clinical Diagnosis
(A)	Parietal	94	F	V	Parkinson's Disease with chances of AD
(B)	Left Frontal	89	F	NA	Parkinson's disease
(C)	Right Temporal	75	M	II	Parkinson's disease with chances of AD
(D)	SN	78	M	NA	Parkinson's Disease
(E)	Right Frontal	89	F	IV	Parkinson's disease with chances of AD

References:

1. Goedert M, Spillantini MG, Del Tredici K, Braak H (2012) 100 years of Lewy pathology. Nat Rev Neurol 9(1):13–24.

2. Miake H (2002) Biochemical Characterization of the Core Structure of alpha - Synuclein Filaments. J Biol Chem 277(21):19213–19219.

3. Rodriguez JA, et al. (2015) Structure of the toxic core of α-synuclein from invisible crystals. Nature 525(7570):486–490.

4. Tuttle MD, et al. (2016) Solid-state NMR structure of a pathogenic fibril of full-length human α-synuclein. Nat Struct Mol Biol 23(5):409–415.

5. Giasson BI, Murray IVJ, Trojanowski JQ, Lee VM-Y (2001) A Hydrophobic Stretch of 12 Amino Acid Residues in the Middle of α-Synuclein Is Essential for Filament Assembly. J Biol Chem 276(4):2380–2386.

6. Periquet M, Fulga T, Myllykangas L, Schlossmacher MG, Feany MB (2007) Aggregated α-Synuclein Mediates Dopaminergic Neurotoxicity In Vivo. J Neurosci 27(12):3338–3346.

7. Goedert M (2015) Alzheimer's and Parkinson's diseases: The prion concept in relation to assembled Aβ , tau, and α-synuclein. Science 349(6248):1255555–1255555.

8. Braak H, et al. (2003) Staging of brain pathology related to sporadic Parkinson's disease. Neurobiol Aging 24(2):197–211.

9. Braak H, Del Tredici K (2009) Neuroanatomy and pathology of sporadic Parkinson's disease. Adv Anat Embryol Cell Biol 201:1–119.

10. Masuda-Suzukake M, et al. (2013) Prion-like spreading of pathological α-synuclein in brain. Brain 136(4):1128–1138.

11. Desplats P, et al. (2009) Inclusion formation and neuronal cell death through neuron-to-neuron transmission of alpha-synuclein. Proc Natl Acad Sci U S A 106(31):13010–13015.

12. Luk KC, et al. (2009) Exogenous α-synuclein fibrils seed the formation of Lewy body-like intracellular inclusions in cultured cells. Proc Natl Acad Sci 106(47):20051–20056.

13. Mandler M, et al. (2015) Active immunization against alpha-synuclein ameliorates the degenerative pathology and prevents demyelination in a model of multiple system atrophy. Mol Neurodegener 10(1). doi:10.1186/s13024-015-0008-9.

14. Wrasidlo W, et al. (2016) A de novo compound targeting α-synuclein improves deficits in models of Parkinson's disease. Brain:aww238.

15. Sawaya MR, et al. (2007) Atomic structures of amyloid cross-β spines reveal varied steric zippers. Nature 447(7143):453–457.

16. Sanders DW, et al. (2014) Distinct Tau Prion Strains Propagate in Cells and Mice and Define Different Tauopathies. Neuron 82(6):1271–1288.

17. Goedert M, Spillantini MG, Cairns NJ, Crowther RA (1992) Tau proteins of alzheimer paired helical filaments: Abnormal phosphorylation of all six brain isoforms. Neuron 8(1):159–168.

18. Prusiner SB, et al. (2015) Evidence for α-synuclein prions causing multiple system atrophy in humans with parkinsonism. Proc Natl Acad Sci 112(38):E5308–E5317.

19. Woerman AL, et al. (2015) Propagation of prions causing synucleinopathies in cultured cells. Proc Natl Acad Sci 112(35):E4949–E4958.